Neural Control of Coordinated Wing and Leg Movements during a Terrestrial Threat Display

Thesis by

Shuo Cao

In Partial Fulfillment of the Requirements for

the degree of

Doctor of Philosophy

CALIFORNIA INSTITUTE OF TECHNOLOGY

Pasadena, California

2027

(Defended August 4, 2026)

Shuo Cao
ORCID: 0000-0002-4501-4065

ACKNOWLEDGEMENTS

I am deeply grateful to my PhD mentor, Dr. David Anderson, for his unwavering support throughout my graduate studies. He taught me how to approach scientific research with both creativity and rigor, setting an example of how science should be done.

I also thank my thesis defense committee, Dr. Elizabeth Hong, Dr. Michael Dickinson, and Dr. David Prober, as well as former members of my thesis advisory committee, Dr. Doris Tsao and Dr. Paul Sternberg, for their thoughtful guidance, insightful feedback, and encouragement.

I thank all the current and former members of the Anderson lab for a collaborative and supportive research environment, and for their insightful discussions, encouragements, and friendship.

Finally, I am profoundly grateful to my parents and friends for their constant love, encouragement, and unwavering support throughout the journey.

ABSTRACT

Social displays are a widespread form of animal communication used to signal intent and are central to survival and reproduction. These displays are often multi-modal, engage multiple body parts, and follow characteristic, species-specific patterns. Although their behavioral diversity is well described in the ethological and evolutionary literatures, the neural circuits that generate and coordinate them remain largely uncharacterized. The *Drosophila* male wing threat display offers a tractable system for addressing this gap: it is an intrinsic aggressive behavior built from coordinated wing and leg actions, including wing elevation, wing pump, turning, and charging, that can occur in both flexible and coordinated combinations. Prior work in the Anderson lab identified AIP, a small cluster of interneurons that is both necessary and sufficient for this display and dispensable for other aggressive behaviors such as lunging and tussling, suggesting that AIP functions as a command-like node specifically for wing threat. This thesis uses AIP as an entry point to determine how various wing and leg actions are controlled and coordinated by the neural circuits in wing threat display. By mapping AIP neurons onto an electron-microscopy connectome of the *Drosophila* brain, I identified its major downstream targets. For four of these, I generated sparse, specific genetic drivers and characterized their individual and combined contributions to behavior. Contrary to the expectation that each downstream neuron type would drive a single, dedicated action, this work shows that AIP targets are organized into two appendage-specific modules — one for the wings, one for the legs — each governed by its own combinatorial logic. Wing movements are controlled by two descending neurons, DNpe050 and DNp60, which act synergistically: activating either alone produces only weak effects but simultaneous co-activation of both drives robust wing actions. Leg movements, in contrast,

are governed by two interneurons with antagonistic effects on locomotion; their patterned co-activation produces the characteristic locomotion features of the wing threat, likely by recruiting and coordinating a broader population of downstream descending neurons. Together, these findings reveal a circuit-level logic by which different appendages are repurposed and coordinated to build specialized, structured actions during social display. This work provides a mechanistic framework for future studies of how animals select actions in real time during social interactions by integrating external sensory inputs and internal states.

PUBLISHED CONTENT AND CONTRIBUTIONS

Cao, S., and Anderson, D.J. (2025). “Neural control of coordinated wing and leg movements during a terrestrial threat display”. Preprint at bioRxiv, https://doi.org/10.1101/2025.10.25.684556

S.C. participated in the conception of the project, performed the experiments, analyzed and prepared the data, and co-wrote the manuscript.

TABLE OF CONTENTS

Chapter 1

INTRODUCTION

The biological significance of social display

Social display is widespread across the animal kingdom[1–9]. It serves as a critical channel for communicating an individual's intention and is essential for survival and reproduction. Females often select mates on the basis of their courtship displays, while threat displays signal aggressive intent and territorial claims without committing an animal to physical fights that could cause injury and death[10–12].

The forms of social display are remarkably diverse and typically recruit multiple body parts in tightly coordinated sequences. Male riflebirds (genus *Ptiloris*), for instance, alternate opposing motions of the head and wings while dragging the bill across the wing feathers to produce a mechanical "snap" sound, and expose a brightly colored gape at the climax of the display[13]. Elephants coordinate the ears, head, and trunk during threat displays — stepping forward with the head raised, the ears held in specific postures, and the trunk swinging or extending outward[14]. In many cases, opposite movements of a single body part convey emotions of opposite valence — a phenomenon Darwin termed the "principle of antithesis"[15]. Such complex combinations of body parts have been proposed to be evolutionarily meaningful: they may provide redundancy that reduces the risk of miscommunication, while also allowing additional information to be conveyed through different combinations of movements[16–18].

Although the diverse forms of social display have been well documented in ethological and evolutionary theory, the neural mechanisms underlying these displays remain poorly understood. Elucidating these mechanisms would provide a valuable paradigm for understanding how animals integrate sensory information, precisely coordinate the motor output of multiple body parts, and potentially reveal the evolutionary substrates of these behaviors.

Control of innate social behaviors

How does an animal decide whether to perform a social display, and how does it choose which form to express? Nikolaas Tinbergen proposed that innate behavior is selected through a hierarchical decision-making process[19]. At the top of this hierarchy sits a superordinate center — for example, a "reproductive center" — activated by external stimuli signaling favorable environmental conditions for reproduction. Downstream of this center are several intermediate centers, each governing a specific class of reproductive behavior, such as mating, aggression, or nest building. Excitation flows to a given intermediate center only once the appropriate sensory cues release its gate. Further downstream are the specific behaviors associated with each behavioral state, such as attack, threat display, biting, and so on. Mutual inhibition among centers at the same hierarchical level is thought to ensure that only one behavior is expressed at a time.

While this model has proven a useful ethological framework for behavioral selection, whether the underlying neural substrates are organized in the same hierarchical manner remains largely unknown. Work in the pond snail *Lymnaea* has identified an interneuron that mediates the suppression of feeding by the defensive withdrawal circuit[20]. This provides a

neural instantiation of the lateral-inhibition component of Tinbergen's model, but a full hierarchical circuit structure has yet to be identified in any species.

Neural circuits for social behaviors in Drosophila

Drosophila melanogaster has served as an excellent model for studying the neural mechanisms of social behaviors. Males perform an elaborate courtship ritual comprising a sequence of stereotyped actions — tapping the female, chasing, and unilateral wing extension and vibration of the wings to produce courtship songs[21] — as well as a rich repertoire of aggressive behaviors during antagonistic encounters, including wing threat, lunging, and tussling[22].

The *fruitless* (*fru*) gene has been a key entry point into the circuitry underlying fly courtship. *fru* mutant male flies direct courtship toward same-sex targets[23,24]. *fru* is expressed in around 2,000 neurons dispersed throughout the male nervous system[25–27], which have been subdivided into ~100 genetically and morphologically distinct classes[28,29]. These neurons collectively mediate courtship behavior[26,27,30–32].

Among the *fru*-positive courtship-promoting neurons, the best-known are P1 neurons. The P1 cluster is a male-specific population of neurons whose activation promotes courtship[31,33–35]. P1 neurons are activated by a variety of sensory stimuli, including visual and chemosensory cues[31,36,37]. Leg gustatory neurons expressing *ppk23* and *ppk29* mediate the detection of female pheromones that promote male courtship[38–43]. This chemosensory information is relayed via vAB3 ascending neurons, which provide excitatory input to P1 neurons as well as feedforward inhibitory input through another neuron type, mAL[37]. P1

neurons also promote a persistent state that facilitates social interaction, including aggression[37,44,45] (discussed later in this section).

Various descending neurons and downstream VNC neurons have also been identified as contributing to courtship. A screen for *fru*-expressing neurons whose activation promotes courtship has identified pIP10, a descending neuron type downstream of P1, as well as three VNC neuron types, dPR1, vPR6, and vMS11, that promote courtship songs[34]. TN1 neurons in the VNC also promote song production[46]. More recent studies have identified an additional DN type, pMP2, along with several further VNC neuron types involved in song production, and have suggested a nested network organization of these neurons that mediates song-type selection[47,48]. A descending neuron type, aSP22, promotes a sequence of courtship behaviors, including licking the female, abdomen bending, and foreleg tapping[49].

Although these neurons have been identified and many studies have focused on the generation and modulation of the courtship song by the wings[47,48,50–54], considerably less is known about how the song and non-song actions are coordinated by the central brain circuits.

What neurons control aggression? Neuromodulators are well known to modulate aggressiveness in arthropods[55–59], and octopamine and serotonin (5-HT) have been shown to promote fighting in *Drosophila*[57,60,61]. However, the cellular basis of these effects remained unclear. To address this, a screen of genetic driver lines generated from the putative promoter regions of ~20 different *Drosophila* neuropeptide genes identified Tachykinin-expressing neurons that promote aggressiveness[62]. Subsequently, octopamine-receptor-expressing aSP2 neurons were found to integrate input from octopaminergic neurons and social behavior-promoting neurons to control aggression[63].

An unbiased screen of ~3000 Gal4 drivers for aggression-promoting neurons identified drivers that labelled a common cluster of 8-10 neurons per hemisphere, morphologically similar to P1 neurons[64]. These neurons are termed $P1^a$. Surprisingly, optogenetic activation of $P1^a$ induces a persistent internal state of aggression lasting as long as 10 min after the LED is turned off, in addition to inducing unilateral wing extension that is time-locked to photo-stimulation. This work reveals a new role of P1 neurons, which had previously been considered solely as a courtship-promoting center. The same screening also identified a distinct aggression-promoting genetic driver, R60G08-Gal4, that does not label $P1^a$. A follow-up study showed that this driver labels two neuron types, CAP and MAP, which control approach and attack, respectively, corresponding to the appetitive and consummatory phases of aggression[65].

As noted above, aggressive behaviors in the fruit fly comprise a rich repertoire of distinct actions. How are these different behaviors controlled? Another study identified a group of interneurons that specifically control wing threat, termed AIP neurons[66]. AIP neurons are both necessary and sufficient for wing threat but dispensable for other aggressive behaviors such as lunging and tussling, indicating that they function as a module specific to wing threat. Artificial activation of AIP neurons can induce the full set of leg and wing actions associated with this display, including turning, charging, wing elevation and wing pump, in a threshold-dependent manner, suggesting a unique role for AIP in coordinating the motor execution of wing threat. This work identified a neural node corresponding to the third level of Tinbergen's model. However, it remains unclear how the wing threat module relates to other aggression circuits, and how wing and leg movements are coordinated to generate the various combinations of actions observed during natural wing threat.

Descending control of wings and legs in Drosophila

Descending neurons (DNs) connect the brain to the ventral nerve cord (VNC). *Drosophila melanogaster* has approximately 1,300 DNs[67–69], a small population relative to the ~130,000 neurons in the central brain[70–73] and the 20,000 neurons in the VNC[72–75]. DNs therefore act as an information bottleneck, conveying highly compressed motor commands from the brain to the VNC. Their small number also makes them a tractable entry point for studying how motor actions are organized into behaviors of various complexity. Recent advances in genetic tools[76–80] and connectomics[70,72–75,81,82] have accelerated our understanding of DN function, particularly for the canonical uses of the wings and legs: walking and flight.

Multiple DNs have been studied in detail for walking. Moonwalker DNs initiate backward walking and suppress forward walking[83]. An unbiased screen for locomotor phenotypes identified DNs that promote forward walking[84]. DNp09 drives ipsilateral turning and is necessary for courtship chasing[84,85]. BPN, a central-brain interneuron, promotes straight walking[84], likely through downstream DNs such as DNg97 and DNg100[86,87]. Other DNs specifically control turning: DNa01 and DNa02 mediate low- and high-gain steering, respectively[88], and DNa02 and DNg13 shape turning by differentially adjusting inner versus outer stride length[89]. More work has revealed a hierarchical central circuit, involving the interneuron LAL013 together with the descending neurons, DNa03 and DNa11 that coordinate turning[90].

Flight has been dissected in comparable detail[91,92]. AX, later identified as DNae014, drives flight saccades together with DNb01[93,94]. DNOVS1, DNOVS2, and

DNHS1 integrate input from LPTC neurons and encode self-motion around the three body axes[95]. DNp06 mediates evasive turns[96], and DNp03 also contributes to saccade generation[97,98]. Distinct from these command-like neurons, DNg12, a population of 15 DN pairs, regulates wing beat amplitude via a population code[99].

Beyond walking and flight, individual DNs have been linked to other actions of the wings and legs. Giant Fiber neurons trigger a non-directional escape behavior[100,101], and DNp02, DNp04, and DNp11 contribute to escape as well[102]. DNp07 and DNp10 drive landing[103]. aDN, DNg11, and DNg12 each control grooming of distinct body parts[104].

The accumulating characterization of individual DNs has begun to reveal general principles of how DNs encode behavior. Most DNs characterized to date appear to function in a command-like manner, whereby activation of a single DN induces a specific behavior in an all-or-none fashion. However, the example of DNg12 shows that DNs can also use population coding to control graded, scalable features of a behavior, such as wing-beat amplitude. Work on fruit fly courtship song suggests that the combined activity of pIP10 and pMP2 may underlie selection between sine song and pulse song[47,48]. Together, these findings suggest that population coding represents an alternative strategy by which DNs control action. A recent study has attempted to reconcile these two modes of DN function[105]. This work reported that DNs, in addition to their descending output to the VNC premotor neurons, are also densely interconnected with one another, providing a circuit substrate for population coding. Notably, the DNs previously characterized as command-like were found to occupy a privileged position within this network, acting as recruiters that broadcast output to other DNs. Based on this, the author proposes that the apparent command-like property of these neurons may actually emerge from their capacity to recruit a broader population of DNs.

Despite these advances, it remains unclear whether this recruitment-based model generalizes across DN populations, or whether other modes of action coding remain to be discovered. It is likewise unclear how DNs, or DN networks more broadly, are organized by the central brain when a behavior requires the coordinated, repurposed use of multiple appendages for specialized actions — a demand that is especially pronounced in social displays.

Connectome: a transformative advance in *Drosophila* circuit studies

Recent advances in connectomics have profoundly reshaped how neural circuits are delineated in *Drosophila*. Complete or near-complete connectomes have become available in rapid succession, spanning the central brain[70,106–108], the ventral nerve cord[74,75,81,109–111], and most recently the entire central nervous system[72,73]. Despite methodological variation, these datasets share a common pipeline: electron microscopy (EM) of the complete or partial nervous system, followed by computationally assisted segmentation of individual neurons and detection of their synapses. The resolution of EM imaging allows single neurons to be traced and individual synapses to be identified[112], ultimately yielding an all-by-all connectivity matrix that documents the number of synapses between every pair of neurons in the fly nervous system.

Connectomes serve as powerful hypothesis generators: the connectivity pattern of a given neuron can be used to infer its likely function, though establishing causal relationships still requires perturbing neuronal activity in the intact animal. *Drosophila* is unusually well suited to this next step. Tens of thousands of Gal4 and Split-Gal4 driver lines allow specific neurons to be targeted[76–80,113], and a suite of computational tools[114–118] has been developed

to enable the neurons identified in EM datasets to be matched to their counterparts in light-microscopy driver libraries. Calcium indicators[119] and in vivo imaging techniques are available for researchers to experimentally measure the functional connectivity suggested by the connectomes. Combined with a mature toolkit for neuronal perturbation — Chrimson for optogenetic activation[45,120], and Kir2.1, GtACR, or RubyACR[121–123] for silencing — these resources give *Drosophila* an unmatched platform for dissecting neural circuits. With the connectome now in hand, there is a unique opportunity to ask how appendage movements are coordinated during social display.

References

1. Scholes, E., and Laman, T.G. (2018). Distinctive courtship phenotype of the Vogelkop Superb Bird-of-Paradise Lophorina niedda Mayr, 1930 confirms new species status. PeerJ *6*, e4621. https://doi.org/10.7717/peerj.4621.

2. Parnell, R.J., and Buchanan-Smith, H.M. (2001). An unusual social display by gorillas. Nature *412*, 294–294. https://doi.org/10.1038/35085631.

3. Nelson, X.J., and Jackson, R.R. (2010). Complex display behaviour during the intraspecific interactions of myrmecomorphic jumping spiders (Araneae, Salticidae). Journal of Natural History *41*, 1659–1678. https://doi.org/10.1080/00222930701450504.

4. LOXTON, R.G. (1979). On display behaviour and courtship in the praying mantis Ephestiasula amoena (Bolivar). Zool J Linn Soc *65*, 103–110. https://doi.org/10.1111/j.1096-3642.1979.tb01083.x.

5. Van Parijs, S.M., Hastie, G.D., and Thompson, P.M. (2000). Individual and geographical variation in display behaviour of male harbour seals in Scotland. Animal Behaviour *59*, 559–568. https://doi.org/10.1006/anbe.1999.1307.

6. Brown, B.V., and Porras, W. (2015). Extravagant female sexual display in a Megaselia Rondani species (Diptera: Phoridae). Biodiversity Data Journal *3*, e4368. https://doi.org/10.3897/BDJ.3.e4368.

7. Cárdenas-Posada, G., Cadena, C.D., Blake, J.G., and Loiselle, B.A. (2018). Display behaviour, social organization and vocal repertoire of Blue-backed Manakin Chiroxiphia pareola napensis in northwest Amazonia. Ibis *160*, 269–282. https://doi.org/10.1111/ibi.12548.

8. Mikula, P., Toszogyova, A., and Albrecht, T. (2022). A global analysis of aerial displays in passerines revealed an effect of habitat, mating system and migratory traits. Proceedings of the Royal Society B: Biological Sciences *289*, 20220370. https://doi.org/10.1098/rspb.2022.0370.

9. Rubenstein, D.I., and Hazlett, B.A. (1974). Examination of the Agonistic Behaviour of the Crayfish Orconectes Virilis By Character Analysis. Behaviour *50*, 193–215. https://doi.org/10.1163/156853974X00453.

10. Smith, J.M., and Price, G.R. (1973). The Logic of Animal Conflict. Nature *246*, 15–18. https://doi.org/10.1038/246015a0.

11. Hurd, P., and Enquist, M. (2001). Threat displays in birds. Canadian Journal of Zoology *79*, 931–942.

12. Enquist, M. (1985). Communication during aggressive interactions with particular reference to variation in choice of behaviour. Animal Behaviour *33*, 1152–1161. https://doi.org/10.1016/S0003-3472(85)80175-5.

13. MacGillavry, T., Frith, C.B., and Fusani, L. (2024). The mechanics of male courtship display behaviour in the Ptiloris riflebirds (Aves: Paradisaeidae). Biol J Linn Soc *143*, blae077. https://doi.org/10.1093/biolinnean/blae077.

14.Poole, J.H., and Granli, P. (2011). Signals, Gestures, and Behavior of African Elephants. In The Amboseli Elephants: A Long-Term Perspective on a Long-Lived Mammal, C. J. Moss, H. Croze, and P. C. Lee, eds. (University of Chicago Press), p. 0. https://doi.org/10.7208/chicago/9780226542263.003.0008.

15. Darwin, C. (1872). The expression of the emotions in man and animals (John Murray) https://doi.org/10.1037/10001-000.

16. Partan, S.R., Marler, P., null, null, and null, null (2005). Issues in the Classification of Multimodal Communication Signals. The American Naturalist *166*, 231–245. https://doi.org/10.1086/431246.

17. Fleishman, L.J. (1992). The Influence of the Sensory System and the Environment on Motion Patterns in the Visual Displays of Anoline Lizards and Other Vertebrates. The American Naturalist *139*, S36–S61. https://doi.org/10.1086/285304.

18. Mitoyen, C., Quigley, C., and Fusani, L. (2019). Evolution and function of multimodal courtship displays. Ethology *125*, 503–515. https://doi.org/10.1111/eth.12882.

19. Tinbergen, N. (1951). The study of instinct (Clarendon Press/Oxford University Press).

20. Pirger, Z., Crossley, M., László, Z., Naskar, S., Kemenes, G., O'Shea, M., Benjamin, P.R., and Kemenes, I. (2014). Interneuronal Mechanism for Tinbergen's Hierarchical Model of Behavioral Choice. Current Biology *24*, 2018–2024. https://doi.org/10.1016/j.cub.2014.07.044.

21. Yamamoto, D., Sato, K., and Koganezawa, M. (2014). Neuroethology of male courtship in Drosophila: from the gene to behavior. J Comp Physiol A *200*, 251–264. https://doi.org/10.1007/s00359-014-0891-5.

22. Chen, S., Lee, A.Y., Bowens, N.M., Huber, R., and Kravitz, E.A. (2002). Fighting fruit flies: A model system for the study of aggression. PNAS *99*, 5664–5668. https://doi.org/10.1073/pnas.082102599.

23. Ito, H., Fujitani, K., Usui, K., Shimizu-Nishikawa, K., Tanaka, S., and Yamamoto, D. (1996). Sexual orientation in Drosophila is altered by the satori mutation in the sex-

determination gene fruitless that encodes a zinc finger protein with a BTB domain. Proc. Natl. Acad. Sci. U.S.A. *93*, 9687–9692. https://doi.org/10.1073/pnas.93.18.9687.

24. Ryner, L.C., Goodwin, S.F., Castrillon, D.H., Anand, A., Villella, A., Baker, B.S., Hall, J.C., Taylor, B.J., and Wasserman, S.A. (1996). Control of Male Sexual Behavior and Sexual Orientation in Drosophila by the fruitless Gene. Cell *87*, 1079–1089. https://doi.org/10.1016/S0092-8674(00)81802-4.

25. Lee, G., Foss, M., Goodwin, S.F., Carlo, T., Taylor, B.J., and Hall, J.C. (2000). Spatial, temporal, and sexually dimorphic expression patterns of the fruitless gene in the Drosophila central nervous system. Journal of Neurobiology *43*, 404–426. https://doi.org/10.1002/1097-4695(20000615)43:4%3C404::AID-NEU8%3E3.0.CO;2-D.

26. Manoli, D.S., Foss, M., Villella, A., Taylor, B.J., Hall, J.C., and Baker, B.S. (2005). Male-specific fruitless specifies the neural substrates of Drosophila courtship behaviour. Nature *436*, 395–400. https://doi.org/10.1038/nature03859.

27. Stockinger, P., Kvitsiani, D., Rotkopf, S., Tirián, L., and Dickson, B.J. (2005). Neural Circuitry that Governs Drosophila Male Courtship Behavior. Cell *121*, 795–807. https://doi.org/10.1016/j.cell.2005.04.026.

28. Yu, J.Y., Kanai, M.I., Demir, E., Jefferis, G.S.X.E., and Dickson, B.J. (2010). Cellular Organization of the Neural Circuit that Drives Drosophila Courtship Behavior. Current Biology *20*, 1602–1614. https://doi.org/10.1016/j.cub.2010.08.025.

29. Cachero, S., Ostrovsky, A.D., Yu, J.Y., Dickson, B.J., and Jefferis, G.S.X.E. (2010). Sexual Dimorphism in the Fly Brain. Current Biology *20*, 1589–1601. https://doi.org/10.1016/j.cub.2010.07.045.

30. Clyne, J.D., and Miesenböck, G. (2008). Sex-Specific Control and Tuning of the Pattern Generator for Courtship Song in Drosophila. Cell *133*, 354–363. https://doi.org/10.1016/j.cell.2008.01.050.

31. Kohatsu, S., Koganezawa, M., and Yamamoto, D. (2011). Female Contact Activates Male-Specific Interneurons that Trigger Stereotypic Courtship Behavior in Drosophila. Neuron *69*, 498–508. https://doi.org/10.1016/j.neuron.2010.12.017.

32. Pan, Y., Robinett, C.C., and Baker, B.S. (2011). Turning Males On: Activation of Male Courtship Behavior in Drosophila melanogaster. PLOS ONE *6*, e21144. https://doi.org/10.1371/journal.pone.0021144.

33. Kimura, K., Hachiya, T., Koganezawa, M., Tazawa, T., and Yamamoto, D. (2008). Fruitless and Doublesex Coordinate to Generate Male-Specific Neurons that Can Initiate Courtship. Neuron *59*, 759–769. https://doi.org/10.1016/j.neuron.2008.06.007.

34. von Philipsborn, A.C., Liu, T., Yu, J.Y., Masser, C., Bidaye, S.S., and Dickson, B.J. (2011). Neuronal Control of Drosophila Courtship Song. Neuron *69*, 509–522. https://doi.org/10.1016/j.neuron.2011.01.011.

35. Pan, Y., Meissner, G.W., and Baker, B.S. (2012). Joint control of Drosophila male courtship behavior by motion cues and activation of male-specific P1 neurons. Proceedings of the National Academy of Sciences *109*, 10065–10070. https://doi.org/10.1073/pnas.1207107109.

36. Yamamoto, D., and Koganezawa, M. (2013). Genes and circuits of courtship behaviour in Drosophila males. Nat Rev Neurosci *14*, 681–692. https://doi.org/10.1038/nrn3567.

37. Clowney, E.J., Iguchi, S., Bussell, J.J., Scheer, E., and Ruta, V. (2015). Multimodal Chemosensory Circuits Controlling Male Courtship in Drosophila. Neuron *87*, 1036–1049. https://doi.org/10.1016/j.neuron.2015.07.025.

38. Lin, H., Mann, K.J., Starostina, E., Kinser, R.D., and Pikielny, C.W. (2005). A Drosophila DEG/ENaC channel subunit is required for male response to female pheromones. Proceedings of the National Academy of Sciences *102*, 12831–12836. https://doi.org/10.1073/pnas.0506420102.

39. Thistle, R., Cameron, P., Ghorayshi, A., Dennison, L., and Scott, K. (2012). Contact Chemoreceptors Mediate Male-Male Repulsion and Male-Female Attraction during Drosophila Courtship. Cell *149*, 1140–1151. https://doi.org/10.1016/j.cell.2012.03.045.

40. Lu, B., LaMora, A., Sun, Y., Welsh, M.J., and Ben-Shahar, Y. (2012). ppk23-Dependent Chemosensory Functions Contribute to Courtship Behavior in Drosophila melanogaster. PLOS Genetics *8*, e1002587. https://doi.org/10.1371/journal.pgen.1002587.

41. Starostina, E., Liu, T., Vijayan, V., Zheng, Z., Siwicki, K.K., and Pikielny, C.W. (2012). A *Drosophila* DEG/ENaC Subunit Functions Specifically in Gustatory Neurons Required for Male Courtship Behavior. J. Neurosci. *32*, 4665–4674. https://doi.org/10.1523/JNEUROSCI.6178-11.2012.

42. Liu, T., Starostina, E., Vijayan, V., and Pikielny, C.W. (2012). Two *Drosophila* DEG/ENaC Channel Subunits Have Distinct Functions in Gustatory Neurons That Activate Male Courtship. J. Neurosci. *32*, 11879–11889. https://doi.org/10.1523/JNEUROSCI.1376-12.2012.

43. Toda, H., Zhao, X., and Dickson, B.J. (2012). The Drosophila Female Aphrodisiac Pheromone Activates ppk23+ Sensory Neurons to Elicit Male Courtship Behavior. Cell Reports *1*, 599–607. https://doi.org/10.1016/j.celrep.2012.05.007.

44. Hoopfer, E.D. (2016). Neural control of aggression in Drosophila. Current Opinion in Neurobiology *38*, 109–118. https://doi.org/10.1016/j.conb.2016.04.007.

45. Inagaki, H.K., Jung, Y., Hoopfer, E.D., Wong, A.M., Mishra, N., Lin, J.Y., Tsien, R.Y., and Anderson, D.J. (2014). Optogenetic control of Drosophila using a red-shifted channelrhodopsin reveals experience-dependent influences on courtship. Nature Methods *11*, 325–332. https://doi.org/10.1038/nmeth.2765.

46. Shirangi, T.R., Wong, A.M., Truman, J.W., and Stern, D.L. (2016). Doublesex Regulates the Connectivity of a Neural Circuit Controlling Drosophila Male Courtship Song. Developmental Cell *37*, 533–544. https://doi.org/10.1016/j.devcel.2016.05.012.

47. Lillvis, J.L., Wang, K., Shiozaki, H.M., Xu, M., Stern, D.L., and Dickson, B.J. (2024). Nested neural circuits generate distinct acoustic signals during Drosophila courtship. Current Biology *34*, 808-824.e6. https://doi.org/10.1016/j.cub.2024.01.015.

48. Shiozaki, H.M., Wang, K., Lillvis, J.L., Xu, M., Dickson, B.J., and Stern, D.L. (2024). Activity of nested neural circuits drives different courtship songs in Drosophila. Nat Neurosci *27*, 1954–1965. https://doi.org/10.1038/s41593-024-01738-9.

49. McKellar, C.E., Lillvis, J.L., Bath, D.E., Fitzgerald, J.E., Cannon, J.G., Simpson, J.H., and Dickson, B.J. (2019). Threshold-Based Ordering of Sequential Actions during Drosophila Courtship. Current Biology *29*, 426-434.e6. https://doi.org/10.1016/j.cub.2018.12.019.

50. Coen, P., Clemens, J., Weinstein, A.J., Pacheco, D.A., Deng, Y., and Murthy, M. (2014). Dynamic sensory cues shape song structure in Drosophila. Nature *507*, 233–237. https://doi.org/10.1038/nature13131.

51. Coen, P., Xie, M., Clemens, J., and Murthy, M. (2016). Sensorimotor Transformations Underlying Variability in Song Intensity during Drosophila Courtship. Neuron *89*, 629–644. https://doi.org/10.1016/j.neuron.2015.12.035.

52.Clemens, J., Coen, P., Roemschied, F.A., Pereira, T.D., Mazumder, D., Aldarondo, D.E., Pacheco, D.A., and Murthy, M. (2018). Discovery of a New Song Mode in *Drosophila* Reveals Hidden Structure in the Sensory and Neural Drivers of Behavior. Current Biology *28*, 2400-2412.e6. https://doi.org/10.1016/j.cub.2018.06.011.

53. Calhoun, A.J., Pillow, J.W., and Murthy, M. (2019). Unsupervised identification of the internal states that shape natural behavior. Nat Neurosci *22*, 2040–2049. https://doi.org/10.1038/s41593-019-0533-x.

54. Roemschied, F.A., Pacheco, D.A., Aragon, M.J., Ireland, E.C., Li, X., Thieringer, K., Pang, R., and Murthy, M. (2023). Flexible circuit mechanisms for context-dependent song sequencing. Nature, 1–8. https://doi.org/10.1038/s41586-023-06632-1.

55. Kravitz, E.A., and Huber, R. (2003). Aggression in invertebrates. Current Opinion in Neurobiology *13*, 736–743. https://doi.org/10.1016/j.conb.2003.10.003.

56. Huber, R., Smith, K., Delago, A., Isaksson, K., and Kravitz, E.A. (1997). Serotonin and aggressive motivation in crustaceans: Altering the decision to retreat. Proceedings of the National Academy of Sciences *94*, 5939–5942. https://doi.org/10.1073/pnas.94.11.5939.

57. Stevenson, P.A., Dyakonova, V., Rillich, J., and Schildberger, K. (2005). Octopamine and Experience-Dependent Modulation of Aggression in Crickets. J. Neurosci. *25*, 1431–1441. https://doi.org/10.1523/JNEUROSCI.4258-04.2005.

58. Rillich, J., Schildberger, K., and Stevenson, P.A. (2010). Octopamine and occupancy: an aminergic mechanism for intruder–resident aggression in crickets. Proc. R. Soc. B *278*, 1873–1880. https://doi.org/10.1098/rspb.2010.2099.

59. Stevenson, P.A., Hofmann, H.A., Schoch, K., and Schildberger, K. The Fight and Flight Responses of Crickets Depleted of Biogenic Amines.

60. Baier, A., Wittek, B., and Brembs, B. (2002). Drosophila as a new model organism for the neurobiology of aggression? J Exp Biol *205*, 1233–1240. https://doi.org/10.1242/jeb.205.9.1233.

61. Dierick, H.A., and Greenspan, R.J. (2007). Serotonin and neuropeptide F have opposite modulatory effects on fly aggression. Nat Genet *39*, 678–682. https://doi.org/10.1038/ng2029.

62. Asahina, K., Watanabe, K., Duistermars, B.J., Hoopfer, E., González, C.R., Eyjólfsdóttir, E.A., Perona, P., and Anderson, D.J. (2014). Tachykinin-Expressing Neurons Control Male-Specific Aggressive Arousal in Drosophila. Cell *156*, 221–235. https://doi.org/10.1016/j.cell.2013.11.045.

63. Watanabe, K., Chiu, H., Pfeiffer, B.D., Wong, A.M., Hoopfer, E.D., Rubin, G.M., and Anderson, D.J. (2017). A Circuit Node that Integrates Convergent Input from Neuromodulatory and Social Behavior-Promoting Neurons to Control Aggression in Drosophila. Neuron *95*, 1112-1128.e7. https://doi.org/10.1016/j.neuron.2017.08.017.

64. Hoopfer, E.D., Jung, Y., Inagaki, H.K., Rubin, G.M., and Anderson, D.J. (2015). P1 interneurons promote a persistent internal state that enhances inter-male aggression in Drosophila. eLife *4*, e11346. https://doi.org/10.7554/eLife.11346.

65. Chiu, H., Hoopfer, E.D., Coughlan, M.L., and Anderson, D.J. (2021). A circuit logic for sexually shared and dimorphic aggressive behaviors in Drosophila. Cell *184*, 507-520.e16. https://doi.org/10.1016/j.cell.2020.11.048.

66. Duistermars, B.J., Pfeiffer, B.D., Hoopfer, E.D., and Anderson, D.J. (2018). A Brain Module for Scalable Control of Complex, Multi-motor Threat Displays. Neuron *100*, 1474-1490.e4. https://doi.org/10.1016/j.neuron.2018.10.027.

67. Namiki, S., Dickinson, M.H., Wong, A.M., Korff, W., and Card, G.M. (2018). The functional organization of descending sensory-motor pathways in Drosophila. eLife *7*, e34272. https://doi.org/10.7554/eLife.34272.

68. Cande, J., Namiki, S., Qiu, J., Korff, W., Card, G.M., Shaevitz, J.W., Stern, D.L., and Berman, G.J. (2018). Optogenetic dissection of descending behavioral control in Drosophila. eLife *7*, e34275. https://doi.org/10.7554/eLife.34275.

69.Cheong, H.S., Eichler, K., Stürner, T., Asinof, S.K., Champion, A.S., Marin, E.C., Oram, T.B., Sumathipala, M., Venkatasubramanian, L., Namiki, S., et al. (2024). Transforming descending input into behavior: The organization of premotor circuits in the Drosophila Male Adult Nerve Cord connectome. eLife *13*. https://doi.org/10.7554/eLife.96084.1.

70. Dorkenwald, S., Matsliah, A., Sterling, A.R., Schlegel, P., Yu, S., McKellar, C.E., Lin, A., Costa, M., Eichler, K., Yin, Y., et al. (2024). Neuronal wiring diagram of an adult brain. Nature *634*, 124–138. https://doi.org/10.1038/s41586-024-07558-y.

71. Schlegel, P., Yin, Y., Bates, A.S., Dorkenwald, S., Eichler, K., Brooks, P., Han, D.S., Gkantia, M., dos Santos, M., Munnelly, E.J., et al. (2024). Whole-brain annotation and multi-connectome cell typing of Drosophila. Nature *634*, 139–152. https://doi.org/10.1038/s41586-024-07686-5.

72. Berg, S., Beckett, I.R., Costa, M., Schlegel, P., Januszewski, M., Marin, E.C., Nern, A., Preibisch, S., Qiu, W., Takemura, S., et al. (2025). Sexual dimorphism in the complete connectome of the Drosophila male central nervous system. Preprint at bioRxiv, https://doi.org/10.1101/2025.10.09.680999

73. Bates, A.S., Phelps, J.S., Kim, M., Yang, H.H., Matsliah, A., Ajabi, Z., Perlman, E., Delgado, K.M., Osman, M.A.M., Salmon, C.K., et al. (2026). Distributed control circuits across a brain-and-cord connectome. Nature, 1–4. https://doi.org/10.1038/s41586-026-10735-w.

74. Takemura, S., Hayworth, K.J., Huang, G.B., Januszewski, M., Lu, Z., Marin, E.C., Preibisch, S., Xu, C.S., Bogovic, J., Champion, A.S., et al. (2024). A Connectome of the Male Drosophila Ventral Nerve Cord. eLife *13*. https://doi.org/10.7554/eLife.97769.1.

75. Azevedo, A., Lesser, E., Phelps, J.S., Mark, B., Elabbady, L., Kuroda, S., Sustar, A., Moussa, A., Khandelwal, A., Dallmann, C.J., et al. (2024). Connectomic reconstruction of a female Drosophila ventral nerve cord. Nature *631*, 360–368. https://doi.org/10.1038/s41586-024-07389-x.

76. Tirian, L., and Dickson, B.J. (2017). The VT GAL4, LexA, and split-GAL4 driver line collections for targeted expression in the Drosophila nervous system. bioRxiv, 198648. https://doi.org/10.1101/198648.

77. Jenett, A., Rubin, G.M., Ngo, T.-T.B., Shepherd, D., Murphy, C., Dionne, H., Pfeiffer, B.D., Cavallaro, A., Hall, D., Jeter, J., et al. (2012). A GAL4-Driver Line Resource for Drosophila Neurobiology. Cell Reports *2*, 991–1001. https://doi.org/10.1016/j.celrep.2012.09.011.

78. Dionne, H., Hibbard, K.L., Cavallaro, A., Kao, J.-C., and Rubin, G.M. (2018). Genetic Reagents for Making Split-GAL4 Lines in Drosophila. Genetics *209*, 31–35. https://doi.org/10.1534/genetics.118.300682.

79. Meissner, G.W., Nern, A., Dorman, Z., DePasquale, G.M., Forster, K., Gibney, T., Hausenfluck, J.H., He, Y., Iyer, N.A., Jeter, J., et al. (2023). A searchable image resource of Drosophila GAL4-driver expression patterns with single neuron resolution. eLife *12*, e80660. https://doi.org/10.7554/eLife.80660.

80.Meissner, G.W., Vannan, A., Jeter, J., Close, K., DePasquale, G.M., Dorman, Z., Forster, K., Beringer, J.A., Gibney, T., Hausenfluck, J.H., et al. (2025). A split-GAL4 driver line resource for Drosophila neuron types. eLife *13*, RP98405. https://doi.org/10.7554/eLife.98405.

81.Cheong, H.S., Eichler, K., Stürner, T., Asinof, S.K., Champion, A.S., Marin, E.C., Oram, T.B., Sumathipala, M., Venkatasubramanian, L., Namiki, S., et al. (2025). Transforming descending input into motor output: An analysis of the Drosophila Male Adult Nerve Cord connectome. eLife *13*. https://doi.org/10.7554/eLife.96084.2.

82. Stürner, T., Brooks, P., Serratosa Capdevila, L., Morris, B.J., Javier, A., Fang, S., Gkantia, M., Cachero, S., Beckett, I.R., Marin, E.C., et al. (2025). Comparative connectomics of Drosophila descending and ascending neurons. Nature, 1–15. https://doi.org/10.1038/s41586-025-08925-z.

83. Bidaye, S.S., Machacek, C., Wu, Y., and Dickson, B.J. (2014). Neuronal Control of Drosophila Walking Direction. Science *344*, 97–101. https://doi.org/10.1126/science.1249964.

84. Bidaye, S.S., Laturney, M., Chang, A.K., Liu, Y., Bockemühl, T., Büschges, A., and Scott, K. (2020). Two Brain Pathways Initiate Distinct Forward Walking Programs in Drosophila. Neuron *0*. https://doi.org/10.1016/j.neuron.2020.07.032.

85. Zacarias, R., Namiki, S., Card, G.M., Vasconcelos, M.L., and Moita, M.A. (2018). Speed dependent descending control of freezing behavior in Drosophila melanogaster. Nat Commun *9*, 3697. https://doi.org/10.1038/s41467-018-05875-1.

86. Sapkal, N., Mancini, N., Kumar, D.S., Spiller, N., Murakami, K., Vitelli, G., Bargeron, B., Maier, K., Eichler, K., Jefferis, G.S.X.E., et al. (2024). Neural circuit mechanisms underlying context-specific halting in Drosophila. Nature *634*, 191–200. https://doi.org/10.1038/s41586-024-07854-7.

87. Sapkal, N., Kumar, D.S., Sunke, S., Mancini, N., Pitchford, J., Murakami, K., and Bidaye, S.S. (2026). Central versus peripheral neural control of a coordinated walking pattern in Drosophila. Preprint at bioRxiv, https://doi.org/10.64898/2026.04.29.721658 https://doi.org/10.64898/2026.04.29.721658.

88.Rayshubskiy, A., Holtz, S.L., Bates, A.S., Vanderbeck, Q.X., Capdevila, L.S., Rockwell, V., and Wilson, R.I. (2025). Neural circuit mechanisms for steering control in walking Drosophila. eLife *13*. https://doi.org/10.7554/eLife.102230.2.

89. Yang, H.H., Brezovec, B.E., Capdevila, L.S., Vanderbeck, Q.X., Adachi, A., Mann, R.S., and Wilson, R.I. (2024). Fine-grained descending control of steering in walking Drosophila. Cell *0*. https://doi.org/10.1016/j.cell.2024.08.033.

90. Feng, K., Gebehart, C., Trehan, R., Palieri, V., Zaman, Y., Hassel, K.A. van, Khan, M., Minegishi, R., Müller, A., Poll, M.N.V.D., et al. (2026). Hierarchical Transformation of Navigational Variables into Coordinated Turning. Preprint at bioRxiv, https://doi.org/10.1101/2024.06.27.601106 https://doi.org/10.1101/2024.06.27.601106.

91. Büschges, A., and Gorostiza, E.A. (2023). Neurons with names: Descending control and sensorimotor processing in insect motor control. Current Opinion in Neurobiology *83*, 102766. https://doi.org/10.1016/j.conb.2023.102766.

92. Simpson, J.H. (2024). Descending control of motor sequences in Drosophila. Current Opinion in Neurobiology *84*, 102822. https://doi.org/10.1016/j.conb.2023.102822.

93. Schnell, B., Ros, I.G., and Dickinson, M.H. (2017). A Descending Neuron Correlated with the Rapid Steering Maneuvers of Flying Drosophila. Current Biology *27*, 1200–1205. https://doi.org/10.1016/j.cub.2017.03.004.

94. Ros, I.G., Omoto, J.J., and Dickinson, M.H. (2024). Descending control and regulation of spontaneous flight turns in Drosophila. Current Biology *34*, 531-540.e5. https://doi.org/10.1016/j.cub.2023.12.047.

95. Suver, M.P., Huda, A., Iwasaki, N., Safarik, S., and Dickinson, M.H. (2016). An Array of Descending Visual Interneurons Encoding Self-Motion in Drosophila. J. Neurosci. *36*, 11768–11780. https://doi.org/10.1523/JNEUROSCI.2277-16.2016.

96. Kim, H., Park, H., Lee, J., and Kim, A.J. (2023). A visuomotor circuit for evasive flight turns in Drosophila. Current Biology *33*, 321-335.e6. https://doi.org/10.1016/j.cub.2022.12.014.

97. Buchsbaum, E., and Schnell, B. (2025). Activity of a descending neuron associated with visually elicited flight saccades in Drosophila. Current Biology *0*. https://doi.org/10.1016/j.cub.2024.12.001.

98.Croke, H., Jang, H., Ludlow, B.K., Leung, A., Eichler, K., Stürner, T., Costa, M., Cohen, I., Ausborn, J., and Von Reyn, C.R. (2026). Drosophila DNp03 descending neurons serve as a hub within a flight saccade network. Current Biology *36*, 133-150.e5. https://doi.org/10.1016/j.cub.2025.11.035.

99. Namiki, S., Ros, I.G., Morrow, C., Rowell, W.J., Card, G.M., Korff, W., and Dickinson, M.H. (2022). A population of descending neurons that regulates the flight motor of Drosophila. Current Biology *0*. https://doi.org/10.1016/j.cub.2022.01.008.

100. von Reyn, C.R., Breads, P., Peek, M.Y., Zheng, G.Z., Williamson, W.R., Yee, A.L., Leonardo, A., and Card, G.M. (2014). A spike-timing mechanism for action selection. Nature Neuroscience *17*, 962–970. https://doi.org/10.1038/nn.3741.

101.von Reyn, C.R., Nern, A., Williamson, W.R., Breads, P., Wu, M., Namiki, S., and Card, G.M. (2017). Feature Integration Drives Probabilistic Behavior in the Drosophila Escape Response. Neuron *94*, 1190-1204.e6. https://doi.org/10.1016/j.neuron.2017.05.036.

102. Dombrovski, M., Peek, M.Y., Park, J.-Y., Vaccari, A., Sumathipala, M., Morrow, C., Breads, P., Zhao, A., Kurmangaliyev, Y.Z., Sanfilippo, P., et al. (2023). Synaptic gradients transform object location to action. Nature *613*, 534–542. https://doi.org/10.1038/s41586-022-05562-8.

103. Ache, J.M., Namiki, S., Lee, A., Branson, K., and Card, G.M. (2019). State-dependent decoupling of sensory and motor circuits underlies behavioral flexibility in Drosophila. Nat Neurosci *22*, 1132–1139. https://doi.org/10.1038/s41593-019-0413-4.

104. Guo, L., Zhang, N., and Simpson, J.H. (2022). Descending neurons coordinate anterior grooming behavior in Drosophila. Current Biology *0*. https://doi.org/10.1016/j.cub.2021.12.055.

105. Braun, J., Hurtak, F., Wang-Chen, S., and Ramdya, P. (2024). Descending networks transform command signals into population motor control. Nature, 1–9. https://doi.org/10.1038/s41586-024-07523-9.

106. Zheng, Z., Lauritzen, J.S., Perlman, E., Robinson, C.G., Nichols, M., Milkie, D., Torrens, O., Price, J., Fisher, C.B., Sharifi, N., et al. (2018). A Complete Electron Microscopy Volume of the Brain of Adult Drosophila melanogaster. Cell *174*, 730-743.e22. https://doi.org/10.1016/j.cell.2018.06.019.

107. Scheffer, L.K., Xu, C.S., Januszewski, M., Lu, Z., Takemura, S., Hayworth, K.J., Huang, G.B., Shinomiya, K., Maitlin-Shepard, J., Berg, S., et al. (2020). A connectome and analysis of the adult Drosophila central brain. eLife *9*, e57443. https://doi.org/10.7554/eLife.57443.

108. Schlegel, P., Bates, A.S., Stürner, T., Jagannathan, S.R., Drummond, N., Hsu, J., Serratosa Capdevila, L., Javier, A., Marin, E.C., Barth-Maron, A., et al. (2021). Information flow, cell types and stereotypy in a full olfactory connectome. eLife *10*, e66018. https://doi.org/10.7554/eLife.66018.

109. Marin, E.C., Morris, B.J., Stürner, T., Champion, A.S., Krzeminski, D., Badalamente, G., Gkantia, M., Dunne, C.R., Eichler, K., Takemura, S., et al. (2024). Systematic annotation of a complete adult male Drosophila nerve cord connectome reveals principles of functional organisation. eLife *13*. https://doi.org/10.7554/eLife.97766.1.

110. Phelps, J.S., Hildebrand, D.G.C., Graham, B.J., Kuan, A.T., Thomas, L.A., Nguyen, T.M., Buhmann, J., Azevedo, A.W., Sustar, A., Agrawal, S., et al. (2021). Reconstruction of motor control circuits in adult Drosophila using automated transmission electron microscopy. Cell *0*. https://doi.org/10.1016/j.cell.2020.12.013.

111. Lesser, E., Azevedo, A.W., Phelps, J.S., Elabbady, L., Cook, A., Syed, D.S., Mark, B., Kuroda, S., Sustar, A., Moussa, A., et al. (2024). Synaptic architecture of leg and wing premotor control networks in Drosophila. Nature *631*, 369–377. https://doi.org/10.1038/s41586-024-07600-z.

112. Buhmann, J., Sheridan, A., Malin-Mayor, C., Schlegel, P., Gerhard, S., Kazimiers, T., Krause, R., Nguyen, T.M., Heinrich, L., Lee, W.-C.A., et al. (2021). Automatic detection of synaptic partners in a whole-brain Drosophila electron microscopy data set. Nat Methods *18*, 771–774. https://doi.org/10.1038/s41592-021-01183-7.

113. Ehrhardt, E., Whitehead, S.C., Namiki, S., Minegishi, R., Siwanowicz, I., Feng, K., Otsuna, H., Team, F.P., Meissner, G.W., Stern, D., et al. (2025). Single-cell type analysis of wing premotor circuits in the ventral nerve cord of Drosophila melanogaster. eLife *14*. https://doi.org/10.7554/eLife.106548.1.

114. Clements, J., Goina, C., Hubbard, P.M., Kawase, T., Olbris, D.J., Otsuna, H., Svirskas, R., and Rokicki, K. (2024). NeuronBridge: an intuitive web application for neuronal morphology search across large data sets. BMC Bioinformatics *25*, 114. https://doi.org/10.1186/s12859-024-05732-7.

115. Otsuna, H., Ito, M., and Kawase, T. (2018). Color depth MIP mask search: a new tool to expedite Split-GAL4 creation. bioRxiv, 318006. https://doi.org/10.1101/318006.

116. Mais, L., Hirsch, P., Managan, C., Wang, K., Rokicki, K., Svirskas, R.R., Dickson, B.J., Korff, W., Rubin, G.M., Ihrke, G., et al. (2021). PatchPerPixMatch for Automated 3d Search of Neuronal Morphologies in Light Microscopy. Preprint at bioRxiv, https://doi.org/10.1101/2021.07.23.453511

117. Hirsch, P., Mais, L., and Kainmueller, D. (2022). PatchPerPix for Instance Segmentation. Preprint at arXiv, https://doi.org/10.48550/arXiv.2001.07626 https://doi.org/10.48550/arXiv.2001.07626.

118. Bogovic, J.A., Otsuna, H., Heinrich, L., Ito, M., Jeter, J., Meissner, G., Nern, A., Colonell, J., Malkesman, O., Ito, K., et al. (2018). An unbiased template of the Drosophila brain and ventral nerve cord. bioRxiv, 376384. https://doi.org/10.1101/376384.

119. Zhang, Y., Rózsa, M., Liang, Y., Bushey, D., Wei, Z., Zheng, J., Reep, D., Broussard, G.J., Tsang, A., Tsegaye, G., et al. (2023). Fast and sensitive GCaMP calcium indicators for imaging neural populations. Nature, 1–8. https://doi.org/10.1038/s41586-023-05828-9.

120. Klapoetke, N.C., Murata, Y., Kim, S.S., Pulver, S.R., Birdsey-Benson, A., Cho, Y.K., Morimoto, T.K., Chuong, A.S., Carpenter, E.J., Tian, Z., et al. (2014). Independent optical excitation of distinct neural populations. Nat Methods *11*, 338–346. https://doi.org/10.1038/nmeth.2836.

121. Mohammad, F., Stewart, J.C., Ott, S., Chlebikova, K., Chua, J.Y., Koh, T.-W., Ho, J., and Claridge-Chang, A. (2017). Optogenetic inhibition of behavior with anion channelrhodopsins. Nat Methods *14*, 271–274. https://doi.org/10.1038/nmeth.4148.

122. Govorunova, E.G., Sineshchekov, O.A., Li, H., Wang, Y., Brown, L.S., and Spudich, J.L. (2020). RubyACRs, nonalgal anion channelrhodopsins with highly red-shifted absorption. Proceedings of the National Academy of Sciences *117*, 22833–22840. https://doi.org/10.1073/pnas.2005981117.

123. Bushey, D., Shiozaki, H., Shuai, Y., Zheng, J., Jayaraman, V., Hasseman, J.P., Kolb, I., Team, G.P., and Turner, G.C. (2025). RubyACRs Enable Red-Shifted Optogenetic Inhibition in Freely Behaving Drosophila. eLife *14*. https://doi.org/10.7554/eLife.108210.1.

Chapter 2

NEURAL CONTROL OF COORDINATED WING AND LEG MOVEMENTS DURING A TERRESTRIAL THREAT DISPLAY

Cao, S., and Anderson, D.J. (2025). "Neural control of coordinated wing and leg movements during a terrestrial threat display". Preprint at bioRxiv, https://doi.org/10.1101/2025.10.25.684556

Summary

In most flying species, legs and wings mediate terrestrial vs. aerial locomotion, respectively. During social displays such as threat or courtship, however, species-typical movements of these appendages are combined and coordinated in a stereotyped manner to communicate the intent to attack or mate. How this integrated appendicular control is achieved is not well understood. Previously we identified a cluster of 4-5 AIP neurons in *Drosophila* whose optogenetic activation can evoke threat behavior comprising four types of leg or wing actions. AIP neurons are essential for natural threat behavior but dispensable for other aggressive actions such as lunging, thereby constituting a dedicated command module for threat displays. To understand how this module functions, we have mapped AIP neurons into the male fly connectome and identified split-Gal4 drivers for four major downstream targets, whose functional connectivity and behavioral roles we have tested singly and in combination. Surprisingly, we find that distinct threat-specific actions are not controlled by parallel downstream pathways under the control of different AIP subtypes, as might have been anticipated. Rather, AIP neurons collectively activate two pairs of neurons that act synergistically vs. antagonistically to control wing vs. leg movements, respectively. Wing

movements are controlled via direct AIP projections to dedicated descending neurons, while leg movements are controlled indirectly via interneurons that control DNs likely used in other contexts. These data elucidate the circuit logic controlling a terrestrial social display and provide insight into how the brain has repurposed appendage-specific locomotor control for social communication.

Introduction

Social displays are communicative behaviors prevalent across the animal kingdom and play a crucial role in encounters such as mating, aggression, and defense[1–9]. A key feature of these displays is that they comprise multiple actions involving the coordinated use of distinct body parts. For instance, during a threat display, elephants spread their ears, raise or swing their trunks, shake or nod their heads, and stomp their feet. The precise coordination of these movements is vital for effective social signaling. While significant progress has been made in identifying neural nodes that control complex social behaviors at a more holistic level[10–15], much less is known about how individual actions involving distinct appendages are orchestrated to produce complex social behaviors.

This problem is of particular interest in flying species that exhibit terrestrial social displays combining coordinated, stereotyped movements of the wings and legs, appendages which are otherwise utilized independently for aerial and earthbound locomotion. Threat display by *Drosophila* males is an aggressive or agonistic behavior, composed of at least four distinct actions: wing elevation, pump, turn, and charge[16]. Wing elevation comprises an abrupt bilateral upward wing movement to an angle of 45º, which is then sustained for seconds (Figure 1Ai). Pump is a transient (<0.1 s) bilateral horizontal wing extension towards

90º (Figure 1Aii). Turns and charges are both transient and discrete locomotor events that are performed as the fly rapidly orients and accelerates toward its opponent (Figure 1Aiii and 1Aiv). These actions can occur in various combinations: stable wing elevation can be performed with or without turns and/or charges, while a pump is always accompanied by turning and charging[16]. Together these movements visually communicate a larger size and aggressive intent to a male conspecific. This behavioral complexity necessitates a sophisticated neural control mechanism to flexibly utilize and coordinate wing and leg movements during such threat displays.

Previously, we identified a small cluster of genetically labeled interneurons (INs) in the central brain, termed "AIP", using an unbiased functional activation screen for aggression-promoting neurons[15–17]. Unlike other aggression-promoting neurons identified to date[15,18–25], the AIP cluster specifically controls only wing threat behavior. Silencing AIP neurons suppresses natural wing threat displays without impairing contact-mediated aggressive behaviors such as lunging, tussling, or boxing[16,26]. Conversely, optogenetic activation of AIP neurons elicits the full complement of threat actions in solitary flies[16]. These data identify AIP as a crucial command center for coordinating threat displays. However, how the activity of AIP neurons is flexibly routed to orchestrate the distinct behavioral actions that comprise these displays remains unknown.

To address this question, we have investigated the logic of threat circuit organization and function downstream of the AIP cluster. Using EM connectomics and functional imaging, we find that, surprisingly, distinct threat-specific actions are not controlled by parallel downstream pathways under the control of different AIP subtypes, as might have been anticipated. Rather, AIP neurons provide both direct and indirect feedforward input to

distinct sets of descending neurons (DNs) controlling the wings or legs, respectively. Through optogenetic and behavioral analysis with cellular epistasis tests, we show that the direct pathway comprises two apparently dedicated DNs that synergistically control wing elevation and pump. In contrast, the indirect pathway comprises two functionally antagonistic INs, whose conjoint activity controls a different group of DNs that mediate leg-based threat actions, but which are likely also used in other locomotor contexts. Together, these findings reveal a hierarchical and combinatorial circuit logic for the coordination of wing and leg movements during a terrestrial social display, and provide new insights into how the brain has repurposed appendicular locomotor control for social communication, an example of exaptation at the behavioral level[27].

Results

Identifying the AIP downstream circuit in a male central nervous system (CNS) connectome

Since AIP neurons are INs located in the central brain, they likely promote wing threat actions by engaging downstream circuits that channel AIP activity into distinct motor pathways, ultimately via the activation of various types of DNs. *A priori* several models could explain the coordination of different appendicular movements. At one extreme, the AIP cluster could comprise different neuronal subtypes, each of which controls a distinct motor action via distinct DNs (Figure 1Bi). Such a model would provide maximal flexibility in orchestrating different combinations of threat actions. At the opposite extreme, each AIP neuron could contribute to the control of all four threat actions, perhaps generating flexible action combinations via connections of different synaptic strengths to different DNs (Figure

1Bii, different arrow thicknesses). Between these extremes, various types of hierarchical models are possible (Figure 1Biii-iv).

To address this question, we first mapped AIP neurons, labeled by a specific split-GAL4 driver line[16] (Figure 1Ci), into a male CNS connectome[28,29] (https://neuprint.janelia.org/, male-cns:v0.9) and identified five neurons per hemisphere with morphological resemblance to the genetically labeled AIP neurons (CL062, Figure 1Cii).

Using the connectome, we then mapped the major downstream targets of these five paired AIP neurons (Figure 1D). There are 45 neuron types that receive more than 40 synapses from AIP (Figure 1Di). The downstream neuron types include both DNs (e.g. DNpe050), and INs (e.g. AVLP710m) (Figure 1Di). 80% of these downstream neuron types are INs and they account for more than 75% of total AIP synaptic output. Hierarchical clustering based on downstream connectivity revealed two subsets of AIP neurons (CL062a,b; Figure S1A), but those subsets projected to highly overlapping downstream targets, differing primarily in the number of synapses for each connection, particularly among the top downstream targets (Figure S1B). Notably, the major direct IN targets of AIP, AVLP491 and AVLP710m, project heavily to DNs, thus mediating an indirect output from AIP to DNs (Figure 1E). The circuit diagram downstream of AIP reveals a largely feed-forward network in which a small number of DNs receive direct synaptic input from AIP while a larger number of DNs receive indirect inputs via an intervening layer of INs (Figure 1F and S1C). Together, these data immediately excluded models in which different AIP neurons each control one of the four distinct threat motor actions by projecting to different DNs, or in which all AIP neurons fan out to directly engage a common set of DNs in parallel, without an intervening layer of INs (Figure 1Bi, ii).

These connectomic data suggested additional types of hierarchical models for the control of threat actions by AIP neurons (Figure 1Biii and 1Biv), where some or all threat-related DNs are coordinated by INs to control subsets of actions. To differentiate among these and other models, it was necessary to gain genetic access to individual AIP downstream targets. Using NeuronBridge[30–35], we screened a total of ~70 split-GAL4 lines (Figure S1D) and were able to identify specific drivers for DNpe050, DNp60, AVLP491, and AVLP710m (Figure 1F). As described below, all of these drivers labeled cells that exhibited behavioral phenotypes in silencing or activation experiments and/or calcium responses to AIP stimulation. Although AIP neurons also project to some other classes of INs or DNs (Figure 1D), we excluded those from further analysis either because we were unable to identify clean genetic drivers for those cells, or because the neurons (VES041[36]) did not reveal calcium responses to AIP activation, or functional effects on threat behavior.

DNpe050 activation increases the probability of wing elevation

DNpe050 is a DN that receives the strongest monosynaptic input from AIP among all identified DN targets (Figure 1D, 2Ai and 2Aii) and is predicted[37] to be cholinergic based on the connectome. An initial round of screening identified a split-GAL4 that labeled DNpe050 (VT058429-AD, 12G09-DBD), along with approximately 40 additional neurons per hemisphere. To reduce off-target labeling, we performed enhancer dissection[22,38,39] of both hemi-drivers (Figure S2A, also see Methods) and tested 10 different combinations of enhancer fragments and one of the parental drivers (Figure S1D, DNpe050 EB drivers). Two of these newly created hemi-drivers, VT058429EB1-AD and 12G09EB3-DBD, retained expression in DNpe050 when combined, but labeled only ~10-15 additional neurons. Further

screening using these enhancer-bashed hemi-drivers and additional hemi-drivers from NeuronBridge (Figures S1D, DNpe050 second round) yielded several split-GAL4 combinations of which four, including DNpe050-split1 and DNpe050-split2, were further characterized. When triply intersected with Otd-FLP[21] to eliminate ventral nerve cord (VNC) expression, DNpe050-split1 labeled only 2-3 off-target neurons (Figure 2B and S2Bi) while DNpe050-split2 labeled a group of approximately 5-8 off-target neurons distinct from those labeled by DNpe050-split1 (Figure S2Bii).

To confirm the connectome-predicted functional connectivity between AIP and DNpe050, we used two-photon microscopy to measure GCaMP fluorescence in DNpe050 during wide-field optogenetic activation of AIP neurons in head-fixed, living flies. Robust fluorescence increases were observed during photostimulation (Figure 2C), verifying that DNpe050 is functionally downstream and activated by AIP. The calcium response was absent in the genetic control group, which lacked the AIP driver but underwent the same LED illumination (Figure S2Biii), suggesting that the observed response was not due to visual response to LED or leakage expression of Chrimson.

Next, we examined the behavioral function of DNpe050 by optogenetically activating the labeled cells in freely moving solitary animals that were reared group-housed, thus non-aggressive and not exhibiting spontaneous wing threat behavior. Under high-frequency (40 Hz) photostimulation, activation of DNpe050-split1 elicited stable wing elevation (defined by the criterion that both wings were elevated at between 35° and 65° for >0.2 s) (Figure 2Di), in approximately 10-15% of flies (Figure 2Dii). The penetrance (defined as the fraction of flies showing at least 1 instance of the behavior of interest during

photostimulation) was consistent across various light intensities and frequencies with both DNpe050-split1 and DNpe050-split2 (Figure S2Ci, iii). Among responsive flies, the expressivity (defined as the percentage of the photostimulation period during which the behavior was performed) of wing elevation was highly variable but averaged approximately 10-40% (Figure 2Diii, and S2Cii, iv). Activation of DNpe050-split drivers did not elicit consistent changes in turning, charging, or pumping (Figure S2D).

To test the necessity of DNpe050 for AIP-driven behaviors, we performed epistasis experiments, in which AIP neurons were optogenetically activated with CsChrimson using a LexA driver, while DNpe050 was silenced using split-GAL4 and Otd-FLP[21] to drive brain-restricted expression of the inwardly rectifying potassium channel Kir2.1[40] (Figure 2E and S2Biv). Silencing DNpe050 significantly suppressed AIP-elicited wing elevation (Figure 2Ei) and pumping (Figure 2Eii) but did not affect turning (Figure 2Eiii) or charging (Figure 2Eiv). Finally, we investigated whether DNpe050 is required for natural wing threat displays. Silencing DNpe050 using Kir2.1 and either of the two DNpe050-split drivers in pairs of single-housed male flies (which exhibit spontaneous wing threat behaviors) caused consistent reductions in the fraction of time flies performed wing elevation (Figure 2Fi), and in the average bout duration of wing elevation (Figure 2Fii). The frequency of wing elevation (Figure 2Fiii) and pump (Figure 2Fiv) were reduced in DNpe050-split1 but not or only mildly in split2. Turning (Figure 2Fv) and charging (Figure 2Fvi) during wing threat were not reduced. Lunging (Figure S2Ei) and general locomotion (Figure S2Eii) were not significantly different, suggesting that the reduction in wing elevation is not due to decreased overall aggressiveness or vigor.

Collectively, these results suggest that DNpe050 is required for both wing elevation and pump during threat display, while its activation promotes wing elevation but only at low penetrance. Such a phenotypic pattern suggests that at least one additional neuronal type must be activated together with DNpe050 to evoke wing threat displays. Below we provide evidence in support of this interpretation.

DNp60 elicits pump and wing elevation

We next investigated the function of DNp60, another DN that, like DNpe050, receives direct input from AIP (Figure 3A) and is predicted to be cholinergic by the connectome. By screening combinations of hemi-drivers suggested by NeuronBridge (Figure S1D), we identified two split-GAL4 drivers for DNp60, DNp60-split1 (Figure 3B and S3Ai) and DNp60-split2 (Figure S3Aii). We again confirmed that DNp60 is functionally downstream of AIP by optogenetically activating the latter while imaging calcium transients in the former (Figure 3C and S3Aiii). Interestingly, stimulation of AIP activated DNp60 more strongly than it did DNpe050 (Figure 2C), although the connectome predicted ~11-fold more synapses from AIP onto the latter vs the former (Figure 1Di).

Next, we investigated the behavioral phenotype elicited by DNp60 optogenetic activation. Medium-frequency (10 Hz) activation of DNp60 elicited pumps (Figure 3D), most of which occurred during the early phase of a trial (Figure 3Di). Pumps occurred in ~50% of stimulated flies (Figure 3Dii), with a median frequency of ~0.5 pump/s per responsive fly (Figure 3Diii). Higher LED frequencies and intensities did not further increase the penetrance or expressivity (pump count per responsive fly) (Figure S3Bi-ii). DNp60 activation also elicited wing elevation early in the stimulation period, with ~25% penetrance

and ~20% expressivity (Figure 3E). Penetrance of wing elevation increased with LED frequencies and intensities, but saturated at ~25%, while expressivity remained constant among responsive flies (Figure S3Biii-iv). Turning and charging were not elicited by DNp60 activation (Figure S3C).

To assess whether DNp60 is necessary for any AIP-induced wing threat actions, we conducted epistasis experiments in which DNp60 was silenced while AIP neurons were optogenetically activated (Figure 3F and S3Aiv). Silencing DNp60 significantly reduced AIP-elicited wing elevation (Figure 3Fi) and pump (Figure 3Fii) for both DNp60-split drivers. Turning was reduced only with DNp60-split1 but not with DNp60-split2 (Figure 3Fiii), likely due to off-target labeling in the former line. Charging was unaffected (Figure 3Fiv). Silencing DNp60 in pairs of interacting aggressive flies did not lead to any detectable reduction in natural wing threat actions (Figure S3D), perhaps reflecting redundancy with DNpe050.

Together, these results reveal that DNp60 is able to elicit pump and wing elevation with moderate penetrance and low expressivity and is necessary for AIP-induced wing elevation and pump.

DNpe050 and DNp60 synergistically control wing elevation and pump

Since DNpe050 activation can weakly evoke wing elevation and DNp60 activation evokes both pump and wing elevation, and since each is necessary for AIP-induced wing actions, we hypothesized that coactivating DNpe050 and DNp60 in the same flies might enhance the penetrance and expressivity of wing elevation and pump.

To test this, we generated compound-genotype flies carrying both DNpe050-split1 and DNp60-split1 (Figure S4A) and compared the behavioral phenotypes of DNpe050 and DNp60 coactivation to those of single-neuron-type activation (Figure 4A-C). At low frequency (2 Hz) photostimulation, DNpe050 activation alone triggered few stable wing elevation bouts (Figure 4Bi) and no pumps (Figure 4Ci). DNp60 activation alone elicited pumps and wing elevation, primarily during the initial light pulses of a trial (Figure 4Bii and 4Cii). In striking contrast, coactivation of DNpe050 and DNp60 induced rapid wing extension at each light pulse and maintained wings at an open angle between pulses (Figure 4Aiii), producing wing elevation that was sustained during the inter-pulse intervals (Figure 4Biii) and pumps across multiple photostimulation pulses throughout a trial (Figure 4Ciii). Coactivation significantly increased both penetrance (Figure 4Di) and expressivity (Figure 4Dii) of stable wing elevation relative to DNpe050 alone. Compared to DNp60 activation alone, coactivation showed equivalent pump and wing elevation penetrance (Figure 4Di and 4Ei), but significantly higher expressivity (Figure 4Dii and 4Eii). The expressivities of wing elevation and pump induced by coactivation exceeded the linear summation of those induced by single-neuron-type activation (Figure 4Dii and 4Eii, red dashed line), suggesting a synergistic interaction. Importantly, coactivation of DNp60 and DNpe050 phenocopied AIP activation for both wing elevation and pump in terms of the magnitude of penetrance and expressivity (Figure 4D and 4E, AIP).

To investigate further the synergy between DNpe050 and DNp60, we repeated the experiments using high frequency (40 Hz) photostimulation. Under these conditions, coactivation similarly increased penetrance (Figure S4Bi) and expressivity (Figure S4Bii) of wing elevation relative to either driver alone. However, pump was less effectively elicited

by activation of any driver tested at 40 Hz than it was at 2 Hz, including that of AIP. This ceiling effect likely precluded a significant coactivation improvement for pump (Figure S4Biii and S4Biv). To rule out the possibility that the observed behavioral effects were due to off-target neuron activation or synergistic effects between off-targets neurons and DNpe050/DNp60, we repeated the coactivation experiments using DNp60-split2 combined with four different DNpe050 split-GAL4 lines, each with distinct off-target patterns (Figure S4A). Similar results were obtained under both 2 Hz (Figure S4C) and 40 Hz stimulation (Figure S4D).

Taken together, these data suggest that DNpe050 and DNp60 act synergistically to promote wing elevation and pump, and their coactivation can recapitulate the wing actions driven by AIP. The synergistic behavioral effect may result from reciprocal connectivity between DNpe050 and DNp60, or from their convergent input onto common downstream targets (see Discussion).

AVLP491 induces locomotion and is necessary for AIP-elicited threat locomotor actions

We focused next on the function of INs AVLP710m and AVLP491 (Figure 5A and 6A), both of which receive direct synaptic input from AIP neurons and in turn project to multiple DNs. Based on the connectome, AVLP491 is predicted to be cholinergic. To investigate the function of AVLP491, we identified two split-GAL4 drivers, AVLP491-split1 (Figure 5B and S5Ai) and AVLP491-split2 (Figure S5Aii). Calcium imaging confirmed that AVLP491 is functionally downstream of AIP (Figure 5C and S5Aiii), consistent with the projection suggested by the connectome.

To minimize baseline locomotion during the light-off period and startle-induced locomotion during the light-on period, we performed optogenetic activation of AVLP491 in flies dusted with powder in the presence of dim green backlighting[41,42]. Optogenetic activation of AVLP491 induced locomotion in freely moving flies, with an increase in both forward (Figure 5D and S5C) and angular velocity (Figure 5E and S5D), respectively. Locomotion induced by AVLP491 activation was also temporally correlated across individuals. AVLP491-activated flies showed high Pearson correlation coefficients in forward (Figure S5E) and angular (Figure S5F) velocities across both AVLP491-split drivers. Notably, activating AVLP491 did not induce any wing elevation or pump (Figure S5B). Therefore, AVLP491 activation specifically induced leg-based locomotion.

In epistasis experiments, silencing AVLP491 significantly suppressed AIP-induced turning and charging (Figure 5Fi, 5Fii, and S5Aiv), indicating a requirement of these neurons for leg-mediated threat actions. Epistatic silencing of these cells did not reduce AIP-evoked wing elevation (Figure 5Fiii). However, we observed a significant reduction in pump (Figure 5Fiv). This effect could reflect the fact that pump is frequently accompanied by turns and charges[16], suggesting that the execution of pump might require activation of, or proprioceptive feedback from the legs. Silencing AVLP491 in pairs of spontaneously aggressive flies using either of the two split-GAL4 drivers and Kir2.1 did not lead to any consistent reduction in threat actions, including turning or charging (Figure S5G). This could reflect either insufficient penetrance or expressivity of silencing by the Kir2.1 effector or redundant circuits downstream of, or in parallel with, AIP neurons (Figure 1D).

Together, these data suggest that AVLP491 can enhance forward and angular locomotion, and is necessary for AIP-elicited turning and charging.

AVLP710m inhibits AVLP491-induced locomotion

AVLP710m is a major IN target of AIP besides AVLP491 that projects directly to DNs (Figure 6A). We identified a split-GAL4 driver (Figure 6B) for AVLP710m. Fluorescence *in situ* hybridization using HCR3.0[43] amplification revealed that AVLP710m expresses VGAT but not ChAT (Figure S6A), indicating it is an inhibitory interneuron. Although the connectome suggests over 1,000 synapses between AIP and AVLP710m (Figure 6A), we did not detect significant calcium responses in AVLP710m when AIP was photostimulated in head-fixed preparations (data not shown). AVLP710m receives in total around 15,000 input synapses from over 500 other neurons, which may include tonic inhibitory input that overrides AIP activation. However, the perfusion of picrotoxin did not uncover cryptic responses to AIP stimulation (data not shown). The lack of response may be because AVLP710m is sensitive to the state of the fly and could not be successfully activated by AIP under restrained open-cuticle conditions; however direct activation of AVLP710m neurons co-expressing GCaMP yielded clear stimulus-locked signals indicating these cells are capable of spiking under these conditions (data not shown).

Next, we used direct optogenetic activation of AVLP710m to probe its behavioral function. At an LED intensity of 0.38 mW/mm^2 and frequencies of 5, 10, 25, and 40 Hz the experimental flies did not display any significant differences from the genetic controls in forward or angular velocity (Figure 6C and 6D). However, when the LED intensity was doubled (0.78 mW/mm^2), stimulation of AVLP710m at 40 Hz significantly reduced both forward and angular velocity evoked by light-induced startle (Figure S6C), suggesting that AVLP710m can suppress generic locomotion only when strongly activated.

Given that both AVLP491 and AVLP710m influence locomotion and are required for AIP-driven turning and charging, we hypothesized that they may work together to pattern threat locomotor actions. To test this hypothesis, we performed coactivation experiments at low intensity (0.38 mW/mm^2) (Figure 6E-F and S6Bi). AVLP491 activation alone evoked increased locomotion at all frequencies tested (Figure 6E and 6F, blue traces). However, at 10 Hz or above, coactivation with AVLP710m abolished this increase (Figure 6Eii-v and 6Fii-v, orange traces). Similar results were obtained with AVLP491-split2 (Figure S6D-E and S6Bi). Given that AVLP710m has a high stimulation threshold for suppressing general locomotion (Figure 6C-D and S6C, 0.78 mW/mm^2, 40 Hz), but a much lower threshold for suppressing AVLP491-induced locomotion (Figure 6E-F, 0.38 mW/mm^2, 10 Hz), these results suggest a specific antagonistic interaction between AVLP491 and AVLP710m. Consistent with this notion, connectomic data show that AVLP491 and AVLP710m project to overlapping DNs (Figure S6G), including DNg100 and DNge050, which are functionally implicated in locomotion[41,44]. This suggests that their functional antagonism may result from converging input onto common direct downstream targets.

To test AVLP710m's necessity for AIP-evoked threat behaviors, we silenced it in epistasis experiments (Figure 6G and S6Bii). AVLP710m silencing using Kir2.1 significantly suppressed AIP-induced turning (Figure 6Gi), charging (Figure 6Gii), and pump (Figure 6Giv), but did not affect wing elevation (Figure 6Giii). This suggests that although direct AVLP710m activation can suppress general locomotion, its constitutive inhibition reduces AIP-evoked transient, discrete bouts of turning and charging. However, in single-housed males performing spontaneous threat behavior silencing AVLP710m did not reduce natural turning and charging (Figure S6Fv, vi). This could reflect redundancy among

locomotion-related circuits controlling naturalistic threat (Figure 1D) or insufficient inhibition of AVLP710m in this naturalistic setting. Nevertheless, a mild reduction in wing elevation was observed (Figure S6Fi, ii), while general locomotion was slightly increased (Figure S6Fviii).

Taken together, these data indicate that AVLP710m is necessary for AIP-induced turning and charging and functions in conjunction with AVLP491 to regulate locomotion.

Temporally patterned AVLP491 and AVLP710m coactivation recapitulates AIP-induced turn and charge-like behavior

Turns and charges in the context of threat are performed as transient, discrete bouts of locomotion[16]. AIP activation mimics this pattern, eliciting brief, punctuated turns and charges, even during constant LED stimulation (Figure 7Ai-ii). In contrast, AVLP491 activation alone leads to sustained locomotion (Figure 5D-E and S5C-D), while its coactivation with AVLP710m leads to continuous immobility (Figure 6F-G and S6D-E). Despite these contrasting results, both AVLP491 and AVLP710m are required for AIP-induced turning and charging (Figure 5F and 6G). How, then, does AIP generate transient, discrete locomotor bouts through these neurons?

We hypothesized that while AIP activities provide overall initiation and coordination of threat behavior, AVLP491 and AVLP710m may shape the temporal structure of locomotor bouts. If true, their activation frequency should match the dynamics of turning and charging, which is constrained by the physical limitation of motor execution. We therefore tested this by coactivating AVLP491 and AVLP710m at 3 Hz, a frequency comparable to the turning and charging frequency observed during AIP activation under constant light

(Figure 7Ai-ii). Surprisingly, coactivation at 3 Hz produced transient bouts in both forward (Figure 7Aiii) and angular (Figure 7Biii, iv) velocities time-locked to the stimulation pulses.

The turns and charges observed during both natural and AIP-evoked threat are exhibited as brief bouts of forward and angular locomotion, interspersed with periods of immobility[16]. Similarly, the transient bouts of movement produced by co-activation of AVLP491 and AVLP710m were also interleaved with periods of apparent immobility (Figure 7Biii, iv). To quantify this directly, we measured the probability of immobility (defined as periods during which forward velocity is < 1mm/s and angular velocity is < 10°/s)[16] during coactivation. Strikingly, in flies coactivated at 3 Hz, bouts of locomotion were interspersed with regular periods of immobility (Figure 7D). This "stuttering" locomotion pattern closely resembled the turns and charges elicited by AIP activation at the same frequency (Figure 7E) and was notably absent when either driver was activated alone (Figure 7B and 7C). We further quantified the total time, frequency, and average bout duration of immobility (Figure 7Fi-iii). Flies co-activated with AVLP491 and AVLP710m displayed an intermediate percentage of time immobile compared to AVLP491 or AVLP710m activation alone (Figure 7Fi), but a high frequency of immobility (Figure 7Fii) and low average bout durations (Figure 7Fiii), similar to that observed with AIP activation (Figure 7Fi-iii).

The temporal dynamics of occurrence of immobility also displayed a "stuttering"-like periodicity. Therefore, we further performed a Fourier transformation on the occurrence of immobility during the photo-stimulation period, and extracted the power at the LED frequency, normalized to the total power, denoted as a "stuttering" score. The co-activation of AVLP491 and AVLP710m yielded a significantly higher "stuttering" score than

activation of AVLP491 or AVLP710m alone (Figure 7Fiv). Quantification of turn- and charge-like bouts showed that coactivation of AVLP491 and AVLP710m significantly increased the frequency of these actions relative to AVLP491 or AVLP710m alone (Figure 7G).

In summary, low-frequency coactivation of AVLP491 and AVLP710m recapitulated the temporal pattern of AIP-induced threat locomotion, generating short bouts of locomotion bounded by periods of immobility, a pattern not observed with activation of either IN alone. These findings suggest that AVLP491 and AVLP710m act in combination to generate and temporally pattern the threat locomotor actions mediated by the legs.

Discussion

How the brain has repurposed appendages that evolved for aerial and terrestrial locomotion to generate communicative social displays is poorly understood. In this study, we identified a hierarchical circuit containing four newly characterized cell types that collectively mediate the actions comprising threat displays evoked by stimulation of AIP neurons (Figure 7H). DNpe050 and DNp60, two direct DN targets of AIP, synergistically control wing elevation and pump, while AVLP491 and AVLP710m, two functionally antagonistic INs projecting to overlapping but distinct populations of DNs, coordinatively control threat locomotor actions, i.e., rapid orientation (turning) and acceleration (charging) towards the opponent fly. These findings suggest that appendicular control during threat display, as driven by AIP activation, is mediated by specialized downstream functional neural modules that use combinatorial coding to coordinate distinct wing- and leg-mediated

actions. They also reveal a fundamentally different circuit logic from the simpler models that intuition might suggest (Figure 1B).

Appendage-specific modules for action control

AIP output is organized hierarchically into two different appendage-specific modules: one controlling wing actions and the other regulating leg actions. The former actions are mediated by direct projections to DNs, while the latter are mediated by indirect projections via an intervening layer of INs. This difference in circuit organizational logic likely reflects different neural control requirements for these two types of appendages, as well as evolutionary history.

Wing threat actions are relatively stereotyped. During wing elevation, wings typically are raised to a fixed 45° angle and remain there. During a pump both wings are briefly expanded to approximately 90°. Thus, unlike flying or singing which involves flexible and dynamic control of the wings[45,46], threat displays involve "one-shot" changes in wing postures. Such stereotyped wing postures may require fast, reliable triggering by dedicated DNs, making direct monosynaptic AIP-to-DN connectivity advantageous. From an evolutionary perspective, wing threat and pump are so different from wing movements during flight that it makes intuitive sense to invent a small number of new DNs dedicated to the control of this behavior, analogous to pIP10 neurons for courtship song.

In contrast to wing movements during threat, locomotion is prevalent in various behavioral contexts and can exhibit different modes[42,47–51]. Flies can walk backwards[47,48], follow a target[42,50], walk straight[42], pivot, and swerve[49], which can be driven by single

neuronal types or by the coordinated activity of multiple neuronal types. DNs controlling the legs may participate in a broad set of walking-related motor programs. The presence of an intermediate IN layer downstream of AIP allows for two key forms of circuit control: 1) recruiting the appropriate DN population to produce a motor action specific for a particular behavioral display — a "corralling" function — and 2) shaping the temporal dynamics of DN activity to generate appropriately timed and structured outputs — a "sculpting" function. Although the four types of threat actions are relatively stereotyped, turning and charging are inherently dynamic, with direction, speed, and bout duration modulated by the fly's orientation and distance relative to its opponent. Their execution likely depends on real-time sensory input to guide and adjust the trajectory of the movement. The layered AIP-IN-DN architecture could facilitate these dynamics by allowing sensory signals to modulate circuit activity at multiple stages. From an evolutionary standpoint, it seems simpler to use INs to co-opt DNs that control leg movements in other locomotor contexts and shape their dynamics to achieve the abrupt turns and charges that characterize threat, than to invent new DNs dedicated to the control of those actions.

Overall, segregating wing and leg control into sub-modules specialized for threat enables tailored neural strategies, ensuring precise and efficient execution of actions with different functional demands while still coordinating these actions into an ethologically meaningful communicative display.

Combinatorial control of threat-specific appendage movements

A principal and surprising finding of our analysis is that individual downstream target neurons of AIP are not dedicated to single threat actions, as one might have assumed (Figure

1B). Instead, they function in a combinatorial manner to control appendage-specific actions. This observation corroborates recent reports that DNs may control behaviors using population coding[36,52–54].

In the wing module, DNpe050 and DNp60 act synergistically to promote both wing elevation and pumping. When activated individually, each neuron elicits one or both actions, but with low penetrance and expressivity. In contrast, their coactivation significantly enhances expressivity of pumping and the penetrance and expressivity of wing elevation. This synergy could be an idiosyncratic feature of optogenetic activation, or it could be used by the system during natural threat behavior. In the latter case, synergy between the two DNs could allow the setting of different thresholds for different behaviors and/or offer greater flexibility of coupling to leg actions[16]. Where and how this synergy is implemented is not clear. In the central brain, connectomic data suggest that there is no direct connection between DNpe050 and DNp60. In the VNC, we identified only one high-ranking direct downstream target (IN19B007) shared by DNpe050 and DNp60 (Figure S7Ai). However, there is extensive interconnectivity between the first-order downstream targets of these two DNs in the VNC (Figure S7Aii), suggesting that the synergy might occur at this level.

In contrast to the direct activation by AIP of DNs for wing threat movements, DNs controlling turning and charging (Figure S6G) are indirectly controlled by AIP cells via two antagonistic INs with opposite influences: AVLP491 is excitatory and promotes locomotion, while AVLP710m is inhibitory and can effectively and specifically suppress AVLP491-elicited locomotion. The connectome identified at least five DNs on which AVLP491 and AVLP710m make convergent excitatory and inhibitory synapses, providing a plausible neural substrate for such antagonistic control. However, AVLP491 also excites at least four

other DNs that do not receive inhibitory input from AVLP710m (Figure S6G). The respective roles of these two DN subpopulations in turning and charging will be interesting topics for future investigation.

How DNs are organized to convey motor instructions from the brain to the VNC remains a topic of debate[52,55]. While some DNs function as command-like neurons[42,47,56–66], others may operate through population coding[67–70]. Recent studies suggest organizational principles by which actions are driven by networks of DNs organized under superordinate command-like DNs or through nested DN activities[53,54]. Our findings identify dual strategies by which AIP neurons may control threat motor actions: by promoting "synergistic" interactions between two wing DNs, or by driving the antagonistic influences of a pair of INs that in turn control multiple DNs. DNs have been considered as an information bottleneck between the brain and the VNC because they are greatly outnumbered by other types of neurons in both locations. This combinatorial coding strategy thus could enable greater complexity and adaptive action control given a limited number of DNs.

Generation of turn- and charge-like locomotion patterns

AIP elicits transient, discrete bouts of turning and charging, even under constant LED stimulation (Figure 7A). In contrast, high-frequency coactivation of AVLP491 and AVLP710m results in immobility; only low-frequency coactivation produces patterned turn- and charge-like locomotor bouts interspersed with periods of immobility ("stuttering") that resemble the behavioral effect of AIP activation (Figure 7Aiii-iv and 7D-E). This observation raises a new question: how is continuous AIP activation transformed into discrete, brief turning or charging bouts through AVLP491 and AVLP710m? One possibility is that the

synaptic properties between AIP and these two IN targets may define a transfer function that intrinsically limits their firing patterns. Specifically, AIP may activate AVLP710m with a temporal delay relative to AVLP491, so that AVLP491-elicited extended locomotion is truncated into brief bouts of discrete locomotion. In contrast to the effect of AIP activation, we observed a phase shift in the timing of locomotion relative to LED pulses in AVLP491/AVLP710m coactivation flies, suggesting that rebound excitation in downstream locomotor control circuits may also be involved. Alternatively, other cellular or circuit mechanisms may generate intermittent pulsatile output from AIP neurons despite continuous photostimulation. For example, AIP neurons make reciprocal excitatory connections with the IN AVLP016, which in turn makes reciprocal, asymmetric connections with AVLP710m (Figure S1C); such connectivity could yield intermittent activation of the latter IN which is out-of-phase with the activation of AVLP491. Other models involving network-level dynamics that cannot be inferred from static synaptic connectivity maps are also possible. While future investigation is required to test these possibilities, our findings suggest that the relative dynamics of AVLP491 and AVLP710m activation by AIP may be critical for generating turns and charges.

Flexible coupling and decoupling of actions under a hierarchical circuit.

Threat actions can be flexibly performed both independently and coordinately. While wing elevation can occur with or without turns and charges, pumping is typically accompanied by these locomotor actions[16]. Our data reveal how a threat display which coordinates both sets of appendages is achieved via parallel AIP recruitment of wing and leg

modules. However, this organization raises a key question: how does this circuit enable both coupling and decoupling of threat actions?

One possibility is that different levels of AIP activity may govern action selection. Our initial characterization of AIP neurons indicated that optogenetic activation of these cells can elicit different threat actions in a scalable manner, with turning and charging evoked by weaker stimulation than that required to promote wing elevation, while pumps require the strongest stimulation[16]. The stereotyped co-occurrence of pumping with turn and charge could be explained by this threshold model: when AIP activity reaches the level required to trigger pumping, it has already reached the activation thresholds for turning and charging, ensuring their simultaneous execution.

However, this mechanism alone cannot explain how wing elevation can occur without turning and charging[16], since the latter have a lower activation threshold than the former. In the absence of additional control mechanisms, a simple ramp-to-threshold model would predict that all instances of wing elevation should be accompanied by turning and charging, and this is not observed. Several potential mechanisms could explain this uncoupling. First, once AIP activity reaches the threshold for eliciting wing elevation, higher levels may recruit an inhibitory circuit node that suppresses leg movements. This inhibitory node could be the GABAergic IN AVLP710m; a node downstream of DNpe050/DNp60, in the VNC; or another, as-yet uncharacterized downstream target. Second, proprioceptive feedback from wing elevation may actively suppress locomotor actions under certain conditions. Third, locomotion during social behaviors may be modulated by external sensory cues[71–74,41]. Turn or charge could be suppressed when the fly is already facing its opponent

or in close proximity, preventing unnecessary and energetically costly rapid movements. Further studies will be required to distinguish these alternatives.

Neural circuit mechanisms for appendage coordination

We have identified a hierarchical circuit in which parallel direct and indirect projections to DNs coordinate appendage movements. This parallel, feedforward direct-indirect architecture superficially resembles the organization of the direct and indirect pathways of the basal ganglia[75], but with important distinctions: the basal ganglia's direct and indirect pathways have opposing effects on action selection, decision making, and learning[75], whereas here the two pathways drive distinct appendage movements that are coordinated into a single, cohesive behavior. Furthermore, the basal ganglia pathways are comprised of primarily of inhibitory projections, whereas here with the exception of AVLP710m the projections in the two pathways are excitatory.

Coordination across multiple appendages is a recurring requirement in many behaviors. In Drosophila courtship[45], for example, the male's choice of song type is modulated by male-female distance[71–73], which is itself determined by the male's locomotion relative to the female. Although the well-characterized courtship center, P1 neurons, can directly promote courtship song[14,15,56,76,77], their activation does not itself drive locomotion in a solitary male[15]; instead, P1 activity increases the gain of a visuomotor pathway that mediates tracking of small moving objects[78]. This suggest that courtship song and courtship-related locomotion (e.g., chasing) are governed by parallel pathways with crosstalk between them, rather than by a cohesive hierarchical circuit with shared upstream control such as we identify here for wing threat.

Escape behavior in insects likewise involves coupling between jumping and flight initiation, achieved by giant fiber DNs that directly excite leg extensor motor neurons and wing depressor interneurons[79]. This arrangement produces fast, stereotyped, and largely inflexible co-activation of the two appendages. By contrast, our data our data reveal a more complex and flexible circuit that allows both separate and coordinated activation of wing and leg movements during a social display.

Limitations of this study

Despite the insights provided by this study, several limitations should be acknowledged. First, although we were able to functionally elicit or inhibit threat actions through neuronal activity perturbation, we could not directly record the activity of AIP neurons or their downstream targets during natural wing threat displays. Achieving this would require an imaging setup in which wing threat actions can be evoked from flies by naturalistic visual stimuli in a head-fixed open-cuticle preparation under 2-photon optics — a technically challenging preparation that we were unable to establish despite extensive efforts. Additionally, conditions under which AVLP710m can be activated by AIP stimulation (as predicted by the connectome) need to be further explored. Second, naturalistic threat behavior may involve parallel circuits in addition to those studied here, which act in a partially redundant manner. Nevertheless, silencing of AIP neurons virtually abolished naturalistic threat[16]. Third, in this study we analyzed the function of four different neuron types that are direct synaptic targets of AIP neurons, but the roles of other direct DN and IN targets, or of indirect DN targets of AIP remain uncharacterized. The fact that we did not observe detectable phenotypes when silencing AVLP491 or AVLP710m during natural

threat display suggests that additional neurons in this circuit, or even outside the AIP circuit, may be involved in wing threat. A comprehensive understanding of the subtleties of wing threat control will necessitate genetic access to, and functional analysis of, these additional cell types, alone and in combination with those characterized here. Finally, we have not addressed how sensory cues from the opponent fly may regulate threat action selection, and the role of upstream inputs to AIP in mediating the influence of such cues. Future studies should address these important unanswered questions.

Main Figures

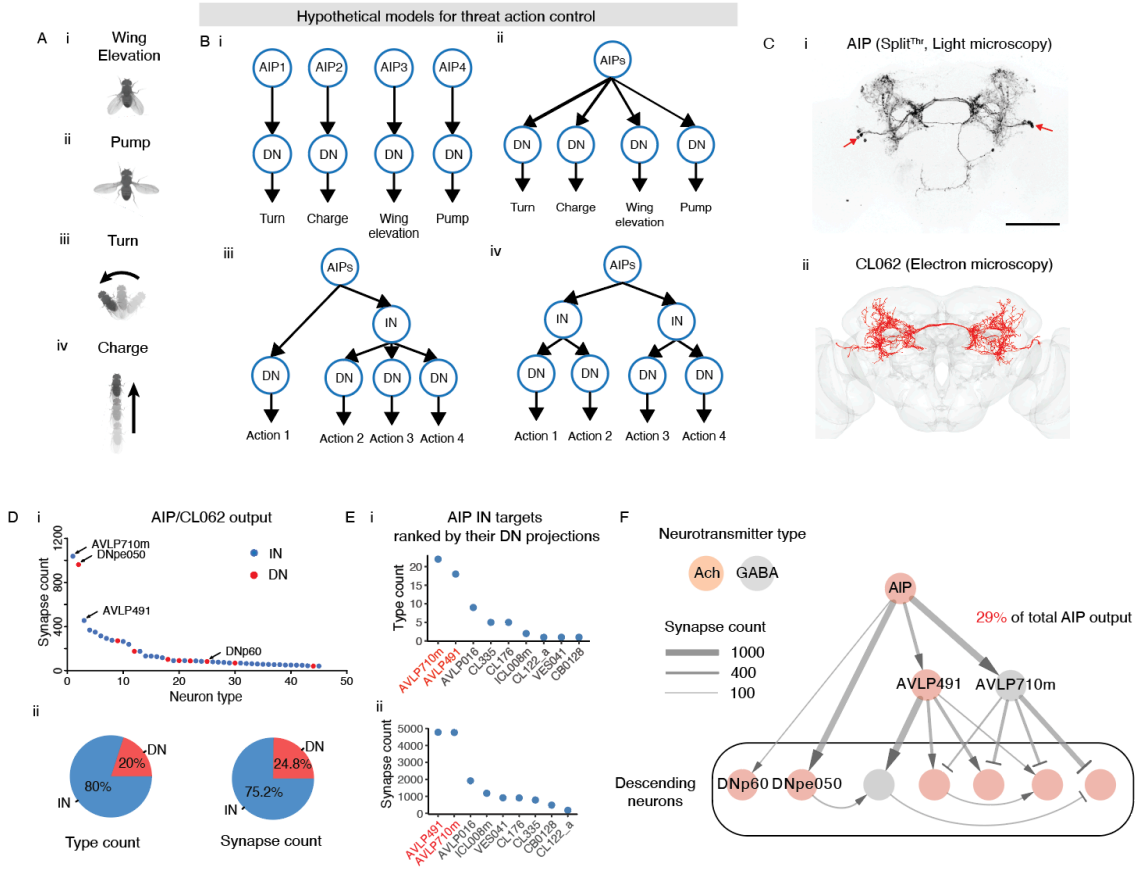

Figure 1. AIP downstream circuit and models of how threat actions are controlled

(A) Four distinct actions of threat display: wing elevation (i), pump (ii), turn (iii), and charge (iv).

(B) Models of how AIP neurons control four distinct threat actions. In (ii), thickness of arrows indicates the strength of connections.

(C) Expression pattern of $Split^{Thr}$ (i), and cell skeletons of AIP neurons reconstructed in the male CNS connectome (ii). Scale bar, 100μm. Arrows indicate the cell body locations of AIP.

(D) (i) Synapse count between AIP and downstream targets. (ii) The percentage of DN and IN among downstream targets counted by types or total synapses. Threshold: 40 synapses.

(E) (i) Total number of DN types that receive direct input from AIP downstream targets. (ii) Total output synapses AIP downstream targets form with DNs. Threshold: 50 synapses.

(F) A circuit diagram of AIP and major downstream descending neuron (DN) and interneuron (IN) targets.

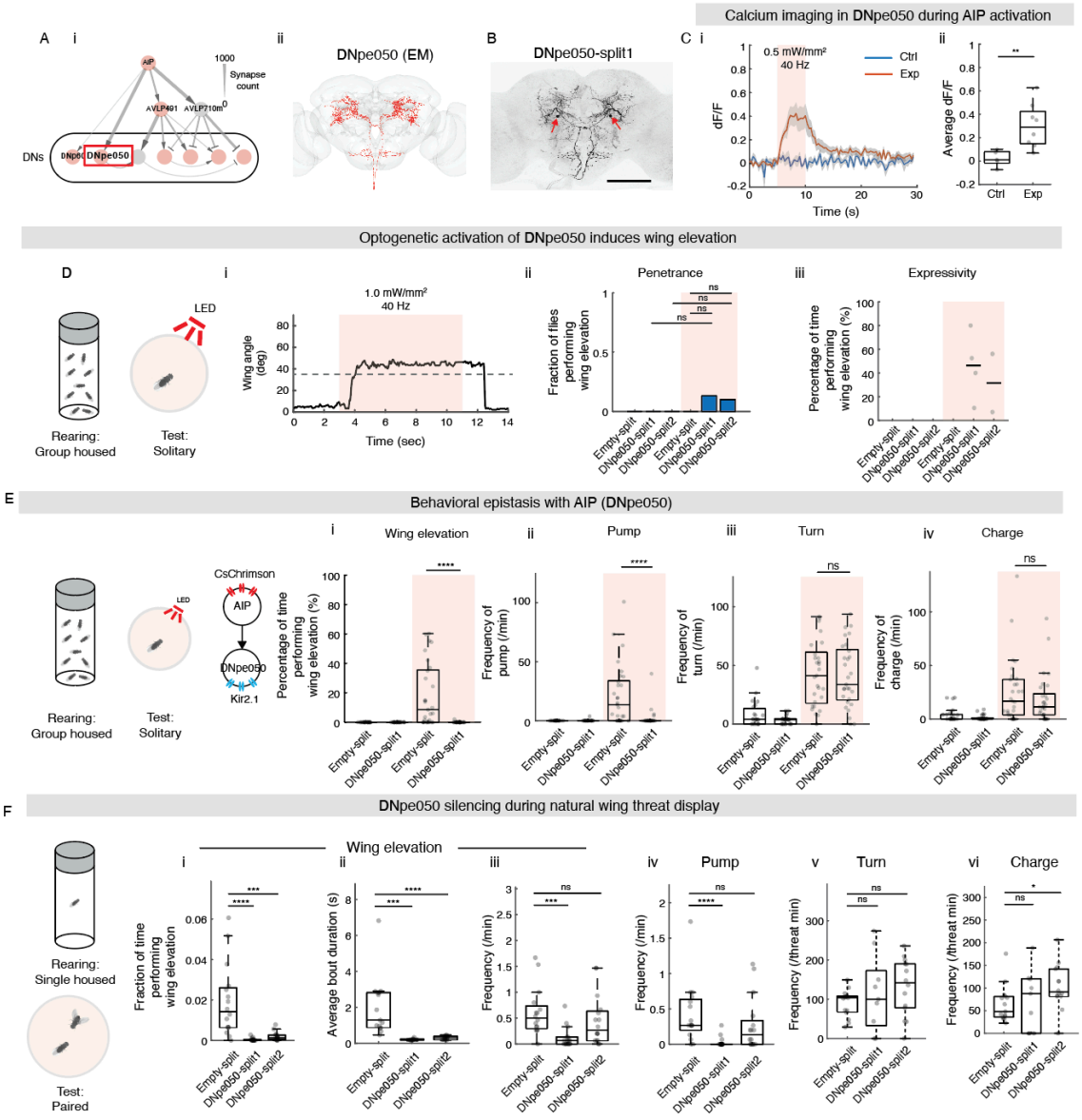
Calcium imaging in DNpe050 during AIP activation
A i
AIP
1000
Synapse count
0
AVLP491
AVLP710m
DNs
DNp06
DNpe050
ii
DNpe050 (EM)
B
DNpe050-split1
C i
0.5 mW/mm²
40 Hz
Ctrl
Exp
dF/F
Time (s)
ii
Average dF/F
Ctrl
Exp
Optogenetic activation of DNpe050 induces wing elevation
D
LED
Rearing:
Group housed
Test:
Solitary
i
1.0 mW/mm²
40 Hz
Wing angle (deg)
Time (sec)
ii
Penetrance
Fraction of flies performing wing elevation
ns
Empty-split
DNpe050-split1
DNpe050-split2
iii
Expressivity
Percentage of time performing wing elevation (%)
E
Behavioral epistasis with AIP (DNpe050)
CsChrimson
AIP
DNpe050
Kir2.1
LED
Rearing:
Group housed
Test:
Solitary
i
Wing elevation
Percentage of time performing wing elevation (%)
****
ii
Pump
Frequency of pump (/min)
iii
Turn
Frequency of turn (/min)
iv
Charge
Frequency of charge (/min)
F
DNpe050 silencing during natural wing threat display
Rearing:
Single housed
Test:
Paired
Wing elevation
i
Fraction of time performing wing elevation
ii
Average bout duration (s)
iii
Frequency (/min)
iv
Pump
Frequency (/min)
v
Turn
Frequency (/threat min)
vi
Charge
Frequency (/threat min)
Empty-split
DNpe050-split1
DNpe050-split2

Figure 2. DNpe050 activation increases the probability of wing elevation

(A) (i) DNpe050 highlighted in the AIP downstream circuit diagram (red box). (ii) Cell skeletons of DNpe050 reconstructed in the male CNS connectome.

(B) Expression pattern of DNpe050-split1 (with Otd-FLP). Arrows: cell body locations of DNpe050. Scale bar, 100μm.

(C) jGCaMP8m fluorescence changes in DNpe050 in response to AIP stimulation in head-fixed living flies. (i) DNpe050 response (dF/F) before, during, and after photostimulation of AIP. Red shaded region indicates light delivery. (ii) Average DNpe050 response (dF/F) during photostimulation. Exp: AIP > Chrimson; DNpe050-split2 > GCaMP8m. N = 8 cells. Ctrl: Empty > Chrimson; DNpe050-split2 > GCaMP8m. N = 5 cells.

(D) DNpe050 (with Otd-FLP) activation elicits wing elevation in a small fraction of individuals. (i) A representative wing angle trace showing stable wing elevation during optogenetic activation. Dashed line: threshold wing angle criterion for wing elevation. (ii) Fraction of flies exhibiting sustained wing elevation ("penetrance"). (iii) Percentage of stimulation time performing wing elevation ("expressivity"). White and red shaded regions indicate quantifications before and during stimulation period, respectively. Empty-split: N = 31. DNpe050-split1: N = 30. DNpe050-split2: N = 20.

(E) Silencing DNpe050 (with Otd-FLP) using Kir2.1 reduces AIP-evoked wing elevation (i) and pumps (ii) but not turns (iii) or charges (iv). Empty-split: N = 29. DNpe050-split1: N = 29.

(F) Behavioral quantification for silencing of DNpe050 (with Otd-FLP) using Kir2.1 during natural threat display: (i) fraction of time performing wing elevation, (ii) average wing

elevation bout duration, (iii) frequency of wing elevation, (iv) frequency of pumps, (v) frequency of turns during wing threat, (vi) frequency of charges during wing threat. Empty-split: N = 16 pairs. DNpe050-split1: N = 16 pairs. DNpe050-split2: N = 16 pairs.

Here and throughout, datapoints represent individual animals. Boxplots indicate median (box dividing line), interquartile range (box), and 1.5 times the interquartile range (whiskers). When less than 5 datapoints, lines denote median.

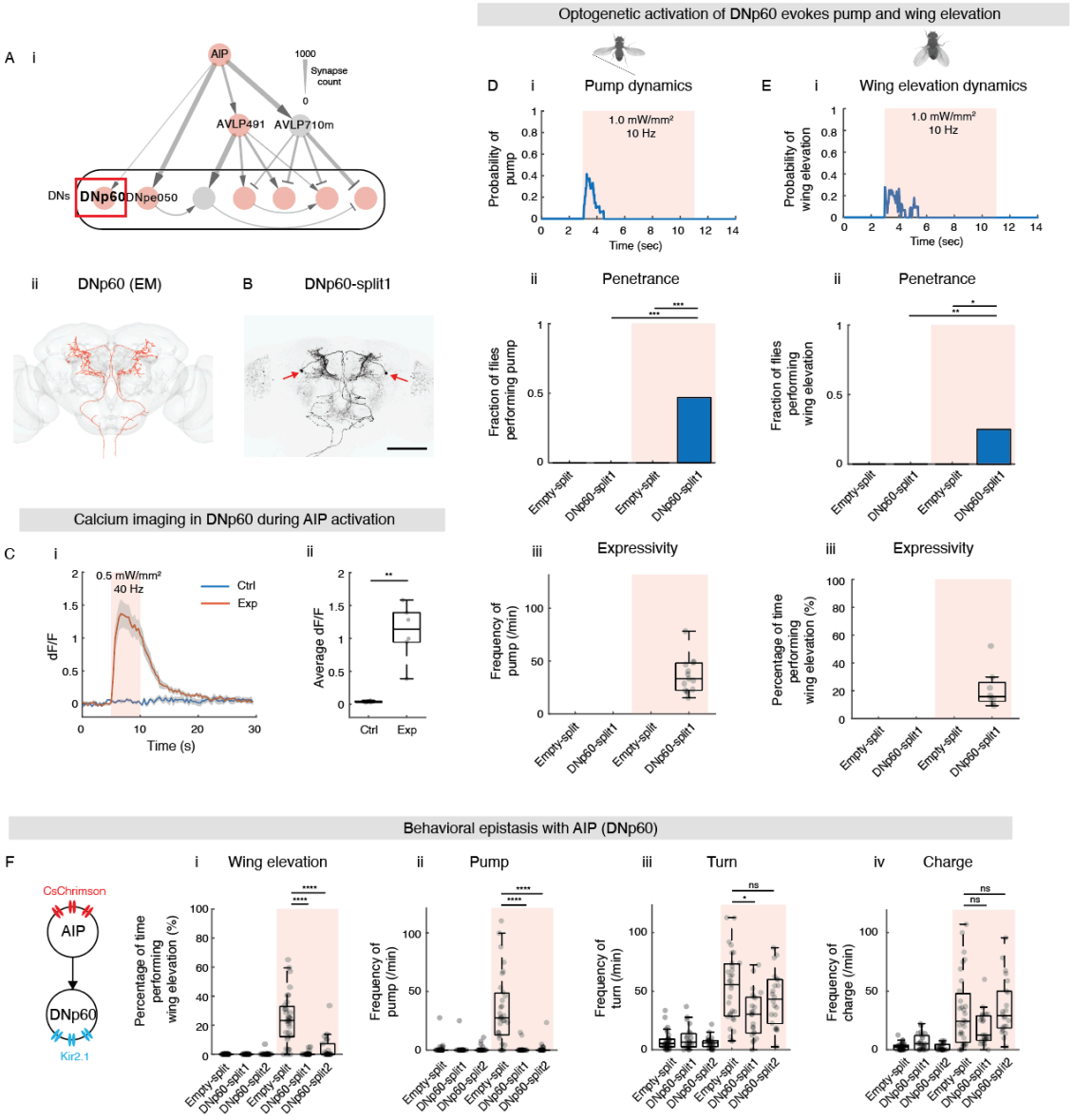
Optogenetic activation of DNp60 evokes pump and wing elevation
A i
AIP
1000
Synapse count
0
AVLP491
AVLP710m
DNs
DNp60
DNpe050
ii DNp60 (EM)
B DNp60-split1
Calcium imaging in DNp60 during AIP activation
C i
0.5 mW/mm²
40 Hz
Ctrl
Exp
dF/F
Time (s)
ii
Average dF/F
Ctrl
Exp
D i Pump dynamics
1.0 mW/mm²
10 Hz
Probability of pump
Time (sec)
ii Penetrance
Fraction of flies performing pump
iii Expressivity
Frequency of pump (/min)
E i Wing elevation dynamics
Probability of wing elevation
ii Penetrance
Fraction of flies performing wing elevation
iii Expressivity
Percentage of time performing wing elevation (%)
Empty-split
DNp60-split1
Behavioral epistasis with AIP (DNp60)
F
CsChrimson
AIP
DNp60
Kir2.1
i Wing elevation
ii Pump
iii Turn
iv Charge
Frequency of turn (/min)
Frequency of charge (/min)
DNp60-split2

Figure 3. DNp60 elicits pump and wing elevation

(A) (i) DNp60 highlighted in the AIP downstream circuit diagram (red box). (ii) Cell skeletons of DNp60 reconstructed in the male CNS connectome.

(B) Expression pattern of DNp60-split1 (with Otd-FLP). Arrows: cell body locations of DNp60. Scale bar, 100μm.

(C) jGCaMP8m fluorescence changes in DNp60 in response to AIP stimulation. (i) DNp60 response (dF/F) before, during, and after photostimulation of AIP. Red shaded region indicates light delivery. (ii) Average DNp60 response (dF/F) during photostimulation. Exp: AIP > Chrimson; DNp60-split1 > GCaMP8m. N = 6 cells. Ctrl: Empty > Chrimson; DNp60-split1 > GCaMP8m. N = 6 cells.

(D) DNp60 (with Otd-FLP) activation elicits pump. (i) Probability of pump during a photostimulation trial. (ii) Fraction of flies performing at least one pump and (iii) frequency of pump during photostimulation. Empty-split: N = 16. DNp60-split1: N = 32.

(E) DNp60 (with Otd-FLP) activation elicits wing elevation. Same as (D) but quantifications for wing elevation. Empty-split: N = 16. DNp60-split1: N = 32.

(F) Silencing of DNp60 (with Otd-FLP) using Kir2.1 reduces AIP-evoked wing elevation (i) and pumps (ii) but not turns (iii) or charges (iv). Empty-split: N = 31. DNp60-split1: N = 23. DNp60-split2: N = 22.

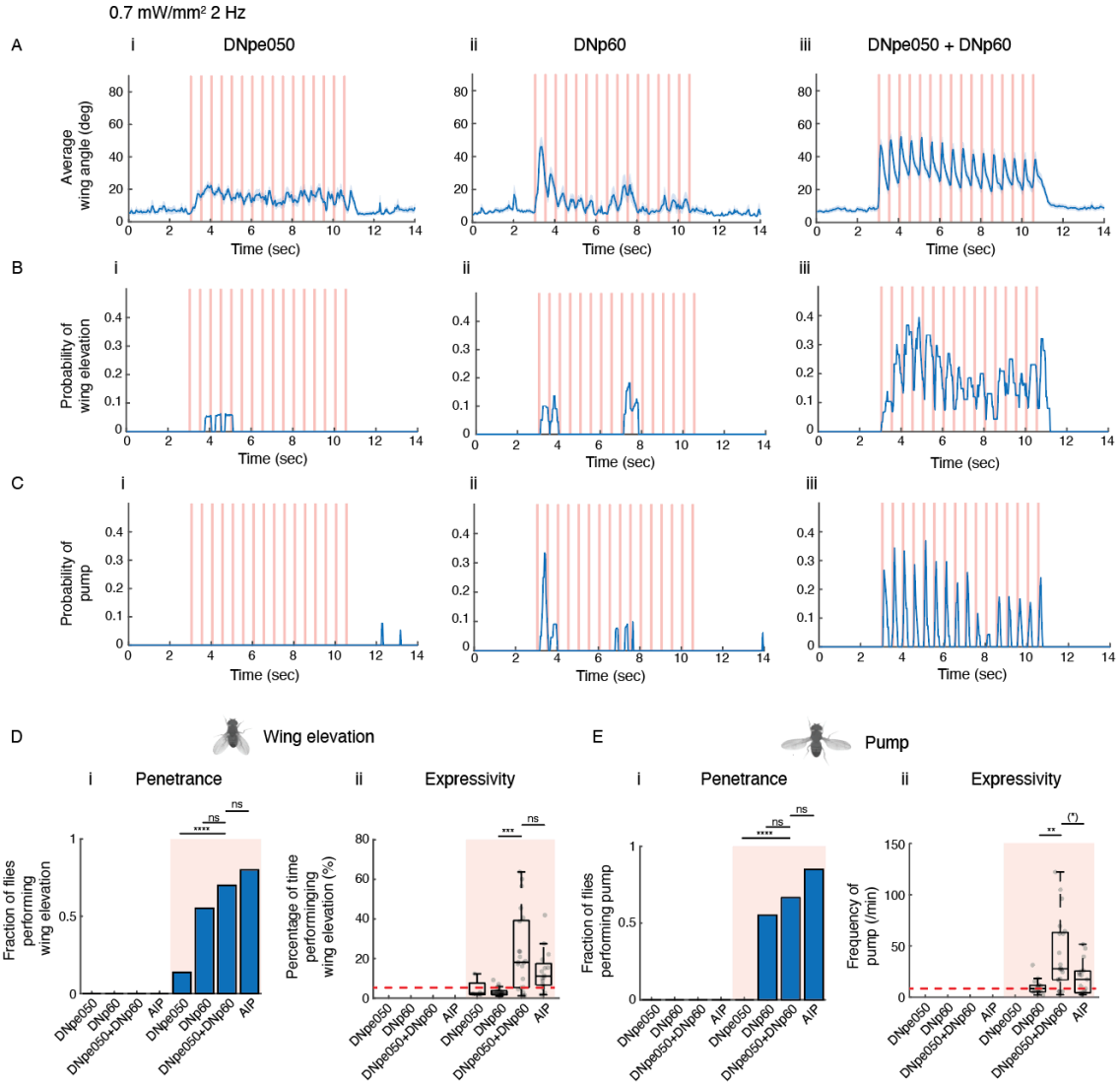
0.7 mW/mm² 2 Hz
A
i DNpe050
ii DNp60
iii DNpe050 + DNp60
Average wing angle (deg)
Time (sec)
B
Probability of wing elevation
C
Probability of pump
D
Wing elevation
E
Pump
Penetrance
Expressivity
Fraction of flies performing wing elevation
Percentage of time performinging wing elevation (%)
Fraction of flies performing pump
Frequency of pump (/min)
DNpe050
DNp60
DNpe050+DNp60
AIP
ns
****
***
**
(*)

Figure 4. DNpe050 and DNp60 synergistically control wing elevation and pump

(A) Wing angles before, during, and after photostimulation of (i) DNpe050-split2 (with Otd-FLP), (ii) DNp60-split1 (with Otd-FLP), and (iii) DNpe050-split1 and DNp60-split2 combined (with Otd-FLP, effectively labeling DNpe050-split2 neurons as well, see Table S1 for detailed genotypes). Here and throughout, shaded lines denote mean ± SEM.

(B) Probability of wing elevation during photostimulation of (i) DNpe050 (with Otd-FLP), (ii) DNp60 (with Otd-FLP), and (iii) DNpe050 and DNp60 combined (with Otd-FLP).

(C) Probability of pump during photostimulation of (i) DNpe050 (with Otd-FLP), (ii) DNp60 (with Otd-FLP), and (iii) DNpe050 and DNp60 combined (with Otd-FLP).

(D) Fraction of flies performing at least one wing elevation bout (i) and percentage of time performing wing elevation (ii) during photostimulation. Red dashed line indicates the linear summation of medians of DNpe050 and DNp60 activation alone. DNpe050: N = 29. DNp60: N = 29. DNpe050+DNp60: N = 30. AIP: N = 20.

(E) Fraction of flies performing at least one pump (i) and frequency of pump (ii) during photostimulation. Red dashed line indicates the linear summation of medians of DNpe050 and DNp60 activation alone. DNpe050: N = 29. DNp60: N = 29. DNpe050+DNp60: N = 30. AIP: N = 20.

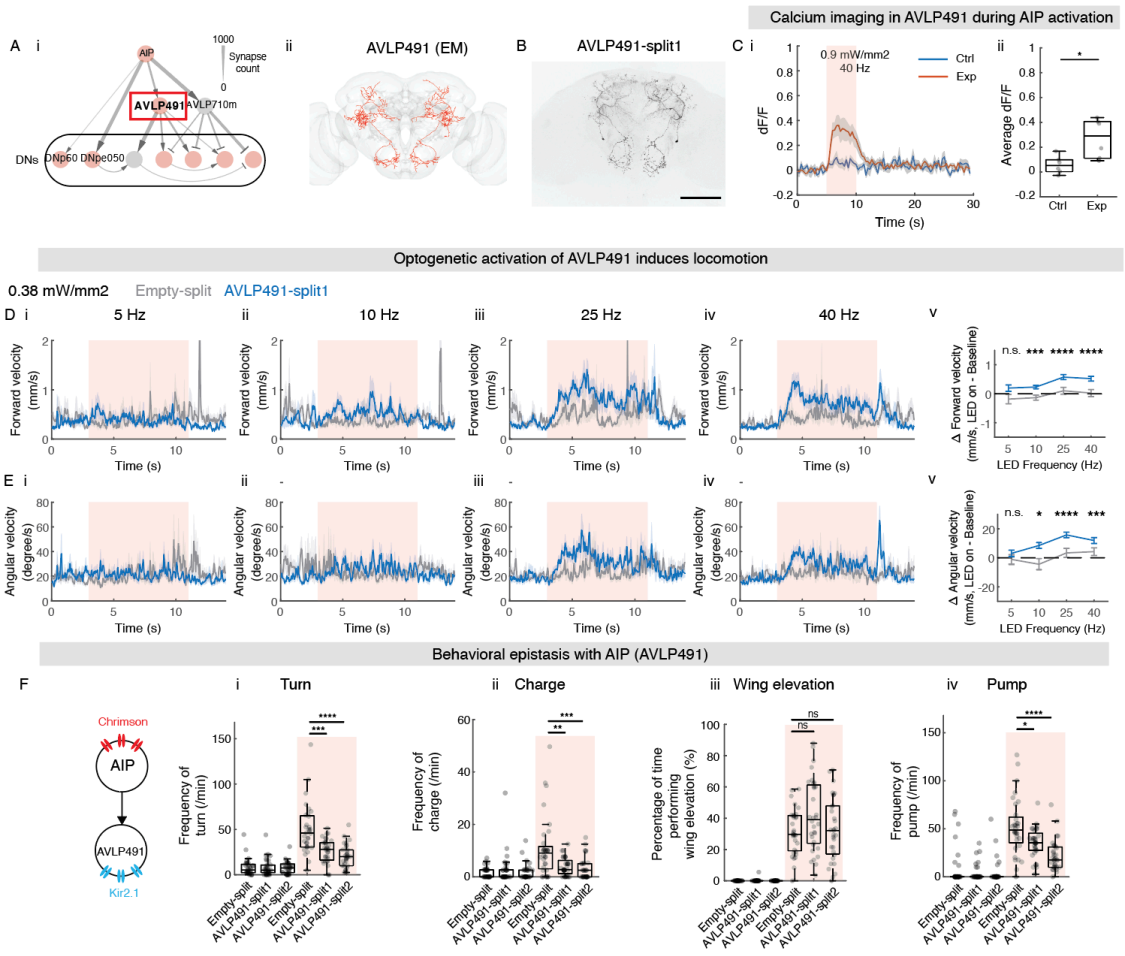
Calcium imaging in AVLP491 during AIP activation
A i
AIP
1000
Synapse count
0
AVLP491
AVLP710m
DNs
DNp60 DNpe050
ii
AVLP491 (EM)
B
AVLP491-split1
C i
0.9 mW/mm2
40 Hz
Ctrl
Exp
dF/F
Time (s)
ii
Average dF/F
Ctrl
Exp
Optogenetic activation of AVLP491 induces locomotion
0.38 mW/mm2
Empty-split
AVLP491-split1
D i 5 Hz
ii 10 Hz
iii 25 Hz
iv 40 Hz
v
Forward velocity (mm/s)
Time (s)
Δ Forward velocity (mm/s, LED on - Baseline)
n.s.
LED Frequency (Hz)
E i
ii
iii
iv
v
Angular velocity (degree/s)
Δ Angular velocity (mm/s, LED on - Baseline)
Behavioral epistasis with AIP (AVLP491)
F
Chrimson
AIP
AVLP491
Kir2.1
i Turn
ii Charge
iii Wing elevation
iv Pump
Frequency of turn (/min)
Frequency of charge (/min)
Percentage of time performing wing elevation (%)
Frequency of pump (/min)
Empty-split
AVLP491-split1
AVLP491-split2

Figure 5. AVLP491 induces locomotion and is necessary for AIP-elicited threat locomotor actions

(A) (i) AVLP491 highlighted in the AIP downstream circuit diagram (red box). (ii) Cell skeletons of AVLP491 reconstructed in the male CNS connectome.

(B) Expression pattern of AVLP491-split1 (with Otd-FLP). Scale bar, 100μm.

(C) jGCaMP8m fluorescence changes in AVLP491 in response to AIP stimulation. (i) AVLP491 response (dF/F) before, during, and after photostimulation of AIP. Red shaded region indicates light delivery. (ii) Average AVLP491 response (dF/F) during photostimulation. Exp: AIP > Chrimson; AVLP491-split1 > GCaMP8m. N = 6 cells. Ctrl: Empty > Chrimson; AVLP491-split1 > GCaMP8m. N = 6 cells.

(D) Forward velocities before, during, and after optogenetic activation of AVLP491-split1 (with Otd-FLP) at 5 Hz (i), 10 Hz (ii), 25 Hz (iii) and 40 Hz (iv) in dusted flies. (v) Differences in average forward velocities during photostimulation compared to baseline. Statistical comparisons are performed between the control and experimental groups. Lines and error bars denote mean ± SEM. Empty-split: N = 52 (5 Hz), 54 (10 Hz), 53 (25 Hz), 53 (40 Hz). AVLP491-split1: N = 44 (5 Hz), 43 (10 Hz), 44 (25 Hz), 44 (40 Hz). See Table S2 for details of statistics.

(E) same as (D) but for angular velocities. In (D) and (E), experiments were performed in dusted flies with dim green background lighting to minimize the spontaneous and light-induced startle locomotion (See Methods).

(F) Silencing of AVLP491 reduces AIP-elicited turns (i), charges (ii), and pumps (iv) but not wing elevation (iii). Empty-split: N = 32. AVLP491-split1: N = 32. AVLP491-split2: N = 31.

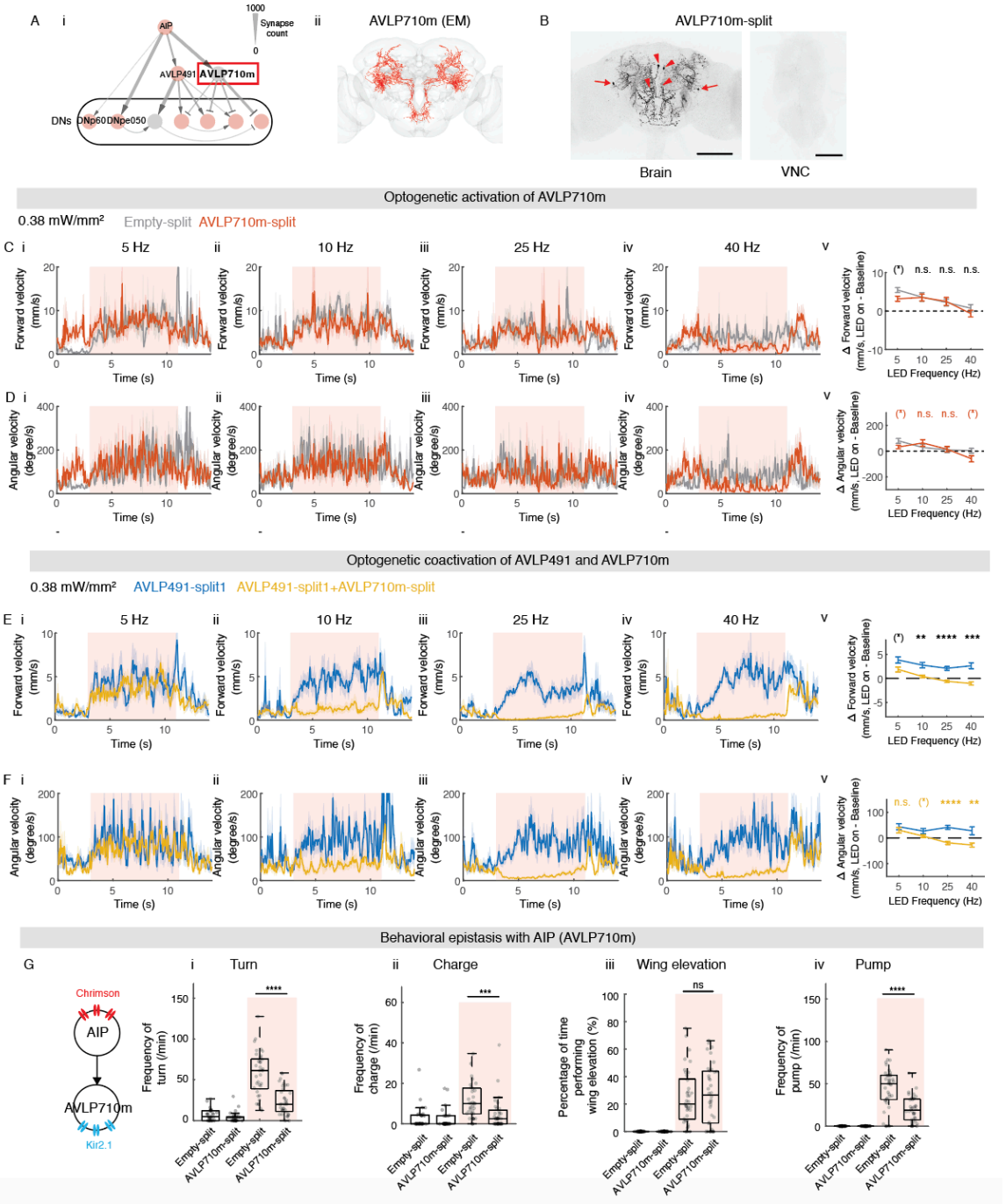
A i
AIP
1000
Synapse count
0
AVLP491
AVLP710m
DNs
DNp60
DNpe050
ii
AVLP710m (EM)
B
AVLP710m-split
Brain
VNC
Optogenetic activation of AVLP710m
0.38 mW/mm²
Empty-split
AVLP710m-split
C i
5 Hz
ii
10 Hz
iii
25 Hz
iv
40 Hz
v
Forward velocity (mm/s)
Time (s)
Δ Forward velocity (mm/s, LED on - Baseline)
LED Frequency (Hz)
(*) n.s. n.s. n.s.
D i
Angular velocity (degree/s)
Δ Angular velocity (mm/s, LED on - Baseline)
(*) n.s. n.s. (*)
Optogenetic coactivation of AVLP491 and AVLP710m
0.38 mW/mm²
AVLP491-split1
AVLP491-split1+AVLP710m-split
E i
(*) ** **** ***
F i
n.s. (*) **** **
Behavioral epistasis with AIP (AVLP710m)
G
Chrimson
AIP
AVLP710m
Kir2.1
i Turn
Frequency of turn (/min)
****
ii Charge
Frequency of charge (/min)
***
iii Wing elevation
Percentage of time performing wing elevation (%)
ns
iv Pump
Frequency of pump (/min)
Empty-split
AVLP710m-split

Figure 6. AVLP710m functions antagonistically to AVLP491 to control locomotion

(A) (i) AVLP710m highlighted in the AIP downstream circuit diagram (red box). (ii) Cell skeletons of AVLP710m reconstructed in the male CNS connectome.

(B) Expression pattern of AVLP710m-split (with Otd-FLP). Arrows: cell body locations of AVLP710m. Arrowheads: cell body locations of off-target neurons. Scale bar, 100μm.

(C) Forward velocities before, during, and after optogenetic activation of AVLP710m (with Otd-FLP) at 5 Hz (i), 10 Hz (ii), 25 Hz (iii) and 40 Hz (iv) in dusted flies. (v) Differences in average forward velocities during photostimulation compared to baseline. Statistical comparisons are performed between the control and experimental groups. Lines and error bars denote mean ± SEM. Empty-split: N = 24 (5 Hz), 23 (10 Hz), 21 (25 Hz), 25 (40 Hz). AVLP710m-split: N = 29 (5 Hz), 29 (10 Hz), 25 (25 Hz), 22 (40 Hz).

(D) same as (C) but for angular velocities.

(E) Forward velocities before, during, and after optogenetic activation of AVLP491 (with Otd-FLP) alone or AVLP491 and AVLP710m combined (with Otd-FLP) at 5 Hz (i), 10 Hz (ii), 25 Hz (iii) and 40 Hz (iv). (v) Differences in average forward velocities during photostimulation compared to baseline. Statistical comparisons are performed between the control and experimental groups. Lines and error bars denote mean ± SEM. AVLP491-split1: N = 15 (5 Hz), 15 (10 Hz), 13 (25 Hz), 13 (40 Hz). AVLP491-split1+AVLP710m-split: N = 29 (5 Hz), 27 (10 Hz), 28 (25 Hz), 28 (40 Hz).

(F) same as (E) but for angular velocities.

(G) Silencing of AVLP710m reduces AIP-elicited turns (i), charges (ii), and pumps (iv) but not wing elevation (iii). Empty-split: N = 37. AVLP710m-split: N = 36.

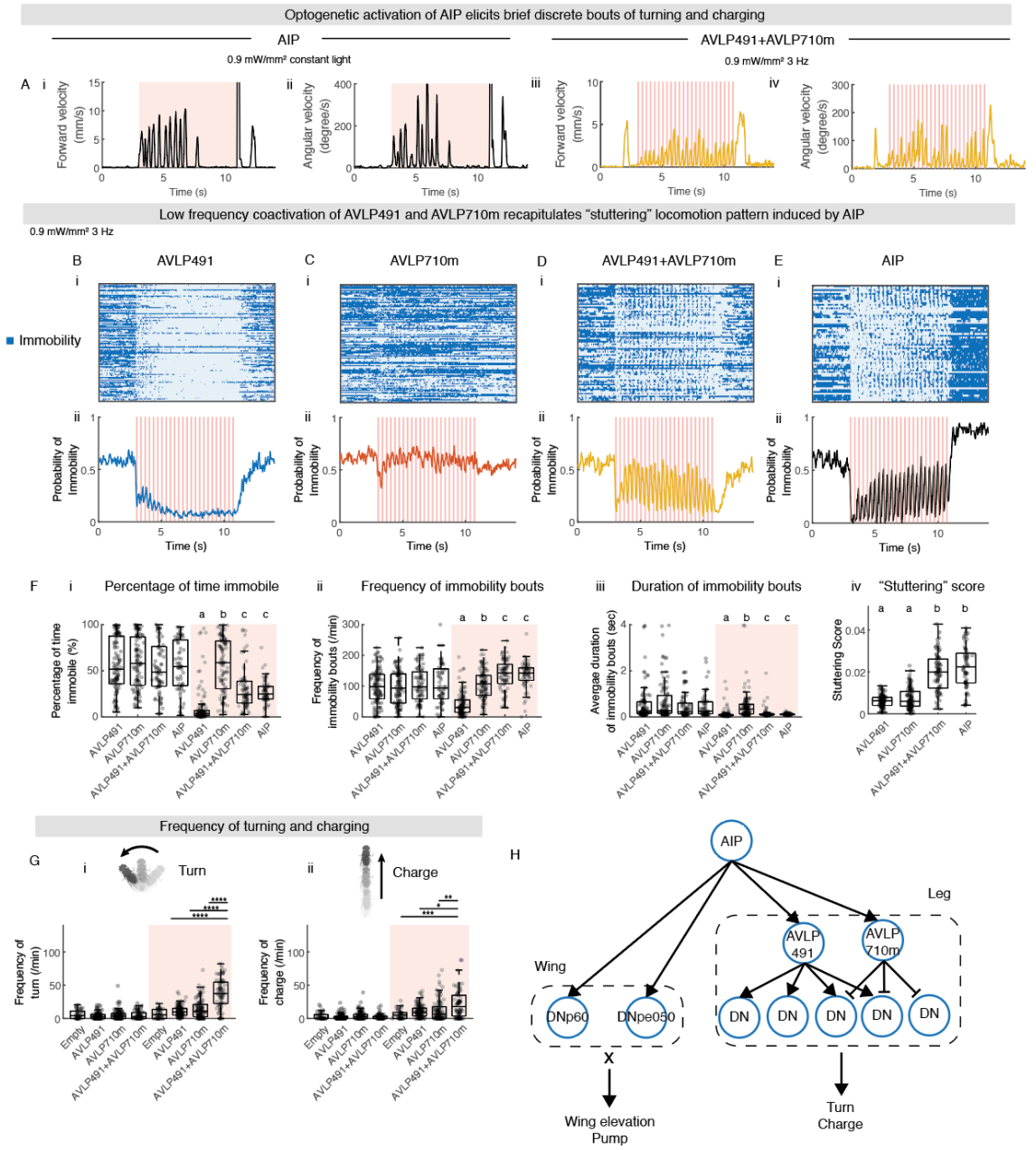
Optogenetic activation of AIP elicits brief discrete bouts of turning and charging
AIP
0.9 mW/mm² constant light
AVLP491+AVLP710m
0.9 mW/mm² 3 Hz
A i
ii
iii
iv
Forward velocity (mm/s)
Angular velocity (degree/s)
Time (s)
Low frequency coactivation of AVLP491 and AVLP710m recapitulates "stuttering" locomotion pattern induced by AIP
0.9 mW/mm² 3 Hz
B AVLP491
C AVLP710m
D AVLP491+AVLP710m
E AIP
Immobility
Probability of Immobility
F i Percentage of time immobile
ii Frequency of immobility bouts
iii Duration of immobility bouts
iv "Stuttering" score
Percentage of time immobile (%)
Frequency of immobility bouts (/min)
Avergae duration of immobility bouts (sec)
Stuttering Score
AVLP491
AVLP710m
AVLP491+AVLP710m
AIP
Frequency of turning and charging
G i Turn
ii Charge
Frequency of turn (/min)
Frequency of charge (/min)
Empty
H
AIP
Leg
Wing
AVLP 491
AVLP 710m
DNp60
DNpe050
DN
X
Wing elevation
Pump
Turn
Charge

Figure 7. Temporally patterned AVLP491 and AVLP710m coactivation recapitulates AIP-induced turn and charge-like behavior

(A) Forward (i) and angular (ii) velocity traces of an example fly during AIP (with Otd-FLP) photostimulation with constant LED light. Forward (iii) and angular (iv) velocity traces of an example fly during AVLP491 and AVLP710m co-activation (with Otd-FLP) with 3 Hz LED light.

(B) (i) Raster plot showing the immobility bouts of individual flies, and probability of immobility across the population (ii) before, during, and after photo-stimulation of AVLP491 (with Otd-FLP).

(C-E) same as (B) but for activation of AVLP710m (with Otd-FLP) (C), AVLP491+AVLP710m (with Otd-FLP) (D), and AIP (with Otd-FLP) (E).

(F) Percentage of time (i), frequency (ii), and average bout duration (iii) of immobility before and during photo-stimulation. (iv) "Stuttering" score for quantifying the periodicity of immobility during photo-stimulation. AVLP491: N = 113 (i), 113 (ii), 104 (iii), 104 (iv). AVLP710m: N = 105 (i), 105 (ii), 105 (iii), 105 (iv). AVLP491+AVLP710m: N = 75 (i), 75 (ii), 75 (iii), 75 (iv). AIP: N = 61 (i), 61 (ii), 60 (iii), 60 (iv).

(G) Quantification of turning (i) and charging-like behavior (ii) during photostimulation (with Otd-FLP). Empty: N = 38. AVLP491: N = 107. AVLP710m: N = 100. AVLP491+AVLP710m: N = 68.

(H) A working model of AIP downstream circuit.

Supplemental Figures

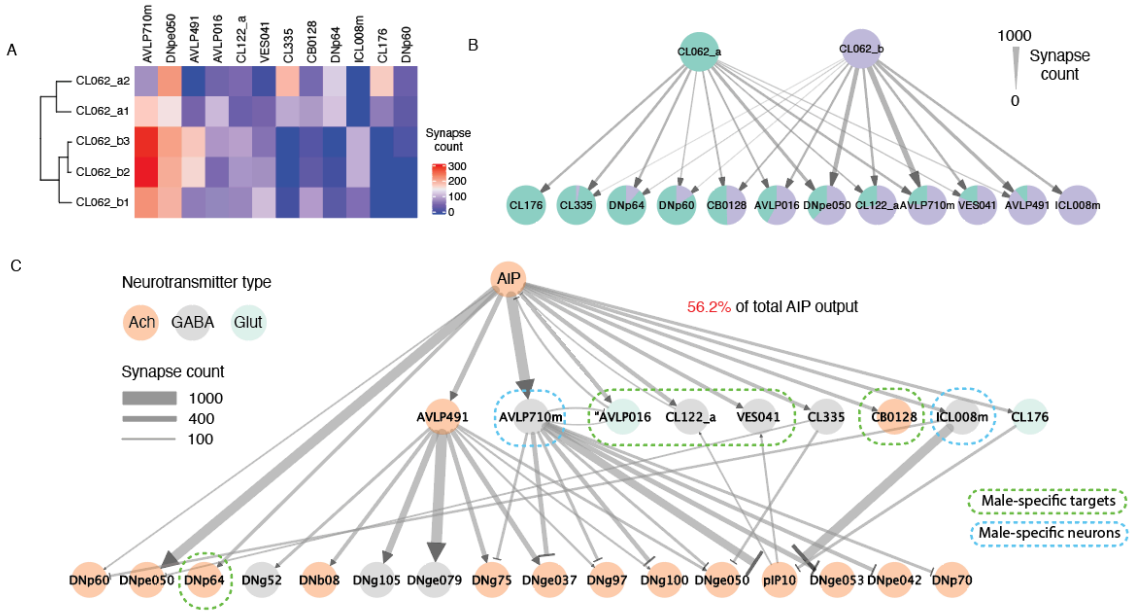

D

	p65.AD	Gal4.DBD
DNpe050 first round	12G09	12G04
	57C10	12G04
	VT016287	12G04
	VT058429	12G04
	50A11	12G09
	VT016281	12G09
	VT058429	12G09
	12G09	VT058429
DNpe050 EB drivers	VT058429	12G09EB1
	VT058429	12G09EB3
	VT058429	12G09EB4
	VT058429EB1	12G09
	VT058429EB2	12G09
	VT058429EB5	12G09
	VT058429EB3	12G09
	VT058429EB4	12G09
	VT058429	12G09EB2
	VT058429	12G09EB5
	VT058429EB1	12G09EB3
DNpe050 second round	VT016281	12G09EB3
	VT058429EB1	60F01
	VT058429EB1	VT016281
	VT058429EB1	VT056582
	VT058429EB1	VT061518
	VT008977	12G09EB3
	VT058429EB1	VT008977
	VT058429EB1	VT007722
	VT058429EB1	VT010265
	VT058429EB1	VT044166
	VT058429EB1	VT045669

	p65.AD	Gal4.DBD
DNp60	54A01	41E03
	54A01	VT045669
	54E12	41E03
	VT009671	41E03
	VT040574	41E03
	VT045670	41E03

AVLP491	57C10	VT025952
	65B04	VT025952
	VT043707	VT025952
	VT043707	65B04
	65B04	VT008974
	65B04	VT046778
	VT008974	VT025952
	65B04	VT019059
	65B04	VT063567
	46A02	VT025952
	VT063567	VT025952
	VT008974	VT046778

	p65.AD	Gal4.DBD
AVLP710m	26E08	VT032899
	85F12	26E08
	85F12	VT032899
	VT032899	26E08
	81D09	VT032899
	85F12	25E05
	VT032899	25E05
	85F12	47G10
	VT032899	47G10
	25E05	85F12
	25E05	VT032899
	81D09	25E05
	VT032899	85F12
	25E05	47G10
	81D09	47G10
	81D09	85F12

split-Gal4 combinations used in this study

Figure S1. Heterogeneity in AIP population and other AIP downstream targets

(A) A heat map of synapse counts between individual pairs of AIP (CL062) neurons and major downstream targets. Dendrogram shows the hierarchical clustering of AIP pairs based on downstream connectivity.

(B) A circuit diagram of the connectivity between the two AIP (CL062) subtypes and their major downstream targets. Pie charts represent the ratio of input synapses that each downstream target receives from the two AIP subtypes respectively. Only projections from AIP to downstream targets are displayed.

(C) A detailed circuit diagram including AIP/CL062, major direct AIP downstream targets, and DN targets of AVLP491 and AVLP710m.

(D) A summary table of split-GAL4 drivers screened in this study. Green shades highlight the combinations that were selected for this study based on their specificity and expression strength.

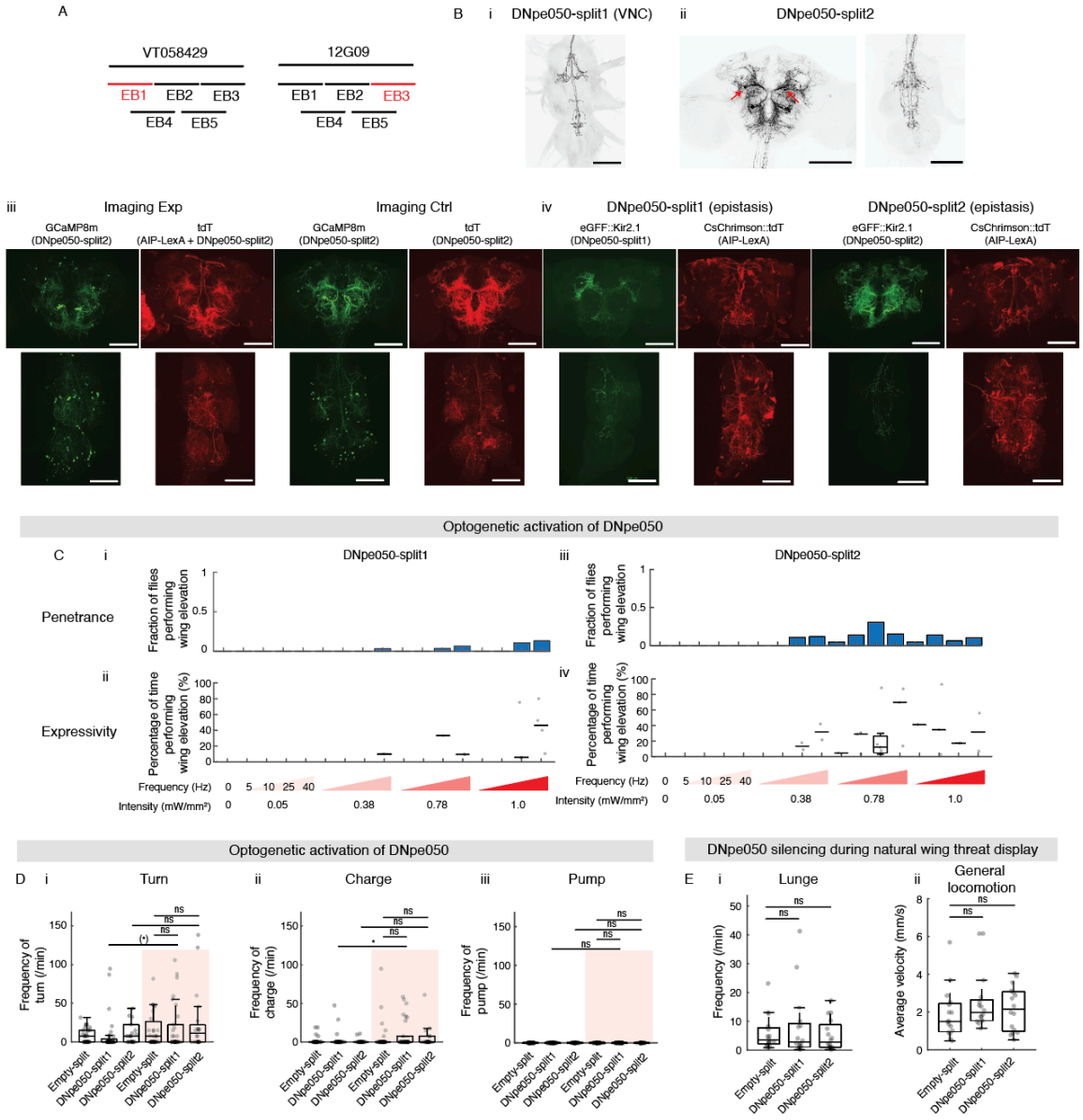
A
VT058429
EB1 EB2 EB3
EB4 EB5
12G09
EB1 EB2 EB3
EB4 EB5
B i DNpe050-split1 (VNC)
ii DNpe050-split2
iii Imaging Exp
GCaMP8m (DNpe050-split2)
tdT (AIP-LexA + DNpe050-split2)
Imaging Ctrl
GCaMP8m (DNpe050-split2)
tdT (DNpe050-split2)
iv DNpe050-split1 (epistasis)
eGFF::Kir2.1 (DNpe050-split1)
CsChrimson::tdT (AIP-LexA)
DNpe050-split2 (epistasis)
eGFF::Kir2.1 (DNpe050-split2)
CsChrimson::tdT (AIP-LexA)
Optogenetic activation of DNpe050
C i DNpe050-split1
iii DNpe050-split2
Penetrance
Fraction of flies performing wing elevation
ii
iv
Expressivity
Percentage of time performing wing elevation (%)
Frequency (Hz) 0 5 10 25 40
Intensity (mW/mm²) 0 0.05 0.38 0.78 1.0
Optogenetic activation of DNpe050
DNpe050 silencing during natural wing threat display
D i Turn
ii Charge
iii Pump
Frequency of turn (/min)
Frequency of charge (/min)
Frequency of pump (/min)
ns
(*)
Empty-split
DNpe050-split1
DNpe050-split2
E i Lunge
ii General locomotion
Frequency (/min)
Average velocity (mm/s)

Figure S2. DNpe050 activation does not promote turning, charging, or pumping

(A) A scheme illustrating the enhancer-bashing strategy for identification of sparse and specific DNpe050 drivers. Fragments that retain labeling in DNpe050 are highlighted in red.

(B) Expression pattern of DNpe050-split1 (VNC, with Otd-FLP) (i) and DNpe050-split2 (with Otd-FLP) (ii). (iii) Expression pattern of GCaMP8m and tdT in experimental (Exp) and control (Ctrl) groups of DNpe050 functional imaging. Note that in experimental group, tdT signal comes from both AIP-LexA>Chrimson::tdT and DNpe050-split2>tdT. The control group does not contain the AIP-LexA transgene. (iv) Expression pattern of Kir2.1 and CsChrimson in flies used for AIP-DNpe050 behavioral epistasis. Arrows: cell body locations of DNpe050. Scale bar, 100μm.

(C) Fraction of flies performing wing elevation (i) and percentage of stimulation time with wing elevation (ii) during photostimulation of DNpe050-split1 (with Otd-FLP) under various LED frequencies and intensities. (iii and iv) Same quantifications for DNpe050-split2 (with Otd-FLP) activation. Results under 1.0 mW/mm^2, 40 Hz activation are duplicated from Figure 2D for the purpose of comparison.

(D) DNpe050 (with Otd-FLP) activation does not promote turning (i), charging (ii), or pumping (iii). Empty-split: N = 31. DNpe050-split1: N = 30. DNpe050-split2: N = 20.

(E) Silencing of DNpe050 (with Otd-FLP) using Kir2.1 did not impact lunging (i) or average velocity during recording (ii). Empty-split: N = 16 pairs. DNpe050-split1: N = 16 pairs. DNpe050-split2: N = 16 pairs.

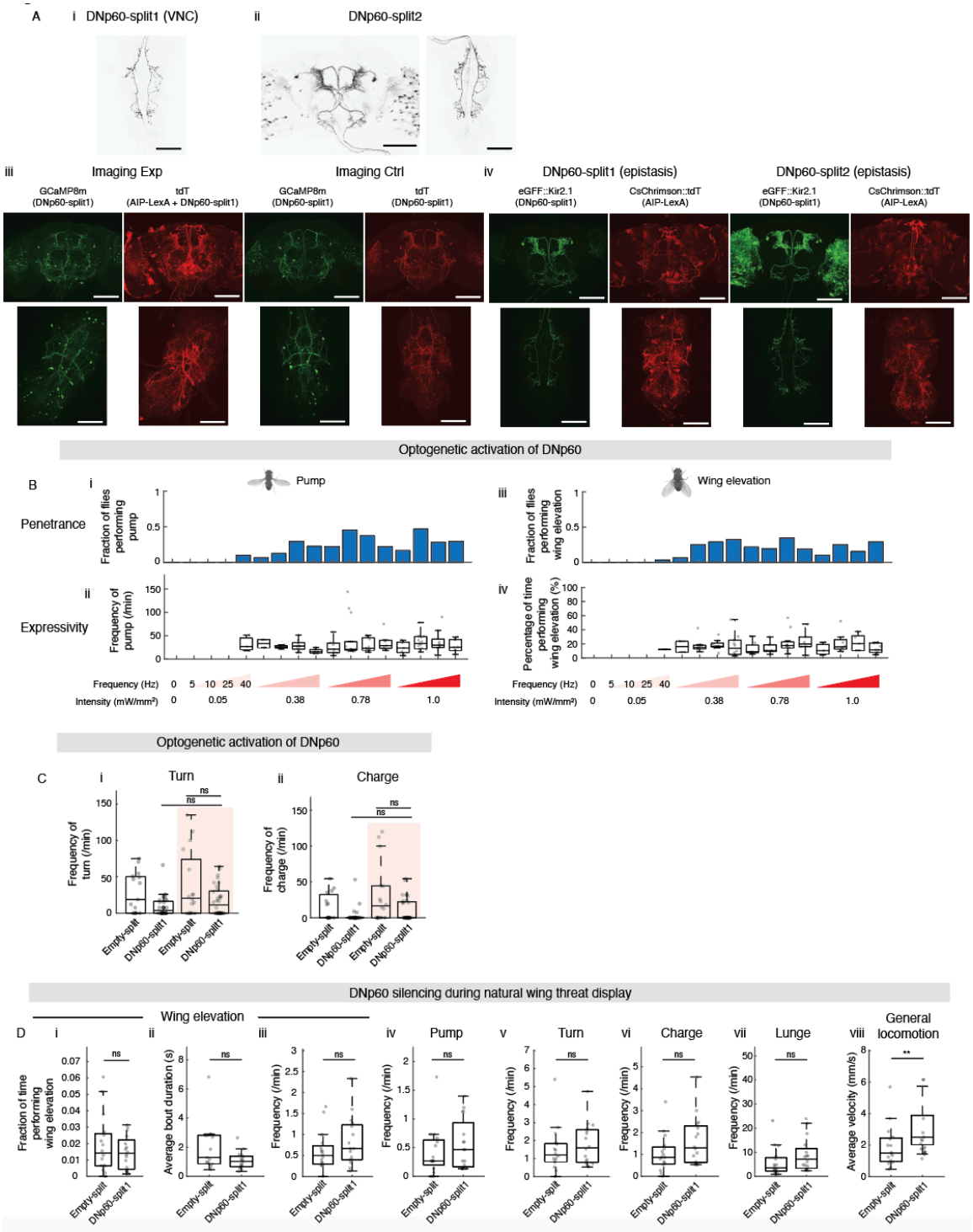
A
i DNp60-split1 (VNC)
ii DNp60-split2
iii
Imaging Exp
Imaging Ctrl
iv
DNp60-split1 (epistasis)
DNp60-split2 (epistasis)
GCaMP8m (DNp60-split1)
tdT (AIP-LexA + DNp60-split1)
GCaMP8m (DNp60-split1)
tdT (DNp60-split1)
eGFF::Kir2.1 (DNp60-split1)
CsChrimson::tdT (AIP-LexA)
eGFF::Kir2.1 (DNp60-split1)
CsChrimson::tdT (AIP-LexA)
Optogenetic activation of DNp60
B
i
Pump
Penetrance
Fraction of flies performing pump
ii
Expressivity
Frequency of pump (/min)
iii
Wing elevation
Fraction of flies performing wing elevation
iv
Percentage of time performing wing elevation (%)
Frequency (Hz) 0 5 10 25 40
Intensity (mW/mm²) 0 0.05 0.38 0.78 1.0
Optogenetic activation of DNp60
C
i
Turn
Frequency of turn (/min)
ns
ii
Charge
Frequency of charge (/min)
Empty-split
DNp60-split1
DNp60 silencing during natural wing threat display
D
Wing elevation
i
Fraction of time performing wing elevation
ii
Average bout duration (s)
iii
Frequency (/min)
iv
Pump
v
Turn
vi
Charge
vii
Lunge
viii
General locomotion
Average velocity (mm/s)
**

Figure S3. DNp60 does not evoke turning or charging

(A) Expression pattern of DNp60-split1 (VNC, with Otd-FLP) (i) and DNp60-split2 (with Otd-FLP) (ii). (iii) Expression pattern of GCaMP8m and tdT in experimental (Exp) and control (Ctrl) groups of DNp60 functional imaging. Note that in experimental group, tdT signal comes from both AIP-LexA>Chrimson::tdT and DNp60-split2>tdT. The control group does not contain the AIP-LexA transgene. (iv) Expression pattern of Kir2.1 and CsChrimson in flies used for DNp60 behavioral epistasis. Scale bar, 100μm.

(B) Fraction of flies performing at least one pump (i), frequency of pump (ii), fraction of flies performing at least one wing elevation bout (iii) and percentage of time performing wing elevation (iv) during photostimulation of DNp60-split1 (with Otd-FLP) under various LED frequencies and intensities. Results under 1.0 mW/mm^2, 10 Hz are duplicated from Figure 3D and 3E for purposes of comparison.

(C) DNp60 (with Otd-FLP) activation does not elicit turning (i) or charging (ii). Empty-split: N = 16. DNp60-split1: N = 32.

(D) Behavioral quantification of DNp60 (with Otd-FLP) silencing using Kir2.1: (i) fraction of time performing wing elevation, (ii) average wing elevation bout duration, (iii) frequency of wing elevation, (iv) frequency of pumps, (v) frequency of turns, (vi) frequency of charges, (vii) frequency of lunges, (viii) average velocity during recording. Results of empty-split group are the same as in Figure 2F and S2E. Empty-split: N = 16 pairs. DNp60-split1: N = 16 pairs.

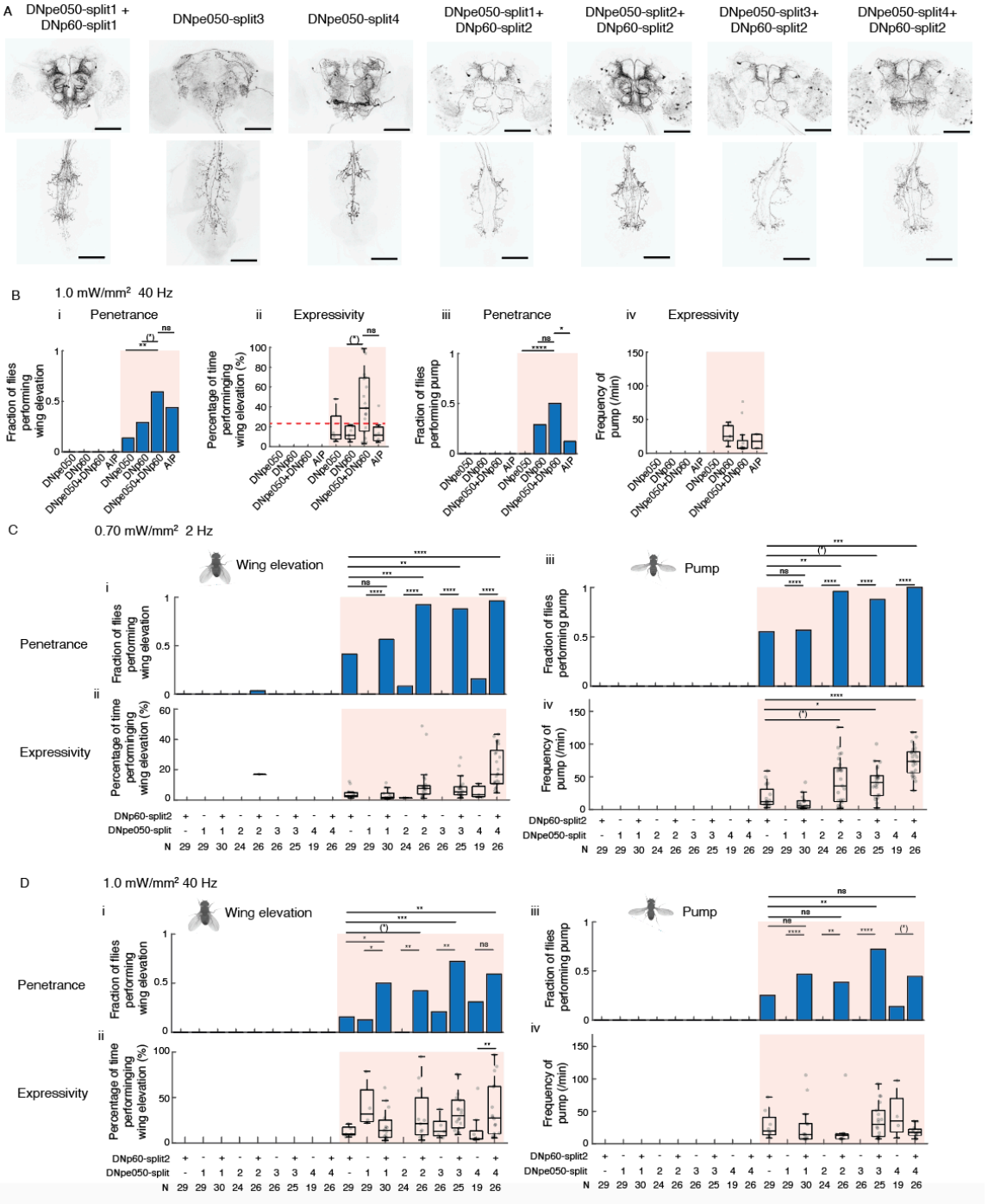
A
DNpe050-split1 + DNp60-split1
DNpe050-split3
DNpe050-split4
DNpe050-split1+ DNp60-split2
DNpe050-split2+ DNp60-split2
DNpe050-split3+ DNp60-split2
DNpe050-split4+ DNp60-split2
B
1.0 mW/mm² 40 Hz
i Penetrance
ii Expressivity
iii Penetrance
iv Expressivity
Fraction of flies performing wing elevation
Percentage of time performinging wing elevation (%)
Fraction of flies performing pump
Frequency of pump (/min)
DNpe050
DNp60
DNpe050+DNp60
AIP
C
0.70 mW/mm² 2 Hz
Wing elevation
Pump
Penetrance
Expressivity
DNp60-split2
DNpe050-split
N
D
1.0 mW/mm² 40 Hz
Wing elevation
Pump
Penetrance
Expressivity

Figure S4. DNpe050 and DNp60 synergistically control wing elevation and pump

(A) Expression pattern of DNpe050-split1 + DNp60-split1 (with Otd-FLP), DNpe050-split3 (with Otd-FLP), DNpe050-split4 (with Otd-FLP), and combinations between DNp60-split2 with DNpe050-split1/2/3/4 (with Otd-FLP). Scale bar, 100μm.

(B) Fraction of flies performing at least one wing elevation bout (i), percentage of time performing wing elevation (ii), fraction of flies performing at least one pump (iii), and frequency of pump (iv) during photostimulation of DNpe050 and DNp60 combined (with Otd-FLP, 1.0 mW/mm^2, 40 Hz, 10 ms pulse width). Results of DNp60 activation are duplicated from Figure S3B for purposes of comparison. DNpe050: N = 29. DNp60: N = 31. DNpe050+DNp60: N = 32. AIP: N = 16.

(C) Fraction of flies performing at least one wing elevation bout (i), percentage of time performing wing elevation (ii), fraction of flies performing at least one pump (iii), and frequency of pump (iv) during photostimulation of DNp60-split2 combined with DNpe050-split drivers (with Otd-FLP, 0.70 mW/mm^2, 2 Hz, 30 ms pulse width). N: number of flies in each group.

(D) Same as (C) but under LED parameters: 1.0 mW/mm^2, 40 Hz, 10 ms pulse width.

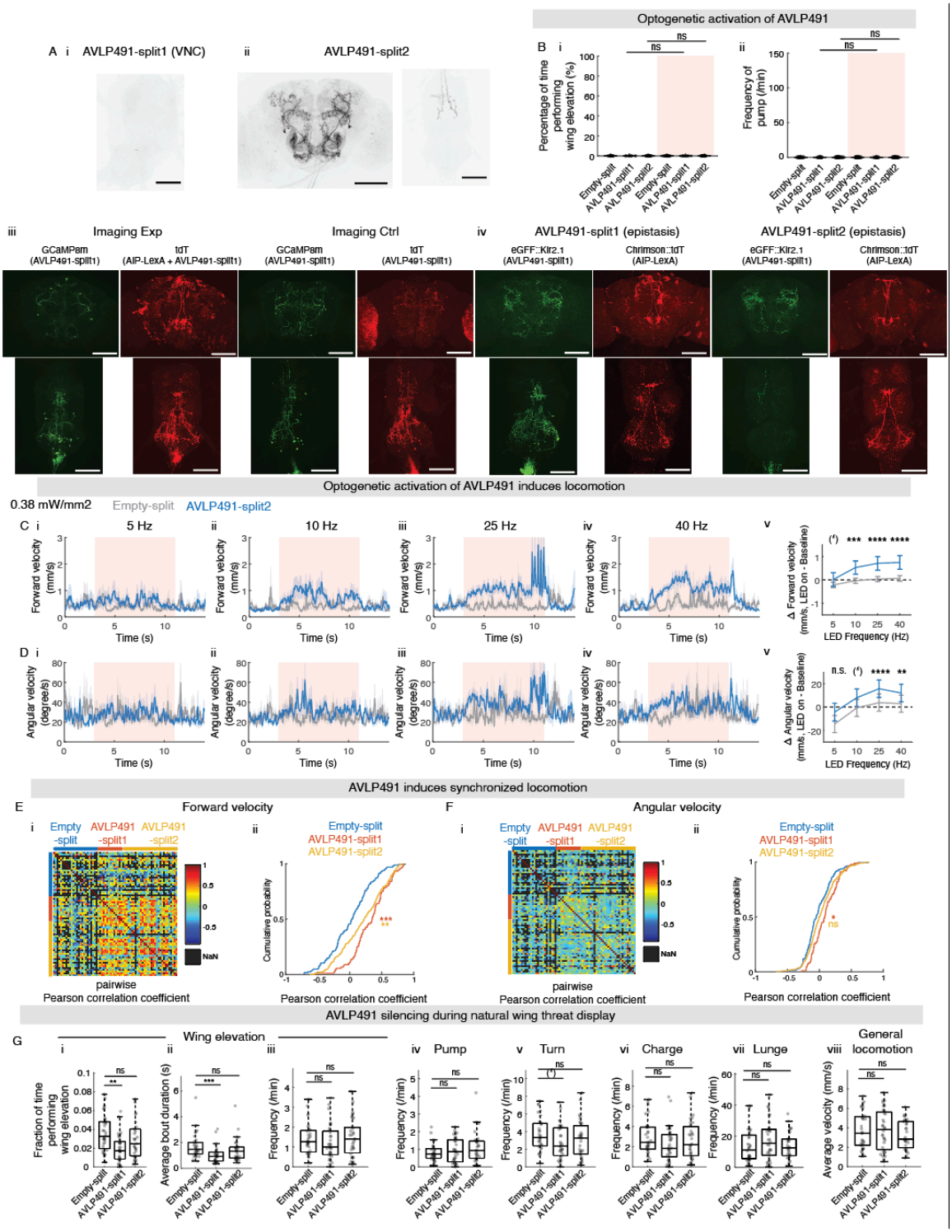
Optogenetic activation of AVLP491
A i AVLP491-split1 (VNC)
ii AVLP491-split2
B i
Percentage of time performing wing elevation (%)
ii
Frequency of pump (/min)
Empty-split
AVLP491-split1
AVLP491-split2
iii Imaging Exp
Imaging Ctrl
iv AVLP491-split1 (epistasis)
AVLP491-split2 (epistasis)
GCaMP8m (AVLP491-split1)
tdT (AIP-LexA + AVLP491-split1)
tdT (AVLP491-split1)
eGFF::Kir2.1 (AVLP491-split1)
Chrimson::tdT (AIP-LexA)
Optogenetic activation of AVLP491 induces locomotion
0.38 mW/mm2
C i 5 Hz
ii 10 Hz
iii 25 Hz
iv 40 Hz
v
Forward velocity (mm/s)
Time (s)
Δ Forward velocity (mm/s, LED on - Baseline)
LED Frequency (Hz)
D i
Angular velocity (degree/s)
Δ Angular velocity (mm/s, LED on - Baseline)
AVLP491 induces synchronized locomotion
E Forward velocity
F Angular velocity
pairwise Pearson correlation coefficient
Cumulative probability
AVLP491 silencing during natural wing threat display
G Wing elevation
Fraction of time performing wing elevation
Average bout duration (s)
Pump
Turn
Charge
Lunge
General locomotion
Average velocity (mm/s)

Figure S5. AVLP491 does not induce wing elevation or pump

(A) Expression pattern of AVLP491-split1 (VNC, with Otd-FLP) (i) and AVLP491-split2 (with Otd-FLP) (ii). (iii) Expression pattern of GCaMP8m and tdT in experimental (Exp) and control (Ctrl) groups of AVLP491 functional imaging. Note that in experimental group, tdT signal comes from both AIP-LexA>Chrimson::tdT and AVLP491-split2>tdT. The control group does not contain the AIP-LexA transgene. (iv) Expression pattern of Kir2.1 and Chrimson in flies used for AVLP491 behavioral epistasis. Scale bar, 100μm.

(B) Percentage of time flies performing wing elevation (i) and frequency of pump (ii) during AVLP491 (with Otd-FLP) activation in clean flies.

(C) Forward velocities before, during, and after optogenetic activation of AVLP491-split2 (with Otd-FLP) at 5 Hz (i), 10 Hz (ii), 25 Hz (iii) and 40 Hz (iv) in dusted flies. (v) Differences in average forward velocities during photostimulation compared to baseline. Statistical comparisons are performed between genetic and experimental groups. Lines and error bars denote mean ± SEM. Empty-split: N = 35 (5 Hz), 35 (10 Hz), 36 (25 Hz), 39 (40 Hz). AVLP491-split2: N = 34 (5 Hz), 35 (10 Hz), 37 (25 Hz), 36 (40 Hz).

(D) same as (C) but for angular velocities. In (C) and (D), experiments were performed in dusted flies with dim green background lighting to minimize the spontaneous and light-induced startle locomotion

(E) (i) A heatmap showing pairwise Pearson correlation coefficients of forward velocities during photostimulation of AVLP491 in clean flies. Each row and column indicate an individual fly. NaN: not a number, when data were not qualified for this analysis (see

Methods). (ii) Cumulative distribution of pairwise Pearson correlation coefficients displayed in (i).

(F) same as (E) but for angular velocities.

(G) Behavioral quantification of AVLP491 (with Otd-FLP) silencing using Kir2.1: (i) fraction of time performing wing elevation, (ii) average wing elevation bout duration, (iii) frequency of wing elevation, (iv) frequency of pumps, (v) frequency of turns, (vi) frequency of charges, (vii) frequency of lunges, (viii) average velocity during recording. Empty-split: N = 32 pairs. AVLP491-split1: N = 32 pairs. AVLP491-split2: N =31 pairs.

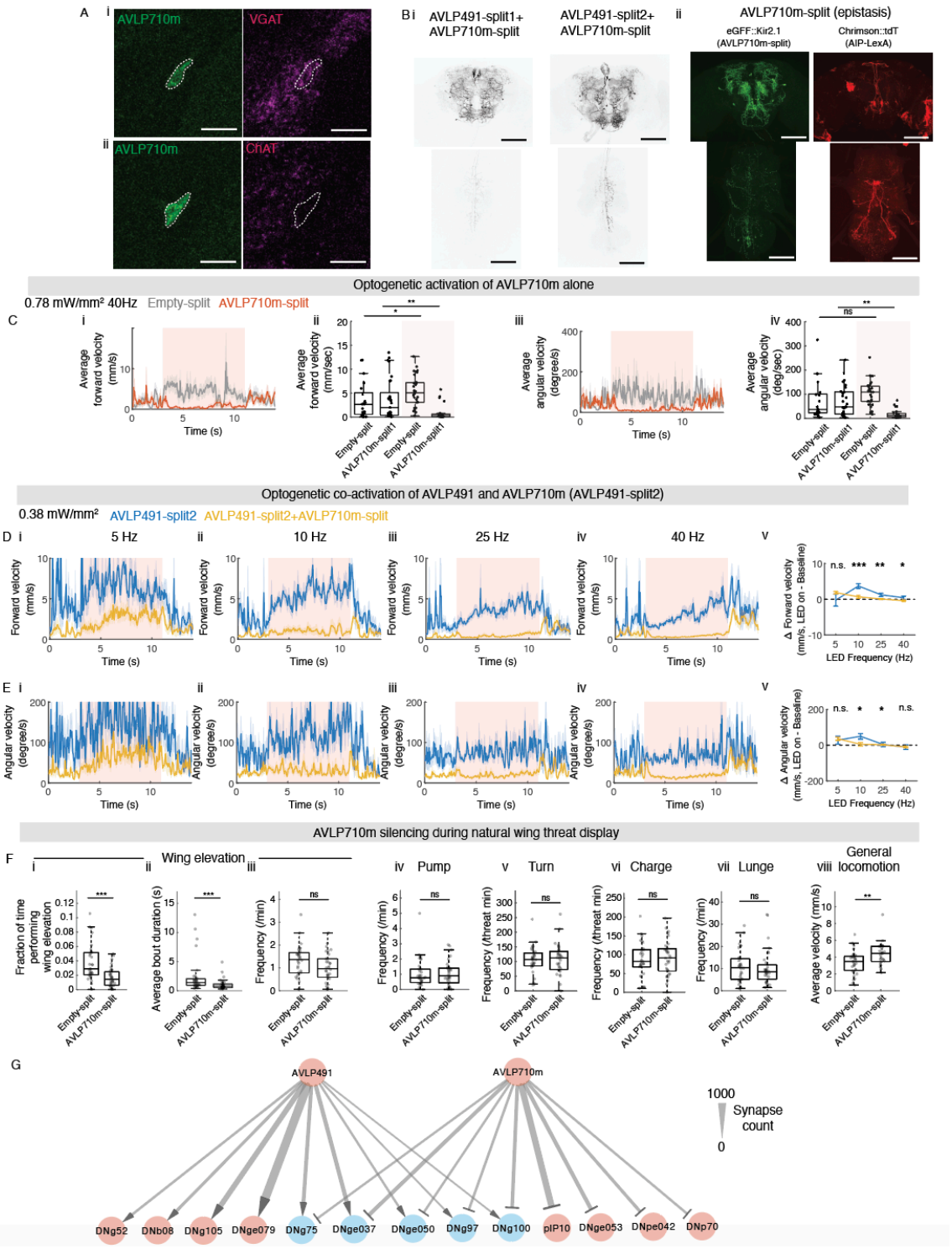
A
i
AVLP710m
VGAT
ii
AVLP710m
ChAT
B i
AVLP491-split1+
AVLP710m-split
AVLP491-split2+
AVLP710m-split
ii
AVLP710m-split (epistasis)
eGFF::Kir2.1
(AVLP710m-split)
Chrimson::tdT
(AIP-LexA)
Optogenetic activation of AVLP710m alone
0.78 mW/mm² 40Hz Empty-split AVLP710m-split
C
Average forward velocity (mm/s)
Time (s)
Average forward velocity (mm/sec)
Average angular velocity (degree/s)
Average angular velocity (deg/sec)
Empty-split
AVLP710m-split
Optogenetic co-activation of AVLP491 and AVLP710m (AVLP491-split2)
0.38 mW/mm² AVLP491-split2 AVLP491-split2+AVLP710m-split
D
5 Hz
10 Hz
25 Hz
40 Hz
Forward velocity (mm/s)
Δ Forward velocity (mm/s, LED on - Baseline)
LED Frequency (Hz)
E
Angular velocity (degree/s)
Δ Angular velocity (mm/s, LED on - Baseline)
AVLP710m silencing during natural wing threat display
F
Wing elevation
Pump
Turn
Charge
Lunge
General locomotion
Fraction of time performing wing elevation
Average bout duration (s)
Frequency (/min)
Frequency (/threat min)
Average velocity (mm/s)
G
AVLP491
AVLP710m
1000
Synapse count
0
DNg52
DNb08
DNg105
DNge079
DNg75
DNge037
DNge050
DNg97
DNg100
pIP10
DNge053
DNpe042
DNp70

Figure S6. AVLP710m is GABAergic and projects to an overlapping set of DNs with AVLP491

(A) (i) Fluorescence *in situ* hybridization for VGAT (i) and ChAT (ii) in AVLP710m. Dashed lines indicate the cell body locations of AVLP710m. Scale bar, 10μm.

(B) (i) Expression pattern of combinations of AVLP710m and AVLP491-split1/2. (ii) Expression pattern of Kir2.1 and Chrimson in flies used for AVLP710m behavioral epistasis. Scale bar, 100μm.

(C) (i) Forward velocities before, during, and after optogenetic activation of AVLP710m (with Otd-FLP). (ii) Average forward velocities before and during photostimulation. (iii-iv) same as (i-ii) but for angular velocities.

(D) Forward velocities before, during, and after optogenetic activation of AVLP491 (with Otd-FLP) alone or AVLP491 and AVLP710m combined (with Otd-FLP) at 5 Hz (i), 10 Hz (ii), 25 Hz (iii) and 40 Hz (iv). (v) Differences in average forward velocities during photostimulation compared to baseline. Statistical comparisons are performed between the control and experimental groups. Lines and error bars denote mean ± SEM. AVLP491-split2: N = 29 (5 Hz), 30 (10 Hz), 31 (25 Hz), 27 (40 Hz). AVLP491-split2+AVLP710m-split: N = 26 (5 Hz), 25 (10 Hz), 26 (25 Hz), 25 (40 Hz).

(E) same as (D) but for angular velocities.

(F) Behavioral quantifications of AVLP710m (with Otd-FLP) silencing using Kir2.1: (i) fraction of time performing wing elevation, (ii) average wing elevation bout duration, (iii) frequency of wing elevation, (iv) frequency of pumps, (v) frequency of turns during wing

threat, (vi) frequency of charges during wing threat, (vii) frequency of lunges, (viii) average velocity during recording. Empty-split: N = 32 pairs. AVLP710m-split: N = 32 pairs. (G) A circuit diagram highlighting the top downstream DN targets of AVLP491 and AVLP710m. Blue circles highlight the common downstream targets.

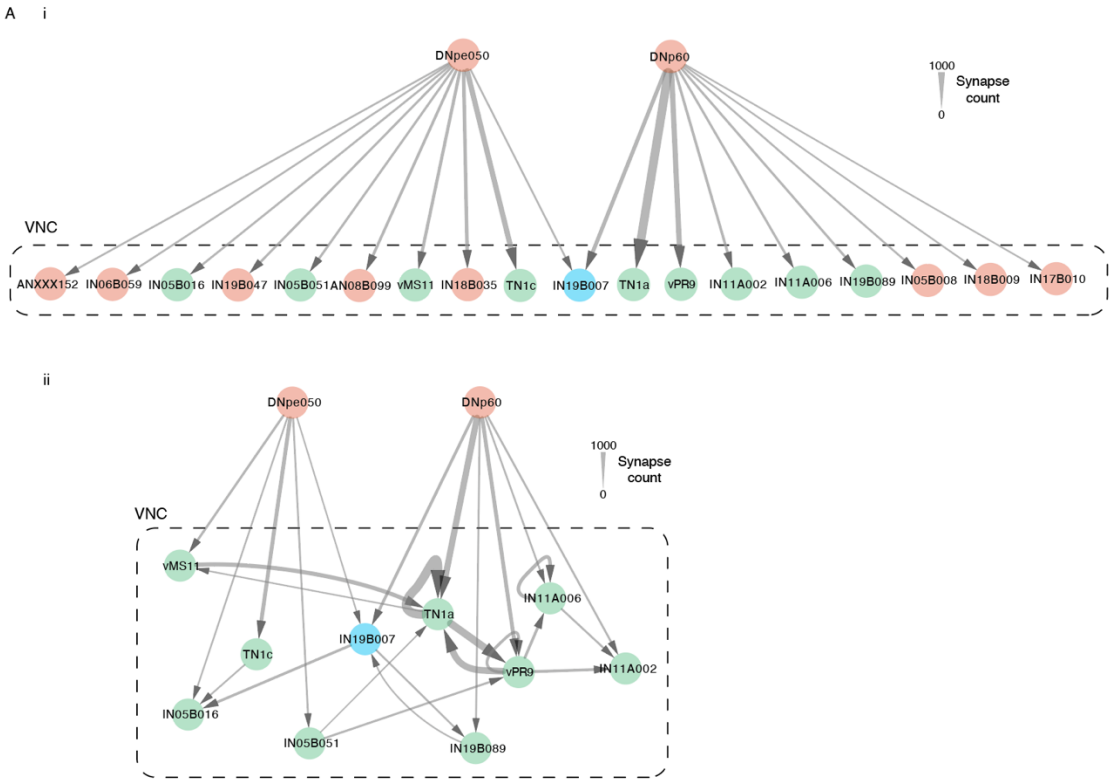
A i
DNpe050
DNp60
1000
Synapse count
0
VNC
ANXXX152
IN06B059
IN05B016
IN19B047
IN05B051
AN08B099
vMS11
IN18B035
TN1c
IN19B007
TN1a
vPR9
IN11A002
IN11A006
IN19B089
IN05B008
IN18B009
IN17B010
ii
DNpe050
DNp60
1000
Synapse count
0
VNC
vMS11
TN1a
IN11A006
IN19B007
TN1c
vPR9
IN11A002
IN05B016
IN05B051
IN19B089

Figure S7. VNC circuit diagram of DNpe050 and DNp60

(A) Circuit diagrams of DNpe050 and DNp60 downstream VNC targets in Male CNS Connectome. (i) Top downstream VNC targets of DNpe050 and DNp60. Only direct connectivity from DNpe050/DNp60 to downstream targets is displayed. Synapse count cut off: 150 synapses. (ii) A circuit diagram of interconnectivity among DNpe050/DNp60 direct VNC downstream targets. Blue highlights the common downstream target. Green highlights the same neurons displayed in (i) and (ii).

Materials and Methods

Fly Strains

A detailed description of all genotypes used in each experiment is provided in Table S1, and the source of each strain is listed in the Key Resources Table. SS33004 (DNp60-split2), 10xUAS-eGFPKir2.1 (attP2), 20xUAS->myrTopHat2->Chrimson::tdT3.1 (VK5), 20xUAS-Chrimson:tdT(Su(Hw)attP5), 13xLexAop2-Chrimson::tdT3.1 (Su(Hw)attP5), 13xLexAop2-IVS-Syn21-CsChrimson::tdT3.1 (VK5) were kindly shared by the Gerald Rubin laboratory (HHMI Janelia Research Campus) and Barret Pfeiffer. SS33004 (DNp60-split2) was kindly shared by Jens Goldammer and Gerald Rubin. Confocal images of the SS33004 line and other information are available from the Omnibus Broad database[80]. The following strains were obtained from the Bloomington *Drosophila* Stock Center (Indiana University): 10xUAS-IVS-myr::tdTomato3.1 (attP2), 20xUAS-IVS-jGCaMP8m (VK5), 20xUAS-IVS-jGCaMP7b(VK5), VT058429-AD (attP40), 12G09-DBD (attP2), VT061518-DBD (attP2), VT045669-DBD (attP2), 54A01-AD (attP40), VT056582-DBD (attP2), VT016281-DBD (attP2), VT008974-AD (attP40), VT025952-DBD (attP2), 46A02-AD (attP40), 85F12-AD (attP40), VT032899-DBB (attP2), Empty-split (BDP-AD (attP40); BDP-DBD (attP2)).

Rearing Conditions

Flies were maintained at 25°C and 50% relative humidity on a 12hr:12hr light-dark cycle. Crosses were established with 10-14 virgin females and 3-5 males and transferred to fresh vials every 3-4 days. Experimental flies were collected on day 0-3 post eclosion.

For group-housed condition (used in optogenetic activation and behavioral epistasis experiments), flies were kept at a density of 15-25 individuals per vial. For single-housed condition (used in silencing experiments), flies were reared individually. All experiments were performed 6-8 days after collection.

Flies were reared on standard molasses-based medium. For optogenetic activation and behavioral epistasis experiments, flies were reared in constant darkness on food supplemented with 0.4mM all-trans-retinal after collection and transferred to fresh all-trans-retinal food 1-2 days before testing.

Construction of Transgenic Animals

The following fly strains were generated in this study: VT058429EB1-AD, VT058429EB2-AD, VT058429EB3-AD, VT058429EB4-AD, VT058429EB5-AD, 12G09EB1-DBD, 12G09EB2-DBD, 12G09EB3-DBD, 12G09EB4-DBD, 12G09EB5-DBD. DNA fragments used for enhancer-bashing were derived from the original VT058429[35,81] and 12G09[34,82,83] enhancer sequences and were synthesized by Integrated DNA Technologies, Inc., with the exception of 12G09EB1, due to a complex sequence feature. Instead, 12G09EB1 was amplified from genomic DNA. EB1, EB2, and EB3 tile and roughly equally divide the parental segments. Breakpoints were selected to (i) sit in evolutionary non-conserved positions, (ii) avoid open chromatin regions, and (iii) meet the sequence requirements for DNA synthesis by IDT, Inc. EB4 and EB5 are of similar length to EB1-3 and were selected to cover the gaps between EB1 and EB2, and between EB2 and EB3, in case a cis-regulatory motif is interrupted. The start and end positions of each segment are as follows:

VT058429EB1 (700 bp):

AATTTAAGGATATGA…CATGTCCTGCCTTCT

VT058429EB2 (830 bp):

GCCTGCCTCTGTCAG…ATACGATTTCAGTGT

VT058429EB3 (674 bp):

TGTGTTTGGGAAAGA…CTGCCGCCAGGTGGC

VT058429EB4 (691 bp):

AATTCGGCGAAAAGA…GTGGAAGATATAGGG

VT058429EB5 (682 bp):

GCAGTTGCAGTTGCA…TTAATGGGAAATGGT

12G09EB1 (815 bp):

CACATGGCGGTTCAG…AGCTGATTGCTACCC

12G09EB2 (1227 bp):

TGTTGCCAGTTGTCC…ATACATTTTCAACAC

12G09EB3 (1027 bp):

GACGTAGTGGGATTT…GCACACCTGAGTGGC

12G09EB4 (990 bp):

TATATGTATGTATAT…TGGGGGTGGTGTGGT

12G09EB5 (990 bp):

CGGCGCTAGCATTTG…TTTGAAAAACATTTA

Cloning procedures followed previous reports[82,83]. Briefly, DNA fragments were inserted into pBPp65ADZpUw (Addgene #26234) and pBPZpGAL4DBD (Addgene

#26233) vectors using Gateway cloning and the LR recombination reaction. Germline transformation was performed by BestGene, Inc.

Immunohistochemistry and Confocal Imaging

Brains or ventral nerve cords were dissected in ice-cold phosphate-buffered saline (PBS) and fixed in 4% paraformaldehyde for 20 min at room temperature. Samples were washed three times in 0.5% PBST (PBS containing 0.5% Triton X-100), for 10 min each at room temperature, then permeabilized in 2% PBST for 30 min at room temperature. Blocking was performed in 5% normal goat serum (NGS) prepared in 0.5% PBST for 1 h at room temperature or overnight at 4°C. Tissues were incubated with primary antibody for at least 48 hours at 4°C (anti-GFP 1:1000, anti-DsRed 1:1000, nc82 1:50), followed by three 10-min washes in 0.5% PBST. Secondary antibodies (1:1000) were applied for 40-48 hours at 4°C, and samples were again washed three times in 0.5% PBST before mounting.

Samples were mounted in Vectashield (Vector Laboratories, Inc.) and imaged on an Olympus Fluoview FV3000 confocal microscope under a 30X objective. Image stacks were acquired at optimal z-step intervals for subsequent analysis. Brain images displayed were maximum intensity projection (MIP) generated in Fiji. Images in Figure 2B and 6B were registered to JRC2018U[84] using the Fiji CMTK registration GUI[85] before MIP generation.

HCR fluorescence In Situ Hybridization

For hybridization chain reaction (HCR) *in situ* hybridization, fly heads were pre-fixed in 4% PFA on ice and dissected in cold PBS. Brains were fixed for 2 hours at 4°C, and HCR

v3.0 was performed as previously reported[43] (also see https://www.moleculartechnologies.org/supp/HCRv3_protocol_generic_solution.pdf), using RNase-free reagents throughout. Following the HCR procedure, brains were post-fixed in 4% PFA for 20 minutes at room temperature, then processed for immunostaining and confocal imaging as described above to label specific cell types.

Behavioral Assays

All behavioral experiments were conducted at 25°C and 50% relative humidity during zeitgeber time (ZT) 0-4h. Behavioral chambers were illuminated from below with 850 nm infrared backlights (SOBL-200x150-850, Smart Vision Lights). Videos were recorded from above at 30 frames/s using Blackfly S USB3 cameras (BFS-U3-13Y3M-C) equipped with long-pass infrared filters (LP780, Midwest Optical Systems). For all behavioral experiments, an 8-well chamber was used, consisting of 12 mm high x 16 mm diameter acrylic cylinders[86]. The floor of the chamber was uniformly coated with apple juice agar.

For optogenetic activation and behavioral epistasis assays, flies were group-housed after collection for rearing. During the experiment, one male fly was loaded per well using a mouth aspirator. Optogenetic stimulation was delivered using a custom LED setup as described previously[86], with a 655 nm LED (SR-05-D000, Luxeon Star LED) positioned ~8 cm above each well at a 24° angle. The stimulation protocol began with a 15 s baseline, followed by sixteen 8 s light periods, each separated by a 15 s interval. For optogenetic activation experiments, stimulation parameters consisted of all combinations of 5, 10, 25,

and 40 Hz with light intensities of 0.05, 0.38, 0.78, 1.0 mW/mm^2, each light pulse lasting 10 ms, or all combinations of 1, 2, 3, 4 Hz with light intensities of 0.45, 0.7, 0.95, 1.2 mW/mm^2, each light pulse lasting 30 ms for low frequency stimulation. For behavioral epistasis experiments, stimulation parameters consisted of all combinations of 1, 7, 13, 19, 25, 31, and 37 Hz with intensities of 0.18 and 0.50 mW/mm^2, each pulse lasting 10 ms. In both cases, the total recording time was 420 s. For Kir2.1 silencing experiments, flies were single-housed immediately after collection for rearing. During experiment, two males of the same genotype were introduced into each well of the 8-well chamber. Each recording lasted 15 minutes.

For AVLP491 activation experiments in Figure 5D and S5C, flies were dusted with Reactive Yellow 86 to minimize spontaneous locomotion, and the chambers were illuminated with a dim green background light (0.0036 mW/mm^2) to prevent red LED-induced startle locomotion as described previously[41,42].

In all experiments, the chamber walls were coated with Insect-A-Slip or Fluon (Tar Heel Ants, Raleigh, NC), and the lids were coated with silicon fluid to prevent climbing, and flies were allowed to acclimate for 4 min after being transferred into the chamber before the video recording started.

Two-photon functional imaging

Two-photon calcium imaging was performed following previously described procedures[87] with minor modifications. Flies were briefly anesthetized on ice for 20-30 s and transferred to an aluminum plate with an open slit that physically restrained the body. The plate was kept cool with ice throughout preparation. Each fly was then mounted onto a

custom holder[88] using UV-cured glue to secure the head, and the proboscis was glued in place to minimize brain motion. The holder was then filled with physiological saline (108 mM NaCl, 5 mM KCl, 4 mM $NaHCO_3$, 1 mM NaH_2PO_4, 5 mM trehalose, 10 mM sucrose, 5 mM HEPES, 0.5 mM $CaCl_2$, 2 mM $MgCl_2$, pH = 7.5). A small piece of head cuticle, along with overlying trachea and adipose tissues, was removed to expose the brain, and the esophagus was severed to further reduce movement artifacts.

Calcium imaging was conducted on a custom-modified Ultima two-photon laser-scanning microscope (Bruker). Cell bodies of interest were scanned at 3 frames/s using a 920 nm laser (Chameleon Ultra II Ti:Sapphire laser, Coherent), and images were collected through a 25x objective (XLPlan N, Olympus) with a numerical aperture of 1.00.

For photostimulation, a 655nm LED was placed at ~1 cm below the fly. Recording includes a 30 s baseline period, 5 s stimulation periods, each separated by a 55 s recovery interval. Stimulation parameters consist of all combinations of 5, 10, 20, and 40 Hz at the intensities of 0.3, 0.5, and 0.9 mW/mm^2. The LED was controlled and synchronized with image acquisition via an Arduino-based interface and custom-written scripts. To minimize leak-through into the imaging channel, the LED source was covered with three layers of Roscolux 26 filters (Rosco).

QUANTIFICATION AND STATISTICAL ANALYSIS

Statistics

All statistical analyses were performed in MATLAB. Table S2 provides a complete summary of the sample size (n) for each experiment, the statistical test used, the resulting *p*-values, and

the adjusted α significance threshold when Bonferroni's multiple comparison correction was applied.

Connectome analysis

Analyses were performed using the male CNS connectome dataset[28] (https://neuprint.janelia.org/, male-cns:v0.9), accessed through the neuPrint interface[89] and the natverse package[90] in R. Connections between neuron pairs with five synapses or fewer were excluded. The remaining connections were used to generate a connectivity table, which was imported into Cytoscape (cytoscape.org) for circuit diagram construction. In these diagrams, neurons of the same type from both hemispheres were grouped into a single node, and synapse counts were summed to represent the connection strength between two cell types. Reconstructed neuron skeletons were registered to the JRC2018U brain template[84]. NeuronBridge[30] was used to identify candidate hemi-drivers, and Split-GAL4 combinations were subsequently generated for anatomical and functional screening.

For AIP subtype analysis, downstream targets included the neuron types with the highest synaptic connectivity to AIP, as well as neurons identified as functionally important for threat behavior (e.g. DNp60). Pairs of AIP neurons were grouped into single types based on morphology, and their synapse counts were summed. Heatmaps displaying synapse counts between neuron types were generated with ComplexHeatmap package[91] in R. Hierarchical clustering was performed with ComplexHeatmap using the complete-linkage method based on Euclidean distance. AIP1 and AIP2 were selected from the highest branching level of the resulting dendrogram.

Fly tracking and behavior classification

Behavioral recordings were processed with Caltech FlyTracker[92] to extract various features from the videos such as the positions and the velocities of the flies.

For optogenetic activation and behavioral epistasis experiments, threat action classification followed our previous report[16] with additional filtering steps to improve accuracy in the assays used in this study. Periods during which flies remained vertically on the behavior chamber wall were excluded from analysis, as wall climbing often caused tracking errors. Stable wing elevation was defined as both wings extended between 35° and 65° for more than 0.2 s. Pump was defined as average wing angle exceeding 65°. Turning and charging were classified by identifying bouts where angular velocity exceeded 75°/s and forward velocity exceeded 6 mm/s, respectively. To specifically identify discrete events, bouts occurring during periods of sustained locomotion (>20°/s angular velocity or >2mm/s forward velocity for more than 0.4 s) were removed, retaining only discrete and brief events. Immobility was defined as periods when the angular velocity is lower than 10°/s and forward velocity is lower than 1mm/s. For Figure 7G, the forward velocity threshold for charging-like behavior was set to 3 mm/s, as coactivation did not generate as high forward velocities characteristic of AIP activation or natural wing threat. Behavioral frequencies were calculated as the number of bouts divided by the total time during photostimulation when flies were not on the wall. 3, 5 or, 8 seconds prior to the stimulation onset were used as baseline. For behavioral epistasis experiments, stimulation conditions where genetic controls displayed the highest levels of threat behavior were used for quantification. In optogenetic

activation experiments, false-positive wing elevation and pump events were manually removed.

For Kir2.1 silencing experiments examining natural wing threat, a JAABA classifier was used to detect bouts of natural wing threat, and lunging was identified with a previously published JAABA classifier[22]. Misidentified bouts resulting from wall climbing were excluded. Each wing threat bout was counted as a single wing elevation bout. All classified wing threat bouts were then manually proofread. For identifying pump, turning, and charging, a 0.5 s window before and after each wing elevation bout was included for analysis, following the convention of our previous study[16], and the same criteria and filtering were applied as described above. Action frequency was calculated as the number of bouts divided by the total recording duration. When there were significant differences in fraction of time performing wing elevation, frequency of turns and charges was normalized to the length of analysis time window (wing elevation period plus 0.5 s before and after).

Stuttering score

The “stuttering” score was calculated to quantify the periodicity of immobility bouts during photostimulation. For each fly, a binarized immobility vector (1 = immobile, 0 = mobile) was extracted for each stimulation block. A fast Fourier transform (FFT) was applied to this binarized vector, and the power spectrum was computed across the corresponding frequency axis. The power at the frequency bin closest to the LED stimulation frequency for that block was extracted and normalized by the total power across all frequencies, yielding the stuttering score for that fly. Scores were then aggregated across flies within each genotype for statistical comparison and plotting.

Pearson Correlation Coefficient

Periods when flies were positioned vertically on the chamber wall were excluded from analysis. To remove artifacts from extreme movements such as jumping or flying, frames in which angular velocity exceeded 1,000°/s or forward velocity exceeded 100 mm/s were also excluded. If two flies share less than 10% overlap in post-filtered recording time, the Pearson correlation coefficient was not computed and was recorded as *Not a Number* (NaN). Cumulative distribution plots were generated using all non-NaN data points. Statistical significance between two genotypes was assessed via a random-labeling bootstrap implemented in a custom MATLAB script. In each iteration, genotype labels were shuffled across all individuals, and the difference in the medians of the Pearson correlation coefficients between two groups was calculated. This process was repeated 10,000 times. The *p*-value was computed as the proportion of the iterations in which the simulated difference exceeded the observed difference.

Two-photon imaging data analysis

After image acquisition, a circular region of interest (ROI) was manually drawn in Fiji to encompass the cell body. Pixel intensity within the ROI was measured across the entire recording session using a custom written MATLAB script, yielding the raw fluorescence trace. The first 20 seconds of each recording were used to establish the baseline fluorescence (F_0). Changes in fluorescence were then expressed as dF/F, calculated relative to this baseline.

Reference

1. Scholes, E., and Laman, T.G. (2018). Distinctive courtship phenotype of the Vogelkop Superb Bird-of-Paradise Lophorina niedda Mayr, 1930 confirms new species status. PeerJ *6*, e4621. https://doi.org/10.7717/peerj.4621.

2. Parnell, R.J., and Buchanan-Smith, H.M. (2001). An unusual social display by gorillas. Nature *412*, 294–294. https://doi.org/10.1038/35085631.

3. Nelson, X.J., and Jackson, R.R. (2010). Complex display behaviour during the intraspecific interactions of myrmecomorphic jumping spiders (Araneae, Salticidae). Journal of Natural History *41*, 1659–1678. https://doi.org/10.1080/00222930701450504.

4. LOXTON, R.G. (1979). On display behaviour and courtship in the praying mantis Ephestiasula amoena (Bolivar). Zool J Linn Soc *65*, 103–110. https://doi.org/10.1111/j.1096-3642.1979.tb01083.x.

5. Van Parijs, S.M., Hastie, G.D., and Thompson, P.M. (2000). Individual and geographical variation in display behaviour of male harbour seals in Scotland. Animal Behaviour *59*, 559–568. https://doi.org/10.1006/anbe.1999.1307.

6. Brown, B.V., and Porras, W. (2015). Extravagant female sexual display in a Megaselia Rondani species (Diptera: Phoridae). Biodiversity Data Journal *3*, e4368. https://doi.org/10.3897/BDJ.3.e4368.

7. Cárdenas-Posada, G., Cadena, C.D., Blake, J.G., and Loiselle, B.A. (2018). Display behaviour, social organization and vocal repertoire of Blue-backed Manakin Chiroxiphia pareola napensis in northwest Amazonia. Ibis *160*, 269–282. https://doi.org/10.1111/ibi.12548.

8. Mikula, P., Toszogyova, A., and Albrecht, T. (2022). A global analysis of aerial displays in passerines revealed an effect of habitat, mating system and migratory traits. Proceedings of the Royal Society B: Biological Sciences *289*, 20220370. https://doi.org/10.1098/rspb.2022.0370.

9. Rubenstein, D.I., and Hazlett, B.A. (1974). Examination of the Agonistic Behaviour of the Crayfish Orconectes Virilis By Character Analysis. Behaviour *50*, 193–215. https://doi.org/10.1163/156853974X00453.

10. Lin, D., Boyle, M.P., Dollar, P., Lee, H., Lein, E.S., Perona, P., and Anderson, D.J. (2011). Functional identification of an aggression locus in the mouse hypothalamus. Nature *470*, 221–226. https://doi.org/10.1038/nature09736.

11. Lee, H., Kim, D.-W., Remedios, R., Anthony, T.E., Chang, A., Madisen, L., Zeng, H., and Anderson, D.J. (2014). Scalable control of mounting and attack by Esr1 + neurons in the ventromedial hypothalamus. Nature *509*, 627–632. https://doi.org/10.1038/nature13169.

12. Wu, Z., Autry, A.E., Bergan, J.F., Watabe-Uchida, M., and Dulac, C.G. (2014). Galanin neurons in the medial preoptic area govern parental behaviour. Nature *509*, 325–330. https://doi.org/10.1038/nature13307.

13. Yang, C.F., Chiang, M.C., Gray, D.C., Prabhakaran, M., Alvarado, M., Juntti, S.A., Unger, E.K., Wells, J.A., and Shah, N.M. (2013). Sexually dimorphic neurons in the ventromedial hypothalamus govern mating in both sexes and aggression in males. Cell *153*, 896–909. https://doi.org/10.1016/j.cell.2013.04.017.

14. Kimura, K., Hachiya, T., Koganezawa, M., Tazawa, T., and Yamamoto, D. (2008). Fruitless and Doublesex Coordinate to Generate Male-Specific Neurons that Can Initiate Courtship. Neuron *59*, 759–769. https://doi.org/10.1016/j.neuron.2008.06.007.

15. Hoopfer, E.D., Jung, Y., Inagaki, H.K., Rubin, G.M., and Anderson, D.J. (2015). P1 interneurons promote a persistent internal state that enhances inter-male aggression in Drosophila. eLife *4*, e11346. https://doi.org/10.7554/eLife.11346.

16. Duistermars, B.J., Pfeiffer, B.D., Hoopfer, E.D., and Anderson, D.J. (2018). A Brain Module for Scalable Control of Complex, Multi-motor Threat Displays. Neuron *100*, 1474-1490.e4. https://doi.org/10.1016/j.neuron.2018.10.027.

17. Tao, L., Ayambem, D., Barranca, V.J., and Bhandawat, V. (2024). Neurons Underlying Aggression-Like Actions That Are Shared by Both Males and Females in *Drosophila*. J. Neurosci. *44*, e0142242024. https://doi.org/10.1523/JNEUROSCI.0142-24.2024.

18. Kravitz, E.A., and Fernandez, M. de la P. (2015). Aggression in Drosophila. Behavioral Neuroscience *129*, 549–563. https://doi.org/10.1037/bne0000089.

19. Hoopfer, E.D. (2016). Neural control of aggression in Drosophila. Current Opinion in Neurobiology *38*, 109–118. https://doi.org/10.1016/j.conb.2016.04.007.

20. Asahina, K., Watanabe, K., Duistermars, B.J., Hoopfer, E., González, C.R., Eyjólfsdóttir, E.A., Perona, P., and Anderson, D.J. (2014). Tachykinin-Expressing Neurons Control Male-Specific Aggressive Arousal in Drosophila. Cell *156*, 221–235. https://doi.org/10.1016/j.cell.2013.11.045.

21. Watanabe, K., Chiu, H., Pfeiffer, B.D., Wong, A.M., Hoopfer, E.D., Rubin, G.M., and Anderson, D.J. (2017). A Circuit Node that Integrates Convergent Input from Neuromodulatory and Social Behavior-Promoting Neurons to Control Aggression in Drosophila. Neuron *95*, 1112-1128.e7. https://doi.org/10.1016/j.neuron.2017.08.017.

22. Chiu, H., Hoopfer, E.D., Coughlan, M.L., and Anderson, D.J. (2021). A circuit logic for sexually shared and dimorphic aggressive behaviors in Drosophila. Cell *184*, 507-520.e16. https://doi.org/10.1016/j.cell.2020.11.048.

23. Deutsch, D., Pacheco, D., Encarnacion-Rivera, L., Pereira, T., Fathy, R., Clemens, J., Girardin, C., Calhoun, A., Ireland, E., Burke, A., et al. (2020). The neural basis for a persistent internal state in Drosophila females. eLife *9*, e59502. https://doi.org/10.7554/eLife.59502.

24. Palavicino-Maggio, C.B., Chan, Y.-B., McKellar, C., and Kravitz, E.A. (2019). A small number of cholinergic neurons mediate hyperaggression in female Drosophila. PNAS *116*, 17029–17038. https://doi.org/10.1073/pnas.1907042116.

25. Schretter, C.E., Aso, Y., Robie, A.A., Dreher, M., Dolan, M.-J., Chen, N., Ito, M., Yang, T., Parekh, R., Branson, K.M., et al. (2020). Cell types and neuronal circuitry underlying female aggression in Drosophila. eLife *9*, e58942. https://doi.org/10.7554/eLife.58942.

26. Chen, S., Lee, A.Y., Bowens, N.M., Huber, R., and Kravitz, E.A. (2002). Fighting fruit flies: A model system for the study of aggression. PNAS *99*, 5664–5668. https://doi.org/10.1073/pnas.082102599.

27. Gould, S.J., and Vrba, E.S. (1982). Exaptation-A Missing Term in the Science of Form. Paleobiology *8*, 4–15.

28. Nern, A., Loesche, F., Takemura, S., Burnett, L.E., Dreher, M., Gruntman, E., Hoeller, J., Huang, G.B., Januszewski, M., Klapoetke, N.C., et al. (2025). Connectome-driven neural inventory of a complete visual system. Nature *641*, 1225–1237. https://doi.org/10.1038/s41586-025-08746-0.

29. Berg, S., Beckett, I.R., Costa, M., Schlegel, P., Januszewski, M., Marin, E.C., Nern, A., Preibisch, S., Qiu, W., Takemura, S., et al. (2025). Sexual dimorphism in the complete connectome of the Drosophila male central nervous system. Preprint at bioRxiv, https://doi.org/10.1101/2025.10.09.680999 https://doi.org/10.1101/2025.10.09.680999.

30. Clements, J., Goina, C., Hubbard, P.M., Kawase, T., Olbris, D.J., Otsuna, H., Svirskas, R., and Rokicki, K. (2024). NeuronBridge: an intuitive web application for

neuronal morphology search across large data sets. BMC Bioinformatics *25*, 114. https://doi.org/10.1186/s12859-024-05732-7.

31. Otsuna, H., Ito, M., and Kawase, T. (2018). Color depth MIP mask search: a new tool to expedite Split-GAL4 creation. bioRxiv, 318006. https://doi.org/10.1101/318006.

32. Mais, L., Hirsch, P., Managan, C., Wang, K., Rokicki, K., Svirskas, R.R., Dickson, B.J., Korff, W., Rubin, G.M., Ihrke, G., et al. (2021). PatchPerPixMatch for Automated 3d Search of Neuronal Morphologies in Light Microscopy. Preprint at bioRxiv, https://doi.org/10.1101/2021.07.23.453511 https://doi.org/10.1101/2021.07.23.453511.

33. Meissner, G.W., Nern, A., Dorman, Z., DePasquale, G.M., Forster, K., Gibney, T., Hausenfluck, J.H., He, Y., Iyer, N.A., Jeter, J., et al. (2023). A searchable image resource of Drosophila GAL4-driver expression patterns with single neuron resolution. eLife *12*, e80660. https://doi.org/10.7554/eLife.80660.

34. Jenett, A., Rubin, G.M., Ngo, T.-T.B., Shepherd, D., Murphy, C., Dionne, H., Pfeiffer, B.D., Cavallaro, A., Hall, D., Jeter, J., et al. (2012). A GAL4-Driver Line Resource for Drosophila Neurobiology. Cell Reports *2*, 991–1001. https://doi.org/10.1016/j.celrep.2012.09.011.

35. Tirian, L., and Dickson, B.J. (2017). The VT GAL4, LexA, and split-GAL4 driver line collections for targeted expression in the Drosophila nervous system. bioRxiv, 198648. https://doi.org/10.1101/198648.

36. Ros, I.G., Omoto, J.J., and Dickinson, M.H. (2024). Descending control and regulation of spontaneous flight turns in Drosophila. Current Biology *34*, 531-540.e5. https://doi.org/10.1016/j.cub.2023.12.047.

37. Eckstein, N., Bates, A.S., Champion, A., Du, M., Yin, Y., Schlegel, P., Lu, A.K.-Y., Rymer, T., Finley-May, S., Paterson, T., et al. (2024). Neurotransmitter classification from electron microscopy images at synaptic sites in *Drosophila melanogaster*. Cell *187*, 2574-2594.e23. https://doi.org/10.1016/j.cell.2024.03.016.

38. Luo, L., Callaway, E.M., and Svoboda, K. (2008). Genetic Dissection of Neural Circuits. Neuron *57*, 634–660. https://doi.org/10.1016/j.neuron.2008.01.002.

39. Hobert, O., and Kratsios, P. (2019). Neuronal identity control by terminal selectors in worms, flies, and chordates. Current Opinion in Neurobiology *56*, 97–105. https://doi.org/10.1016/j.conb.2018.12.006.

40. Baines, R.A., Uhler, J.P., Thompson, A., Sweeney, S.T., and Bate, M. (2001). Altered Electrical Properties in DrosophilaNeurons Developing without Synaptic Transmission. J. Neurosci. *21*, 1523–1531. https://doi.org/10.1523/JNEUROSCI.21-05-01523.2001.

41. Sapkal, N., Mancini, N., Kumar, D.S., Spiller, N., Murakami, K., Vitelli, G., Bargeron, B., Maier, K., Eichler, K., Jefferis, G.S.X.E., et al. (2024). Neural circuit mechanisms underlying context-specific halting in Drosophila. Nature *634*, 191–200. https://doi.org/10.1038/s41586-024-07854-7.

42. Bidaye, S.S., Laturney, M., Chang, A.K., Liu, Y., Bockemühl, T., Büschges, A., and Scott, K. (2020). Two Brain Pathways Initiate Distinct Forward Walking Programs in Drosophila. Neuron *0*. https://doi.org/10.1016/j.neuron.2020.07.032.

43. Choi, H.M.T., Schwarzkopf, M., Fornace, M.E., Acharya, A., Artavanis, G., Stegmaier, J., Cunha, A., and Pierce, N.A. (2018). Third-generation in situ hybridization chain reaction: multiplexed, quantitative, sensitive, versatile, robust. Development *145*, dev165753. https://doi.org/10.1242/dev.165753.

44. Bates, A.S., Phelps, J.S., Kim, M., Yang, H.H., Matsliah, A., Ajabi, Z., Perlman, E., Delgado, K.M., Osman, M.A.M., Salmon, C.K., et al. (2025). Distributed control circuits across a brain-and-cord connectome. Preprint at bioRxiv, https://doi.org/10.1101/2025.07.31.667571 https://doi.org/10.1101/2025.07.31.667571.

45. Spieth, H.T. (1974). Courtship Behavior in *Drosophila*. Annu. Rev. Entomol. *19*, 385–405. https://doi.org/10.1146/annurev.en.19.010174.002125.

46. Dickinson, M.H., and Muijres, F.T. (2016). The aerodynamics and control of free flight manoeuvres in Drosophila. Philosophical Transactions of the Royal Society B: Biological Sciences *371*, 20150388. https://doi.org/10.1098/rstb.2015.0388.

47. Bidaye, S.S., Machacek, C., Wu, Y., and Dickson, B.J. (2014). Neuronal Control of Drosophila Walking Direction. Science *344*, 97–101. https://doi.org/10.1126/science.1249964.

48. Feng, K., Sen, R., Minegishi, R., Dübbert, M., Bockemühl, T., Büschges, A., and Dickson, B.J. (2020). Distributed control of motor circuits for backward walking in Drosophila. Nat Commun *11*, 6166. https://doi.org/10.1038/s41467-020-19936-x.

49. Yang, H.H., Brezovec, B.E., Capdevila, L.S., Vanderbeck, Q.X., Adachi, A., Mann, R.S., and Wilson, R.I. (2024). Fine-grained descending control of steering in walking Drosophila. Cell *0*. https://doi.org/10.1016/j.cell.2024.08.033.

50. Feng, K., Khan, M., Minegishi, R., Müller, A., Poll, M.N.V.D., Swinderen, B. van, and Dickson, B.J. (2024). A central steering circuit in Drosophila. Preprint at bioRxiv, https://doi.org/10.1101/2024.06.27.601106 https://doi.org/10.1101/2024.06.27.601106.

51. Rayshubskiy, A., Holtz, S.L., Bates, A.S., Vanderbeck, Q.X., Capdevila, L.S., Rockwell, V., and Wilson, R.I. (2025). Neural circuit mechanisms for steering control in walking Drosophila. eLife *13*. https://doi.org/10.7554/eLife.102230.2.

52. Braun, J., Hurtak, F., Wang-Chen, S., and Ramdya, P. (2024). Descending networks transform command signals into population motor control. Nature, 1–9. https://doi.org/10.1038/s41586-024-07523-9.

53. Lillvis, J.L., Wang, K., Shiozaki, H.M., Xu, M., Stern, D.L., and Dickson, B.J. (2024). Nested neural circuits generate distinct acoustic signals during Drosophila courtship. Current Biology *34*, 808-824.e6. https://doi.org/10.1016/j.cub.2024.01.015.

54. Shiozaki, H.M., Wang, K., Lillvis, J.L., Xu, M., Dickson, B.J., and Stern, D.L. (2024). Activity of nested neural circuits drives different courtship songs in Drosophila. Nat Neurosci *27*, 1954–1965. https://doi.org/10.1038/s41593-024-01738-9.

55. Simpson, J.H. (2024). Descending control of motor sequences in Drosophila. Current Opinion in Neurobiology *84*, 102822. https://doi.org/10.1016/j.conb.2023.102822.

56. von Philipsborn, A.C., Liu, T., Yu, J.Y., Masser, C., Bidaye, S.S., and Dickson, B.J. (2011). Neuronal Control of Drosophila Courtship Song. Neuron *69*, 509–522. https://doi.org/10.1016/j.neuron.2011.01.011.

57. Hampel, S., Franconville, R., Simpson, J.H., and Seeds, A.M. (2015). A neural command circuit for grooming movement control. eLife *4*, e08758. https://doi.org/10.7554/eLife.08758.

58. Guo, L., Zhang, N., and Simpson, J.H. (2022). Descending neurons coordinate anterior grooming behavior in Drosophila. Current Biology *0*. https://doi.org/10.1016/j.cub.2021.12.055.

59. von Reyn, C.R., Breads, P., Peek, M.Y., Zheng, G.Z., Williamson, W.R., Yee, A.L., Leonardo, A., and Card, G.M. (2014). A spike-timing mechanism for action selection. Nature Neuroscience *17*, 962–970. https://doi.org/10.1038/nn.3741.

60. Wang, F., Wang, K., Forknall, N., Parekh, R., and Dickson, B.J. (2020). Circuit and Behavioral Mechanisms of Sexual Rejection by Drosophila Females. Current Biology *30*, 3749-3760.e3. https://doi.org/10.1016/j.cub.2020.07.083.

61. Wang, F., Wang, K., Forknall, N., Patrick, C., Yang, T., Parekh, R., Bock, D., and Dickson, B.J. (2020). Neural circuitry linking mating and egg laying in Drosophila females. Nature *579*, 101–105. https://doi.org/10.1038/s41586-020-2055-9.

62. Wang, K., Wang, F., Forknall, N., Yang, T., Patrick, C., Parekh, R., and Dickson, B.J. (2021). Neural circuit mechanisms of sexual receptivity in Drosophila females. Nature *589*, 577–581. https://doi.org/10.1038/s41586-020-2972-7.

63. McKellar, C.E., Lillvis, J.L., Bath, D.E., Fitzgerald, J.E., Cannon, J.G., Simpson, J.H., and Dickson, B.J. (2019). Threshold-Based Ordering of Sequential Actions during Drosophila Courtship. Current Biology *29*, 426-434.e6. https://doi.org/10.1016/j.cub.2018.12.019.

64. Wiersma, C.A.G., and Ikeda, K. (1964). Interneurons commanding swimmeret movements in the crayfish, *Procambarus clarki* (girard). Comparative Biochemistry and Physiology *12*, 509–525. https://doi.org/10.1016/0010-406X(64)90153-7.

65. Hedwig, B. (2006). Pulses, patterns and paths: neurobiology of acoustic behaviour in crickets. J Comp Physiol A *192*, 677–689. https://doi.org/10.1007/s00359-006-0115-8.

66. Bouvier, J., Caggiano, V., Leiras, R., Caldeira, V., Bellardita, C., Balueva, K., Fuchs, A., and Kiehn, O. (2015). Descending Command Neurons in the Brainstem that Halt Locomotion. Cell *163*, 1191–1203. https://doi.org/10.1016/j.cell.2015.10.074.

67. Cande, J., Namiki, S., Qiu, J., Korff, W., Card, G.M., Shaevitz, J.W., Stern, D.L., and Berman, G.J. (2018). Optogenetic dissection of descending behavioral control in Drosophila. eLife *7*, e34275. https://doi.org/10.7554/eLife.34275.

68. Aymanns, F., Chen, C.-L., and Ramdya, P. (2022). Descending neuron population dynamics during odor-evoked and spontaneous limb-dependent behaviors. eLife *11*, e81527. https://doi.org/10.7554/eLife.81527.

69. Namiki, S., Ros, I.G., Morrow, C., Rowell, W.J., Card, G.M., Korff, W., and Dickinson, M.H. (2022). A population of descending neurons that regulates the flight motor of Drosophila. Current Biology *0*. https://doi.org/10.1016/j.cub.2022.01.008.

70. Dombrovski, M., Peek, M.Y., Park, J.-Y., Vaccari, A., Sumathipala, M., Morrow, C., Breads, P., Zhao, A., Kurmangaliyev, Y.Z., Sanfilippo, P., et al. (2023). Synaptic gradients transform object location to action. Nature *613*, 534–542. https://doi.org/10.1038/s41586-022-05562-8.

71. Coen, P., Clemens, J., Weinstein, A.J., Pacheco, D.A., Deng, Y., and Murthy, M. (2014). Dynamic sensory cues shape song structure in Drosophila. Nature *507*, 233–237. https://doi.org/10.1038/nature13131.

72. Coen, P., Xie, M., Clemens, J., and Murthy, M. (2016). Sensorimotor Transformations Underlying Variability in Song Intensity during Drosophila Courtship. Neuron *89*, 629–644. https://doi.org/10.1016/j.neuron.2015.12.035.

73. Clemens, J., Coen, P., Roemschied, F.A., Pereira, T.D., Mazumder, D., Aldarondo, D.E., Pacheco, D.A., and Murthy, M. (2018). Discovery of a New Song Mode in *Drosophila* Reveals Hidden Structure in the Sensory and Neural Drivers of Behavior. Current Biology *28*, 2400-2412.e6. https://doi.org/10.1016/j.cub.2018.06.011.

74. Cowley, B.R., Calhoun, A.J., Rangarajan, N., Ireland, E., Turner, M.H., Pillow, J.W., and Murthy, M. (2024). Mapping model units to visual neurons reveals population code for social behaviour. Nature, 1–9. https://doi.org/10.1038/s41586-024-07451-8.

75. Cox, J., and Witten, I.B. (2019). Striatal circuits for reward learning and decision-making. Nat Rev Neurosci *20*, 482–494. https://doi.org/10.1038/s41583-019-0189-2.

76. Kohatsu, S., Koganezawa, M., and Yamamoto, D. (2011). Female Contact Activates Male-Specific Interneurons that Trigger Stereotypic Courtship Behavior in Drosophila. Neuron *69*, 498–508. https://doi.org/10.1016/j.neuron.2010.12.017.

77. Pan, Y., Meissner, G.W., and Baker, B.S. (2012). Joint control of Drosophila male courtship behavior by motion cues and activation of male-specific P1 neurons. Proceedings of the National Academy of Sciences *109*, 10065–10070. https://doi.org/10.1073/pnas.1207107109.

78. Hindmarsh Sten, T., Li, R., Otopalik, A., and Ruta, V. (2021). Sexual arousal gates visual processing during Drosophila courtship. Nature *595*, 549–553. https://doi.org/10.1038/s41586-021-03714-w.

79. Card, G.M. (2012). Escape behaviors in insects. Current Opinion in Neurobiology *22*, 180–186. https://doi.org/10.1016/j.conb.2011.12.009.

80. Meissner, G.W., Vannan, A., Jeter, J., Close, K., DePasquale, G.M., Dorman, Z., Forster, K., Beringer, J.A., Gibney, T., Hausenfluck, J.H., et al. (2025). A split-GAL4 driver line resource for Drosophila neuron types. eLife *13*, RP98405. https://doi.org/10.7554/eLife.98405.

81. Kvon, E.Z., Kazmar, T., Stampfel, G., Yáñez-Cuna, J.O., Pagani, M., Schernhuber, K., Dickson, B.J., and Stark, A. (2014). Genome-scale functional characterization of

Drosophila developmental enhancers in vivo. Nature *512*, 91–95. https://doi.org/10.1038/nature13395.

82. Pfeiffer, B.D., Ngo, T.-T.B., Hibbard, K.L., Murphy, C., Jenett, A., Truman, J.W., and Rubin, G.M. (2010). Refinement of Tools for Targeted Gene Expression in Drosophila. Genetics *186*, 735–755. https://doi.org/10.1534/genetics.110.119917.

83. Pfeiffer, B.D., Jenett, A., Hammonds, A.S., Ngo, T.-T.B., Misra, S., Murphy, C., Scully, A., Carlson, J.W., Wan, K.H., Laverty, T.R., et al. (2008). Tools for neuroanatomy and neurogenetics in Drosophila. PNAS *105*, 9715–9720. https://doi.org/10.1073/pnas.0803697105.

84. Bogovic, J.A., Otsuna, H., Heinrich, L., Ito, M., Jeter, J., Meissner, G., Nern, A., Colonell, J., Malkesman, O., Ito, K., et al. (2020). An unbiased template of the Drosophila brain and ventral nerve cord. PLOS ONE *15*, e0236495. https://doi.org/10.1371/journal.pone.0236495.

85. Masse, N.Y., Cachero, S., Ostrovsky, A.D., and Jefferis, G.S.X.E. (2012). A Mutual Information Approach to Automate Identification of Neuronal Clusters in Drosophila Brain Images. Front. Neuroinform. *6*. https://doi.org/10.3389/fninf.2012.00021.

86. Inagaki, H.K., Jung, Y., Hoopfer, E.D., Wong, A.M., Mishra, N., Lin, J.Y., Tsien, R.Y., and Anderson, D.J. (2014). Optogenetic control of Drosophila using a red-shifted channelrhodopsin reveals experience-dependent influences on courtship. Nature Methods *11*, 325–332. https://doi.org/10.1038/nmeth.2765.

87. Jung, Y., Kennedy, A., Chiu, H., Mohammad, F., Claridge-Chang, A., and Anderson, D.J. (2020). Neurons that Function within an Integrator to Promote a Persistent Behavioral State in Drosophila. Neuron *105*, 322-333.e5. https://doi.org/10.1016/j.neuron.2019.10.028.

88. Weir, P.T., Henze, M.J., Bleul, C., Baumann-Klausener, F., Labhart, T., and Dickinson, M.H. (2016). Anatomical Reconstruction and Functional Imaging Reveal an Ordered Array of Skylight Polarization Detectors in Drosophila. J. Neurosci. *36*, 5397–5404. https://doi.org/10.1523/JNEUROSCI.0310-16.2016.

89. Clements, J., Dolafi, T., Umayam, L., Neubarth, N.L., Berg, S., Scheffer, L.K., and Plaza, S.M. (2020). neuPrint: Analysis Tools for EM Connectomics. Preprint at bioRxiv, https://doi.org/10.1101/2020.01.16.909465 https://doi.org/10.1101/2020.01.16.909465.

90. Bates, A.S., Manton, J.D., Jagannathan, S.R., Costa, M., Schlegel, P., Rohlfing, T., and Jefferis, G.S. (2020). The natverse, a versatile toolbox for combining and analysing neuroanatomical data. eLife *9*, e53350. https://doi.org/10.7554/eLife.53350.

91. Gu, Z. (2022). Complex heatmap visualization. iMeta *1*, e43. https://doi.org/10.1002/imt2.43.

92. Eyjolfsdottir, E., Branson, S., Burgos-Artizzu, X.P., Hoopfer, E.D., Schor, J., Anderson, D.J., and Perona, P. (2014). Detecting Social Actions of Fruit Flies. In Computer Vision – ECCV 2014, D. Fleet, T. Pajdla, B. Schiele, and T. Tuytelaars, eds. (Springer International Publishing), pp. 772–787. https://doi.org/10.1007/978-3-319-10605-2_50.

Chapter 3

FUTURE DIRECTIONS

Chapter III: Future directions

This work identifies a hierarchical neural circuit that coordinates actions across different appendages during a complex social display, in which neurons are organized into appendage-specific functional modules and control actions in a combinatorial manner. These findings provide a framework for understanding how actions are organized and selected within an innate social behavior. This work raises new questions — including what the remaining AIP downstream targets do, how combinatorial coding is implemented circuit-wide, and how sensory cues guide action selection — and comes with limitations that future efforts could address.

One such limitation concerns the necessity of AIP downstream targets, which has thus far been established primarily through epistasis experiments, whereas, except for DNpe050, silencing these neurons during natural interactions fails to produce observable phenotypes. This discrepancy could reflect functional redundancy among other downstream neurons, or even neurons outside the AIP circuit. It remains difficult to know how these neurons are activated during natural interactions, as imaging neural activity during the occurrence of natural wing threat display is currently infeasible. This limitation likely stems from constraints inherent to both *Drosophila* imaging preparations and wing threat display itself: head-fixed, open-cuticle preparations support only a limited repertoire of behaviors, and wing threat itself is a low-frequency behavior, occurring in roughly 1-5% of total

agonistic interaction time — far less frequent than walking, flying, or even courtship. Addressing these limitations will therefore require both a more comprehensive characterization of AIP downstream targets and a clearer understanding of how sensory information feeds into this circuit.

With these findings and limitations in mind, I will discuss several future directions that could address these open questions while also generating new insights.

3.1 The role of uncharacterized AIP downstream targets

In this work, we identified genetic driver lines for, and functionally characterized, four AIP downstream targets. Several questions remain unresolved. Silencing either AVLP491 or AVLP710m reduced AIP-induced turning and charging but produced no detectable phenotype during naturally occurring wing threat, suggesting that the circuit contains redundant pathways capable of compensating for the loss of either neuron. In addition, activation of AVLP491 alone did not fully recapitulate the velocity generated by AIP-induced turning and charging, indicating that additional AIP downstream targets likely contribute to modulating locomotor velocity.

Among the still-uncharacterized targets, AVLP016 is particularly intriguing. It forms reciprocal inhibitory connection with AVLP710m and provides input to at least ten distinct DN types. Its top downstream target, PVLP004, is heavily interconnected with LC9, a visual projection neuron[1]. This arrangement raises the possibility that AVLP016 participates in the visual regulation of wing threat locomotion. CL335 and ICL008m are also of interest, since together they provide feedforward inhibition onto DNpe050 and DNp60, the two descending

neurons that drive wing actions, suggesting a role in shaping the selection and temporal dynamics of wing actions.

Efforts to generate specific genetic drivers for these neurons have so far been unsuccessful. As the community continues to accumulate new drivers[2,3], further attempts may prove fruitful and would open the door to functional characterization of these neurons.

3.2 Combinatorial control of individual threat actions

A key finding of this work is that individual threat actions are not driven by any single cell type but instead arise from the combinatorial activity of functional modules. Wing actions depend on the synergistic interaction of two descending neuron types, while the "stuttering"-like locomotion emerges from two functionally antagonistic interneurons. Although this phenotypic logic has now been established, the circuit mechanism underlying these computations remains an open and interesting question.

The connectome dataset offers initial clues. Downstream of the two wing descending neurons, DNpe050 and DNp60, sit several interconnected first-order targets – notably, several of these targets have previously been identified as courtship singing neurons[4,5]. I hypothesize that these neurons have been classified as courtship singing neurons simply because their role has so far only been examined in the context of courtship song. It is therefore plausible that a single, large wing network exists, in which the specific wing movement produced depends on which descending input drives the network at a given moment.

Downstream of the leg interneurons AVLP491 and AVLP710m, lies a large, interconnected network of leg-related descending neurons. Several of these have been

reported to participate in other locomotor contexts[6,7]. For example, DNg100 and DNge050 also receive input from BPN, a central-brain interneuron type that promotes straight walking, and DNg75 and DNg97 receive input from DNp09, a DN type that promotes courtship chasing. It is therefore plausible that walking-related DNs are reused across different locomotor contexts, with different combinations recruited by different upstream neurons.

Notably, epistatic silencing of the excitatory neuron AVLP491 and the inhibitory neuron AVLP710m both reduced turning and charging — a counterintuitive result given their opposing valence. This argues against a simple mechanism in which the "stuttering"-like locomotion arises from repetitively toggling specific walking neurons on and off. Combined with the dense interconnectivity among the downstream DNs of AVLP491 and AVLP710m, the result points instead to a network-level computation.

Addressing these questions will require a combined approach: (i) a closer kinematic analysis of appendage movement during wing threat; (ii) identification of genetic drivers for the wing VNC neurons and leg DNs, so that their functions can be tested directly in this behavioral assay; and (iii) computational modeling of the circuit[8,9] to expose the computational principles at work.

The question of combinatorial coding is likely to hold broad interest for the neuroscience community, as recent work has begun to reveal control of innate behavior by population-coding across interconnected neural populations[10–12]. However, the mechanistic basis of these networks remains elusive.

3.3 The role of sensory cues in action combination and selection

One characteristic feature of wing threat behavior is that its actions display both flexible and stereotyped combinations. The wing pump is always accompanied by turning and charging, whereas wing elevation can occur with or without turning and charging.

Several mechanisms might explain this pattern. One possibility relates to the scalability of AIP: AIP neurons were found to induce wing threat actions at different activation thresholds, with turning and charging having the lowest threshold, wing elevation an intermediate threshold, and the pump the highest. This suggests that AIP may function as a "dial" node that scales behavioral output with activity level. Such scaling would explain why turning and charging always accompanies the wing pump — once AIP activity reaches the threshold for the pump, it has necessarily already exceeded the threshold for turning and charging. However, this model does not explain how wing elevation can be decoupled from turning and charging, and how AIP activity level is determined.

Previous work has shown that a combination of chemosensory and visual cues is both necessary and sufficient to induce wing threat behavior[13]. This was demonstrated in an elegant experiment using a dead male target paired with an actuated, fly-size magnet: flies displayed wing threat only when the dead male target (providing the chemosensory cue) was present and the magnet was in motion (providing the visual cue). Importantly, the wing threat was directed specifically at the magnet.

The integration of chemosensory cues could occur at different levels in the circuit. (i) Integration occurs upstream of, or at, the AIP neurons, and AIP then functions as a scalable node that dictates the expression of wing threat actions through distinct firing patterns. (ii) AIP neurons represent the chemosensory arm of the circuit — supported by the finding that AIP activation can substitute for the velocity cue and eliminate the requirement for it[13] —

while visual cues trigger specific actions by impinging onto AIP's downstream targets. One potential impinging point is AVLP491, which receives indirect input from visual projection neurons via the interneuron PVLP130. Another is AVLP016, which receives indirect inhibitory input from LC9 via PVLP004, and forms reciprocal inhibitory connections with AVLP710m. Visual projection neurons LC9[1] thus could disinhibit AVLP710m through this LC9-PVLP004-AVLP016-AVLP710m pathway.

To test these models, I propose three approaches. First, use a computational approach such as generalized linear models[14–16] to identify features of the tester-target interaction that predict the occurrence of wing threat actions. This would provide clues of which types of visual cues trigger specific actions, and which actions are not dependent on visual cue. Second, use functional imaging to probe the activity of AIP and its downstream targets in response to visual motion cues, to identify neurons that are sensitive to these cues. Third, perform an unbiased screening or a connectome-assisted candidate-based approach to identify the visual projection neurons[1,17–19] whose perturbation alters the behavioral dynamics of the wing threat actions.

References

1. Wu, M., Nern, A., Williamson, W.R., Morimoto, M.M., Reiser, M.B., Card, G.M., and Rubin, G.M. (2016). Visual projection neurons in the Drosophila lobula link feature detection to distinct behavioral programs. eLife *5*, e21022. https://doi.org/10.7554/eLife.21022.

2. Meissner, G.W., Nern, A., Dorman, Z., DePasquale, G.M., Forster, K., Gibney, T., Hausenfluck, J.H., He, Y., Iyer, N.A., Jeter, J., et al. (2023). A searchable image resource of Drosophila GAL4-driver expression patterns with single neuron resolution. eLife *12*, e80660. https://doi.org/10.7554/eLife.80660.

3. Meissner, G.W., Vannan, A., Jeter, J., Close, K., DePasquale, G.M., Dorman, Z., Forster, K., Beringer, J.A., Gibney, T., Hausenfluck, J.H., et al. (2025). A split-GAL4 driver line resource for Drosophila neuron types. eLife *13*, RP98405. https://doi.org/10.7554/eLife.98405.

4. Lillvis, J.L., Wang, K., Shiozaki, H.M., Xu, M., Stern, D.L., and Dickson, B.J. (2024). Nested neural circuits generate distinct acoustic signals during Drosophila courtship. Current Biology *34*, 808-824.e6. https://doi.org/10.1016/j.cub.2024.01.015.

5. Shiozaki, H.M., Wang, K., Lillvis, J.L., Xu, M., Dickson, B.J., and Stern, D.L. (2024). Activity of nested neural circuits drives different courtship songs in Drosophila. Nat Neurosci *27*, 1954–1965. https://doi.org/10.1038/s41593-024-01738-9.

6. Sapkal, N., Mancini, N., Kumar, D.S., Spiller, N., Murakami, K., Vitelli, G., Bargeron, B., Maier, K., Eichler, K., Jefferis, G.S.X.E., et al. (2024). Neural circuit mechanisms underlying context-specific halting in Drosophila. Nature *634*, 191–200. https://doi.org/10.1038/s41586-024-07854-7.

7. Sapkal, N., Kumar, D.S., Sunke, S., Mancini, N., Pitchford, J., Murakami, K., and Bidaye, S.S. (2026). Central versus peripheral neural control of a coordinated walking pattern in Drosophila. Preprint at bioRxiv, https://doi.org/10.64898/2026.04.29.721658 https://doi.org/10.64898/2026.04.29.721658.

8. Shiu, P.K., Sterne, G.R., Spiller, N., Franconville, R., Sandoval, A., Zhou, J., Simha, N., Kang, C.H., Yu, S., Kim, J.S., et al. (2024). A Drosophila computational brain model reveals sensorimotor processing. Nature *634*, 210–219. https://doi.org/10.1038/s41586-024-07763-9.

9. Pugliese, S.M., Chou, G.M., Abe, E.T.T., Turcu, D., Lancaster, J.K., Tuthill, J.C., and Brunton, B.W. (2026). Connectome simulations identify a central pattern generator circuit

for fly walking. Preprint at bioRxiv, https://doi.org/10.1101/2025.09.12.675944 https://doi.org/10.1101/2025.09.12.675944.

10. Aymanns, F., Chen, C.-L., and Ramdya, P. (2022). Descending neuron population dynamics during odor-evoked and spontaneous limb-dependent behaviors. eLife *11*, e81527. https://doi.org/10.7554/eLife.81527.

11. Braun, J., Hurtak, F., Wang-Chen, S., and Ramdya, P. (2024). Descending networks transform command signals into population motor control. Nature, 1–9. https://doi.org/10.1038/s41586-024-07523-9.

12. Nair, A., Karigo, T., Yang, B., Ganguli, S., Schnitzer, M.J., Linderman, S.W., Anderson, D.J., and Kennedy, A. (2023). An approximate line attractor in the hypothalamus encodes an aggressive state. Cell *186*, 178-193.e15. https://doi.org/10.1016/j.cell.2022.11.027.

13. Duistermars, B.J., Pfeiffer, B.D., Hoopfer, E.D., and Anderson, D.J. (2018). A Brain Module for Scalable Control of Complex, Multi-motor Threat Displays. Neuron *100*, 1474-1490.e4. https://doi.org/10.1016/j.neuron.2018.10.027.

14. Coen, P., Clemens, J., Weinstein, A.J., Pacheco, D.A., Deng, Y., and Murthy, M. (2014). Dynamic sensory cues shape song structure in Drosophila. Nature *507*, 233–237. https://doi.org/10.1038/nature13131.

15. Coen, P., Xie, M., Clemens, J., and Murthy, M. (2016). Sensorimotor Transformations Underlying Variability in Song Intensity during Drosophila Courtship. Neuron *89*, 629–644. https://doi.org/10.1016/j.neuron.2015.12.035.

16.Clemens, J., Coen, P., Roemschied, F.A., Pereira, T.D., Mazumder, D., Aldarondo, D.E., Pacheco, D.A., and Murthy, M. (2018). Discovery of a New Song Mode in *Drosophila* Reveals Hidden Structure in the Sensory and Neural Drivers of Behavior. Current Biology *28*, 2400-2412.e6. https://doi.org/10.1016/j.cub.2018.06.011.

17. Keleş, M.F., and Frye, M.A. (2017). Object-Detecting Neurons in Drosophila. Current Biology *27*, 680–687. https://doi.org/10.1016/j.cub.2017.01.012.

18. Klapoetke, N.C., Nern, A., Rogers, E.M., Rubin, G.M., Reiser, M.B., and Card, G.M. (2022). A functionally ordered visual feature map in the Drosophila brain. Neuron *0*. https://doi.org/10.1016/j.neuron.2022.02.013.

19. Cowley, B.R., Calhoun, A.J., Rangarajan, N., Ireland, E., Turner, M.H., Pillow, J.W., and Murthy, M. (2024). Mapping model units to visual neurons reveals population code for social behaviour. Nature, 1–9. https://doi.org/10.1038/s41586-024-07451-8.